

Can we use topography to differentiate between area and discharge-driven incision rules, and if not how bad are our estimates of channel steepness?

Marina Ruiz Sánchez-Oro¹, Simon Marius Mudd², and Boris Gailleton³

¹The University of Edinburgh

²University of Edinburgh

³CNRS - Geosciences Rennes, Université de Rennes

January 13, 2024

Abstract

The rate of channel incision in bedrock rivers is often described using a power law relationship that scales erosion with drainage area. However, erosion in landscapes that experience strong rainfall gradients may be better described by discharge instead of drainage area. In this study we test if these two end member scenarios result in identifiable topographic signatures in both idealized numerical simulations and in natural landscapes. We find that in simulations using homogeneous lithology, we can differentiate a posteriori between drainage area and discharge-driven incision scenarios by quantifying the relative disorder of channel profiles, as measured by how well tributary profiles mimic both the main stem channel and each other. The more heterogeneous the landscape becomes, the harder it proves to identify the disorder signatures of the end member incision rules. We then apply these indicators to natural landscapes, and find, among 8 test areas, no clear topographic signal that allows us to conclude a discharge or area-driven incision rule is more appropriate. We then quantify the distortion in the channel steepness index induced by changing the incision rule. Distortion in the channel steepness index can also be driven by changes to the assumed reference concavity index, and we find that distortions in the normalized channel steepness index, frequently used as a proxy for erosion rates, is more sensitive to changes in the concavity index than to changes in the assumed incision rule. This makes it a priority to optimize the concavity index even under an unknown incision mechanism.

1 **Can we use topography to differentiate between area**
2 **and discharge-driven incision rules, and if not how bad**
3 **are our estimates of channel steepness?**

4 **Marina Ruiz Sánchez-Oro¹, Simon M. Mudd¹, and Boris Gailleton²**

5 ¹School of GeoSciences, University of Edinburgh, Edinburgh, UK
6 ²CNRS - Geosciences Rennes, Université de Rennes, France

7 **Key Points:**

- 8 • Discharge-driven incision can be identified *a posteriori* in simulated landscapes
9 but not in natural topography.
10 • The choice of concavity index (θ) can distort the channel steepness index more
11 than the choice of incision type.
12 • Topographic metrics should be accompanied by field explorations to fully describe
13 the erosional history of a landscape.

Corresponding author: Marina Ruiz Sánchez-Oro, marina.ruiz.so@ed.ac.uk

Abstract

The rate of channel incision in bedrock rivers is often described using a power law relationship that scales erosion with drainage area. However, erosion in landscapes that experience strong rainfall gradients may be better described by discharge instead of drainage area. In this study we test if these two end member scenarios result in identifiable topographic signatures in both idealized numerical simulations and in natural landscapes. We find that in simulations using homogeneous lithology, we can differentiate *a posteriori* between drainage area and discharge-driven incision scenarios by quantifying the relative disorder of channel profiles, as measured by how well tributary profiles mimic both the main stem channel and each other. The more heterogeneous the landscape becomes, the harder it proves to identify the disorder signatures of the end member incision rules. We then apply these indicators to natural landscapes, and find, among 8 test areas, no clear topographic signal that allows us to conclude a discharge or area-driven incision rule is more appropriate. We then quantify the distortion in the channel steepness index induced by changing the incision rule. Distortion in the channel steepness index can also be driven by changes to the assumed reference concavity index, and we find that distortions in the normalized channel steepness index, frequently used as a proxy for erosion rates, is more sensitive to changes in the concavity index than to changes in the assumed incision rule. This makes it a priority to optimize the concavity index even under an unknown incision mechanism.

Plain Language Summary

Rivers erode into mountains as a result of both the sediment transported as the water flows downstream and the amount of water that the river transports. The amount of rainfall that each part of the river receives affects how much the channel cuts into the rock. In this study, we assess whether it is possible to differentiate between rivers where sediment is responsible for most of the erosion work and rivers where rainfall has a larger erosive power. Through computer simulations, we measure the river fingerprint in the landscape through calculations involving how tributary and main channel slopes compare, and how quickly a channel steepens as it travels away from the headwaters. We extract these fingerprints and search for them in the more complex natural landscapes, measuring how much they change under heavy rainfall. We find that these fingerprints are camouflaged by factors such as changes in rock types, making it a challenge to identify them without field observations.

1 Introduction

Physical intuition suggests that, if all other factors are equal, a steeper river will erode faster than a gentler one. This basic relationship has been proposed by geomorphologists for over a century (Gilbert, 1877). It is unusual, however, to find two channels identical in their properties with the exception of their gradient. Headwaters are, for example, frequently steeper than downstream rivers they feed. In the early 1960s geomorphologists realized that gradient could be related to drainage area in a power law with a negative exponent (Hack, 1960; Morisawa, 1962). This basic relationship was formalized by Flint (1974):

$$S = k_s A^{-\theta} \quad (1)$$

where the concavity index, θ , describes how fast the gradient of the river changes downstream and the constant k_s , channel steepness index, describes the dependence of gradient normalized for drainage area. We can further fix the value of θ to a fixed reference value (θ_{ref}), after which we denote the channel steepness index with k_{sn} . This normal-

61 ization allows us to compare the relative steepness of rivers with different drainage ar-
62 eas (Flint, 1974).

63 Numerous studies have found that this relative steepness (k_{sn}) is positively cor-
64 related with measured erosion rates in upland landscapes (Wobus et al., 2006; DiBiase
65 et al., 2010; Kirby & Whipple, 2012; Harel et al., 2016; Adams et al., 2020; Gailleton et
66 al., 2021; Harries et al., 2021; Peifer et al., 2021). In regions without data on erosion rates
67 we might therefore use k_{sn} as a proxy for erosion rate (Kirby & Whipple, 2012). This
68 is not quite as straightforward as it sounds, however. If we return to physical intuition,
69 consider two channels with all properties equal apart from the amount of water they con-
70 vey (quantified as, e.g., their mean annual discharge or some other statistical represen-
71 tation of runoff). Many authors have proposed relationships between channel incision
72 and the physical properties of bedrock rivers, and these proposals include the influence
73 of sediment supply (dependent on A), sediment transport capacity (dependent on hy-
74 draulic conditions and gradient), shear stress (dependent on flow depth, and thus hy-
75 draulic conditions), stream power (again, hydraulic conditions), and thresholding behav-
76 ior of all the above factors (Howard, 1987; Wobus et al., 2010; Finnegan et al., 2007; John-
77 son & Whipple, 2010; Baynes et al., 2020). This means that computation of k_{sn} based
78 on drainage area rather than hydraulic conditions (e.g., discharge) may not represent the
79 incision process.

80 One reason erosion rate proxies have tended towards using an area-based k_{sn} is
81 because drainage area is trivial to extract from topographic data. Discharge (Q) records
82 are not always easy to obtain, and gauging stations are at points rather than distributed
83 throughout the landscape. However, various global datasets, for example TRMM (Kummerow
84 et al., 2000) and GPM (Skofronick-Jackson et al., 2017) have made it relatively simple
85 to estimate and aggregate precipitation over a basin, over a variety of timescales, which
86 means it is now quite simple to obtain an estimate of discharge in a basin given a lin-
87 ear relationship between aggregate precipitation and discharge.

88 These precipitation datasets enable us to calculate the channel steepness index, k_{sn} ,
89 based on effective discharge rather than drainage area. And indeed, a number of recent
90 authors have taken this approach (e.g., Babault et al., 2018; Adams et al., 2020; Leonard
91 & Whipple, 2021; Harries et al., 2021; Leonard et al., 2023). If precipitation rates are
92 uniform across a catchment, the drainage area-gradient relationship will have the same
93 spatial pattern as the drainage area-discharge relationship. But rainfall can be influenced
94 by mountains (Roe et al., 2002; Anders et al., 2006; Bookhagen & Burbank, 2006; Bookha-
95 gen & Strecker, 2008; Craddock et al., 2007; Gasparini & Whipple, 2014), meaning that
96 the patterns of k_{sn} might be different if one uses A or a more direct estimate of Q that
97 incorporates spatially varied precipitation.

98 One might assume that the latter is always “better” than the former. But there
99 are some reasons why erosion rates, and gradients, might be more sensitive to drainage
100 area than discharge. The main reason for this is that water does not erode the bed of
101 rivers, sediment does. And the amount of sediment fluxing through any part of the chan-
102 nel in a steadily uplifting mountain range should depend on drainage area and not dis-
103 charge. In addition, rivers transporting gravel will alter their geometry, for example their
104 width (Dunne & Jerolmack, 2020; Phillips & Jerolmack, 2016; Pfeiffer et al., 2017), to
105 accommodate sediment supply and this could cause a damping effect on the relationship
106 between discharge and erosion rates. So although it intuitively might make sense to al-
107 ways use discharge-based calculations of k_{sn} , we are not, at present, certain if this is bet-
108 ter than a calculation using A .

109 Any proposed erosion rule, be it area or discharge driven, can be transformed into
110 a prediction of topography. For example, the most basic erosion law incorporating gra-
111 dient and area of takes the form (Howard & Kerby, 1983):

112

$$E = KA^m S^n \quad (2)$$

113

114

115

116

117

118

119

120

121

122

123

where K is an erodibility and m and n are empirical coefficients. If one rearranges equation 2 to isolate S and compares the result with equation 1, one can see that, if equation 2 is correct, $k_{sn} = (E/K)^{1/n}$ and $\theta = m/n$. Thus equation 2 predicts a power law relationship between gradient and drainage area where erosion rates are invariant in time and space. It can also be shown that this power law relationship holds in segments of constant erosion that move upstream in transiently eroding landscapes (L. Royden & Perron, 2013). Various threshold models have been proposed as more complex versions of equation 2, but much of their relevant behavior can be captured by altering the n exponent (Gasparini & Brandon, 2011). While this approach is not without controversy (Lague, 2014), it is at least not clearly falsified by relationships between topographic data and measured erosion rates.

124

125

126

127

128

129

130

131

132

Such topographic predictions suggest a basic test: if there are strong gradients in precipitation, we expect the topographic outcomes of incision rules that are driven by either A or Q to differ. In this contribution we first explore the question: if we know erosion rates are driven by either A or Q , could we tell the difference just based on topography? We use numerical experiments to answer this question. We explore the extent to which heterogeneity in uplift rates and erodibilities can cloud this signal. Finally, we explore real landscapes to see if we can find locations, based on our proposed metrics, where it is clear that an area-based or discharge-based calculation of k_{sn} is more appropriate.

133

2 Methods

134

135

136

137

138

139

140

Our study includes three components. First, we perform a series of numerical experiments using a simple landscape evolution model with different imposed incision rules, and in addition alter other model parameters such as rainfall gradient. The aim of these simulations is to produce landscapes under idealized and controlled conditions against which metrics for determining the most likely incision rule may be tested. We then develop metrics that allow us to test if a particular incision rule better describes observed topography. Finally, we deploy these metrics on real landscapes.

141

2.1 Numerical simulations

142

143

144

145

146

We simulate landscapes where bedrock channels incise through an uplifting landscape. We thus must select an incision rule for our simulations. For the purposes of simplicity, we use the basic form of the stream power incision model (equation 2), which can emulate different incision mechanisms by altering the n exponent (Gasparini & Brandon, 2011).

147

148

149

150

Equation 2 is not influenced by discharge. For discharge-based incision, we follow other authors (e.g. Adams et al., 2020) and replace drainage area with a proxy for discharge, which we compute with the substitution $Q = A \times \text{Rainfall}$ where the rainfall is converted into runoff and accumulated downstream, yielding:

151

$$E = K_{lp} Q^m S^n. \quad (3)$$

152

153

In reality, the discharge will be modulated by other features such as evapotranspiration and infiltration rates, but these factors are subsumed into the parameter K_{lp} .

154

The model then simulates topographic evolution with a simple mass balance:

$$\frac{\partial z}{\partial t} = U - E \quad (4)$$

where U is the uplift rate and the erosion rate, E , is solved by either equation 2 or 3. Simulations are performed using the FastScape framework (Bovy & Lange, 2023). FastScape uses the methods developed by Braun and Willett (2013) that takes advantage of graph theory to efficiently solve equations 2 (or 3) with an implicit finite different scheme.

In order to implement equation 3, we must assign a precipitation pattern. In our experiments, we explore different precipitation gradients. Models do exist where precipitation depends on elevation and prevailing wind direction, for example the model of Smith and Barstad (2004) which was used by Han et al. (2015). Such models involve multiple parameters, and to obtain the desired precipitation gradient one must engage in fine tuning each of these parameters. For consistency across experiments, we decided instead to increase precipitation linearly as a function of distance from the mountain front, with precipitation gradients comparable to real orographic rainfall gradients. Leonard and Whipple (2021) found that a linear rainfall gradient can be a good approximation to studying orographic precipitation patterns in natural landscapes.

We impose rainfall gradients that will mimic natural orographic patterns found in natural landscapes. In the driest scenario, we impose a rainfall gradient across the simulated mountain range of 1 m/yr (that is, the precipitation is 1 m/yr greater at the peak rainfall location than at the minimum rainfall location). In our wettest scenario, the increase in rainfall reaches 10 m/yr across the simulation domain, corresponding to the highest rainfall achieved in the Bhutan Himalayas (Grujic et al., 2018; Anders et al., 2006).

2.1.1 Homogeneous Lithologies

We run experiments on a regular grid ($\Delta x = 30m$) grid over a mountain range that is 15 km by 30 km (see Table 1 in S1 for full parameter details). This size was selected as a compromise between the number of basins that could be formed during a simulation and computational expense. We begin each landscape with a random surface generated using the diamond square algorithm (Fournier et al., 1982; Perron & Royden, 2013) with noise ranging from 0 to 1 m. We choose this initial condition as it produces a greater variety of channel network structures than the more widely used white noise. Each simulation is run to steady state, where the change in erosion is balanced by uplift.

For a given uplift and precipitation gradient, we calculate the landscape resulting from each of the two incision laws as described by equations 2 and 3. Initial experiments use uniform erodibility to simulate homogeneous lithology. The boundary conditions include a fixed elevation on the east and west edges (which allow flux to exit the model) and periodic boundaries at the north and south of the model domain. The resulting mountain range emerges in the North-South direction.

Within the discharge-driven model, we set up one simulation for each rainfall scenario, starting from a gradient of 0 m/yr to 10 m/yr (increasing from East to West in the simulation domain), for a total of 11 simulations. The precipitation runs explore how different rainfall amounts affect river incision mechanisms and whether larger gradients generate a stronger signal in the landscape.

Both the erodibility coefficient and the uplift rate are kept constant across all simulations at 3×10^{-8} and uplift rate is 1×10^{-5} respectively, yielding landscape reliefs within the ranges of those found on Earth. Similarly, n is chosen as 1 and m as 0.45 to keep the m/n ratio equal to 0.45, which is the central tendency of the concavity index across a large number of global landscapes (Kirby & Whipple, 2012; Gailleton et al., 2021; Tucker & Whipple, 2002). Although n is thought to take values other than unity in most landscapes (Lague, 2014; Harel et al., 2016), the value of this parameter is only man-

203 ifested in topographic outcomes during landscape transience (Whipple & Tucker, 1999;
 204 L. Royden & Perron, 2013) and does not affect our simulations since the landscapes are
 205 brought to steady state. When studying the channel steepness index across multiple basins,
 206 we set a reference value, θ_{ref} , (Gailleton et al., 2021) of 0.45 to establish a comparison
 207 between basins.

208 **2.1.2 Heterogeneous Lithologies**

209 To study the role of lithology in the prevalence of rainfall patterns we run a set of
 210 simulations with spatially varying values of erodibility, K . These simulations are designed
 211 to be closer to natural landscapes where the lithological landscape is more complex.

212 Within this study, we choose two lithological units reflecting the properties of a harder
 213 and a softer rock, with erodibility values ranging between $1e-7 < K < 5e-8$. This is
 214 in line with (Forte et al., 2016; Bernard et al., 2021; Peifer et al., 2021). Peifer et al. (2021),
 215 which determined that hard rocks can be related by a factor from 2-10 in erodibility to
 216 softer rocks (Forte et al., 2016; Bernard et al., 2021).

217 We simulate three heterogeneous lithologies scenarios: striped (a), sparse blob (b)
 218 and dense blob (c) lithologies (see SI, Figure S1).

- 219 1. **Striped lithology:** band of hard rock ($K = 5e - 8$) in the center of our sim-
 220 ulated mountain range, surrounded by soft rock ($K = 1e - 7$) to emulate cases
 221 like the Pyrénées.
- 222 2. **Sparse blob lithology:** 4 large hard rock ($K = 5e-8$) blobs evenly distributed
 223 on the landscape domain.
- 224 3. **Dense blob lithology:** many small hard rock blobs ($K = 5e-8$) of a few square
 225 meters in diameter, generated using Perlin noise (Perlin, 1985).

226 **2.1.3 Natural Landscapes**

227 We have chosen natural landscapes for this analysis on the basis of precipitation
 228 gradients and lithological structure, avoiding areas that have complex layers of soft rocks
 229 (Table 1). We analyze basins with a minimum drainage area of $1e7m^2$. We incorporate
 230 all channel pixels within tributaries that have a source area greater than $1.35km^2$ (which
 231 corresponds to 1500 pixels in topographic data with 30 m grid spacing).

Table 1. Geographical areas chosen along with the number of selected basins in each regions, area and rainfall range across the basin, from the outlet to the headwaters of the catchment. We choose a varied range of area sizes and precipitation gradients with to study prevalent trends across regions. Data extracted from the 30m Copernicus DEM and NASA’s Global Precipitation Measurement Mission (GPM) (Skofronick-Jackson et al., 2017).

Location	N basins	Area (km^2)	Precipitation Range (m/yr)
Andes, Southern Perú	5	29979	0.687-3.983
Andes, Northern Argentina	7	5932	0.045-0.010
North Qinling Mts, China	14	30832	0.734-0.938
Kaçkar Mts, Turkey	8	4279	0.784-1.673
Colorado Front Range, USA	7	9282	3.726-4.220
Alburz Mts, Iran	7	8167	0.357-0.849
Massif Central, France	5	1945	0.977-1.092
Pyrénées, Spain-France	5	6632	0.097-0.117

232 **2.1.4 Varying the simulation concavity index, θ (i.e. m/n ratio)**

233 We assess the impact of running the homogeneous lithology simulation with a fur-
 234 ther two choices of m/n : 0.35 and 0.55. The rationale for these experiments is to deter-
 235 mine if changes to the imposed m/n ratio causes distortions to k_{sn} of the same magni-
 236 tude as those induced by changing the incision rule. The broad effect on the landscapes
 237 with different values of m/n compared to the base case of $m/n = 0.45$ is that at 0.35 the
 238 landscape is smoother with lower relief and higher drainage density with sinuous trib-
 239 utaries, whereas at $m/n = 0.55$ the landscape has sharper features, with higher relief and
 240 lower drainage density, forming straighter tributaries. For detailed results of these sim-
 241 ulations, see SI (Text S6, Figures S16-S19, Tables S8-9).

242 **2.2 Metrics to quantify topographic outcomes**

243 Our models simulate river incision, and so we use river profiles to explore topographic
 244 outcomes of simulations. Because gradients should scale by either A or Q (depending
 245 on the incision rule) we use a coordinate transformation, first proposed by (L. H. Roy-
 246 den et al., 2000), that integrates either A or Q along the river profile:

247
$$\chi_A = \int_{x_0}^x \left(\frac{A_0}{A(x)} \right)^\theta dx \quad (5)$$

248
$$\chi_Q = \int_{x_0}^x \left(\frac{Q_0}{Q(x)} \right)^\theta dx \quad (6)$$

249 This transformation has various useful features. The gradient in χ_A -elevation space is
 250 equivalent to k_s if $A_0 = 1 \text{ m}^2$ (e.g., Perron & Royden, 2013; L. Royden & Perron, 2013;
 251 Mudd et al., 2014), and the gradient in χ_Q -elevation space is equivalent a metric k_{s-q}
 252 where gradient is scaled by Q instead of A in the form:

253
$$S = k_{s-q} Q^{-\theta} \quad (7)$$

254 when $Q_0 = \text{unity}$ in the units of Q used to calculate both χ_q and k_{s-q} (e.g., Adams et
 255 al., 2020; Leonard et al., 2023; Leonard & Whipple, 2021; D’Arcy & Whittaker, 2014;
 256 Harries et al., 2021). These steepness metrics can be used both in steady state and tran-
 257 sient landscapes (L. Royden & Perron, 2013). Another advantage of using the χ trans-
 258 formation is that tributaries to the main channel at the same elevation yield the same
 259 χ value, regardless of their drainage area. Given a landscape in steady state, the main
 260 channel and its tributaries should follow the same linear relationship on a χ - z plot, as-
 261 suming the same erosion and uplift rates (Perron & Royden, 2013) and the optimal con-
 262 cavity index value.

263 We exploit this latter feature in our efforts to discriminate, topographically, between
 264 incision rules. Regardless of the incision rule, selection of the incorrect value of θ will re-
 265 sult in tributaries that are not collinear, introducing distortions in channel steepness in-
 266 dex (Perron & Royden, 2013; Mudd et al., 2018; Hergarten & Robl, 2022; Gailleton et
 267 al., 2021; Goren et al., 2014; Harries et al., 2021). Computing χ_A or χ_Q also affects the
 268 channel steepness index values and the spread of the data, which can lead to different
 269 patterns of the channel steepness index and spreading the data in χ space (Figure 1).
 270 Because k_{sn} values are used to infer relative erosion rates across tectonically active re-
 271 gions, distortions to the spatial patterns of the channel steepness index can cloud inter-
 272 pretations of topographic pattern (e.g., Gailleton et al., 2021).

273 We quantify the spread of the χ - z profiles using a disorder metric, first proposed
 274 by Goren et al. (2014) and further developed by Hergarten et al. (2016) and Mudd et

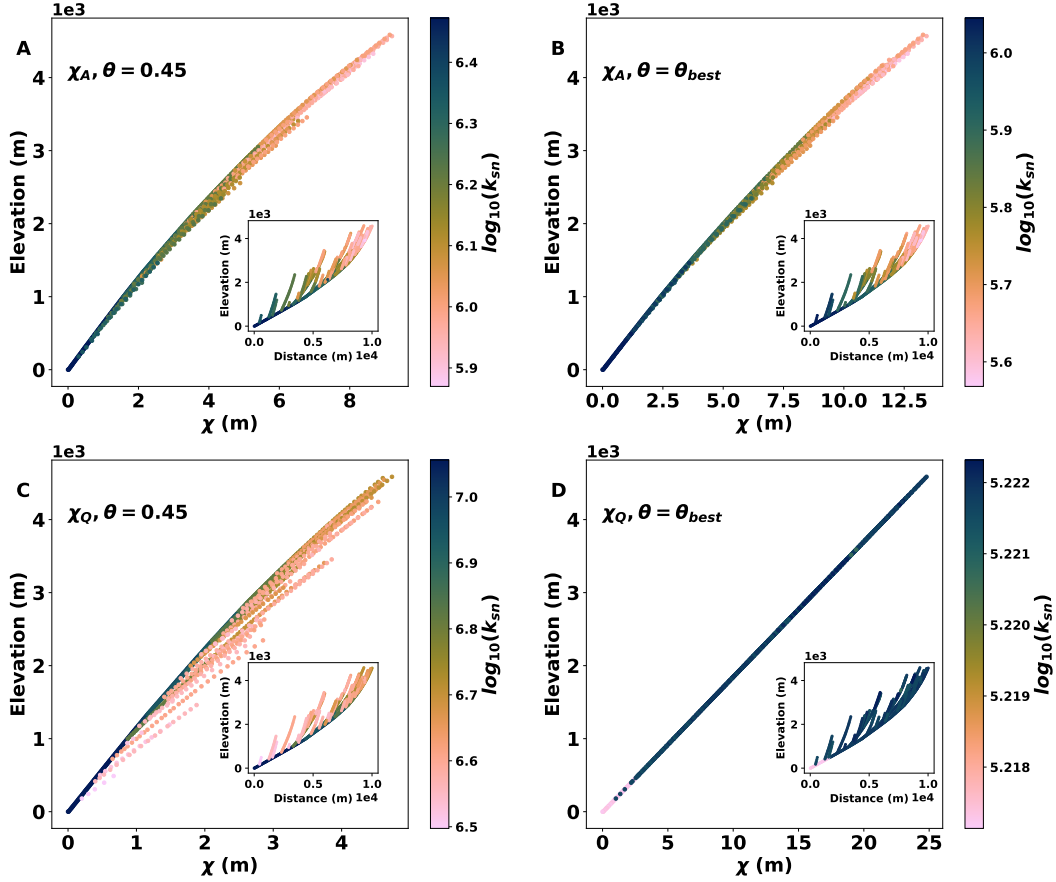


Figure 1. Illustration of how χ profiles and k_{sn} change based on the choice of incision scenario and concavity index values. The χ profiles result from simulations with a range of precipitation of 10m/yr (increasing west to east) under initial $m/n=0.35$. The basin shown is located on the wetter side of the domain, draining to the east. (D) shows perfect collinearity under χ_q and θ_{best} , which match the simulation parameters. (A) shows distortions using both the incorrect incision rule and the wrong θ , (B) shows a slightly more collinear profile, in this case only having the incorrect incision. (C) captures the correct incision (discharge) but uses $\theta=0.45$, where we see the largest increase in disorder and changes in k_{sn} .

275 al. (2018). One begins by ranking every point in the channel network by increasing el-
 276 levation, and then checks to see if the associated χ coordinates are similarly ranked (or
 277 not):

$$278 \quad R = \sum_{i=1}^N |\chi_{s,i+1} - \chi_{s,i}|, \quad (8)$$

279 where the the subscript s, i represents the i^{th} χ coordinate that has been sorted by its
 280 elevation ($\chi_{s,i}$). This sum, R , is minimal if elevation and χ are related monotonically.
 281 However it scales with the absolute values of χ , which are sensitive to the concavity in-
 282 dex (see equations 5 and 6), so following Hergarten et al. (2016) we scale the disorder
 283 metric, D , by the maximum value of χ in the tributary network (χ_{max}):

$$D(\theta) = \frac{1}{\chi_{max}(\theta)} \left(\sum_{i=1}^N |\chi_{s,i+1}(\theta) - \chi_{s,i}(\theta)| - \chi_{max}(\theta) \right). \quad (9)$$

We use the method of Mudd et al. (2018) to constrain uncertainty of this metric by creating subset networks formed from the trunk stream and every possible combination of three tributaries in a particular basin. This creates a population of D values for a given basin from which a median and interquartile range may be reported.

We normalize the disorder values across all tributary combinations, obtaining:

$$D^*(\theta) = \frac{D(\theta)}{D_{max}(\theta)} \quad (10)$$

where D_θ is the disorder for each tributary combination and $D_{max}(\theta)$ is the maximum disorder over all combinations.

In our analysis we aim to decipher whether we can identify the signal from a landscape shaped by rainfall *a posteriori*. To quantify this, we focus on the effect of rainfall in the $\chi - z$ profiles and in the disorder metrics. To emulate what the analysis would look like if we did not know the incision rule, we calculate the χ profiles in two ways for each simulation scenario - regardless of what the actual imposed incision rule is for a given numerical experiment. We calculate these metrics for each basin in the simulation draining to the edge and reaching the main drainage divide (Figure 2). For each of the basins simulated in each model scenario, we calculate the following:

1. χ_A : assumes a drainage area-driven incision (equation 5).
2. χ_Q : assumes a discharge-driven incision (equation 6).

For each of the χ cases, we calculate the disorder metric (equation 9). The disorder constrains the value for the optimal concavity index, θ_{best} , that will lead to the most collinear river profile configuration (Mudd et al., 2018; Gailleton et al., 2021).

2.3 Statistical Analysis

For each incision scenario, we calculate minimum normalized disorder values ($D^*(\theta)$) corresponding to each of the basins under each of the incision and χ scenarios. To measure if $D^*(\theta)$ for the basins in the simulations where incision is purely a function of A is statistically distinguishable from the basins where incision is driven by Q , we extract the value for $D^*(\theta)$ for each basin and χ case. We then calculate the absolute error between $D^*(\theta)$ in the two χ cases. The true value corresponds to calculating $D^*(\theta)$ with the χ of the matching incision scenario. The distribution of error values (ΔD^*) for all basins for each incision case can then be expressed as:

$$\Delta D^* = D_{rain}^* - D_{norain}^* \quad (11)$$

Since we are dealing with non-parametric distributions, we take the median of ΔD^* to quantify whether the A -based incision models may be distinguished from the Q -based incision models. We represent the distributions with kernel density estimates (KDE) (Cox, 2007; Silverman, 1998). If a percentage smaller than 5% is shared between the two distributions we consider them to be distinguishable from each other with 95% confidence.

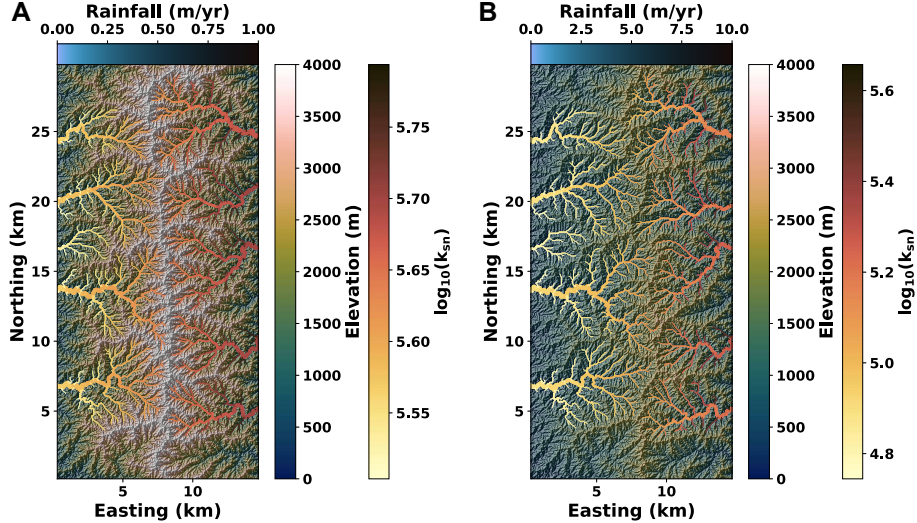


Figure 2. River networks generated with the numerical model under two discharge-driven incision scenarios, with rainfall ranges between (A) 0-1m/yr and (B) 0-10m/yr in the East-West direction. The smaller rainfall ranges in (A) lead to higher relief, steeper channels and a symmetric drainage divide. The higher rainfall in (B) leads to lower relief and a more sinuous and asymmetric drainage divide.

321

2.4 Measuring the effects of rainfall and θ on k_{sn}

322

323

324

325

326

327

328

329

330

331

In our numerical landscapes, we impose an erosion rule and then quantify the extent to which profiles are disordered when applying the appropriate or incorrect χ transformation (that is, using either A or Q). In real landscapes, however, we can only infer which of the two χ transformations is correct based upon relative disorder, and indeed neither may be correct. We resort to distortion in the χ -elevation profiles to quantify the impact of the choice of A or Q to scale χ when the correct choice is unclear. Specifically the distortion metrics quantify the degree to which k_{sn} changes if different choices in calculating χ are made. Determining the distortion of k_{sn} due to the choice of A or Q in calculating k_{sn} is important because it can affect the interpretations of the tectonic and erosional history of a landscape (Kirby & Whipple, 2012).

332

333

334

335

336

We quantify distortion by calculating the ratio between median upstream and downstream k_{sn} values and then investigating how this ratio varies depending on concavity index (Case *i*), incision scenario (Case *ii*) or both (Case *iii*), following the methods in (Gailleton et al., 2021). A full derivation of equations used to calculate the distortion is included in the SI, Text S1.

337

3 Results

338

339

340

In this section we present the numerical experiments and explore the effects of rainfall gradient on channel steepness and concavity index. We cover both homogeneous and heterogeneous lithologies.

341

3.1 Homogeneous lithology

342

3.1.1 Drainage area or discharge-driven incision?

343

344

345

346

347

348

Figure 3 shows the distributions of ΔD^* in each experiment using KDE fitting for Q -driven incision rule (equation 3) and A -driven incision rule (equation 2). Each kernel estimate is obtained for the collection of basins in the simulated domain. We obtain the median (solid line), 95th and 5th (dashed lines) percentiles for each kernel, repeating this procedure for each of the rainfall gradients. We consider $\Delta D^* = 0$ as the point where calculating χ_Q or χ_A would have no effect on the minimum disorder.

349

350

351

352

353

354

355

356

357

358

359

Figure 3 shows the distribution of ΔD^* values. Basins where the χ and the incision scenario match have lower D^* values. This is represented by the A -driven distributions lying on the negative side of the x-axis, meaning that the disorder value calculated using χ_A is lower than the disorder calculated using χ_Q . That is, unsurprisingly, using the version of χ that corresponds with the imposed incision rule results in less disordered channel profiles. The opposite is true of the Q -driven basins, which lie on the positive x-axis range, where the disorder is lower when calculating χ_Q than χ_A . This is true of all three indicated metrics: median, 95th and 5th percentiles. None of the distribution tails overlap inside of the 5-95th percentile ranges. For every rainfall distribution illustrated, the drainage area and the discharge driven incision are statistically far enough apart to be considered distinct distributions.

360

361

362

363

364

As rainfall gradients increase, the medians of the distributions diverge. For smaller rainfall gradients, the distribution medians appear closer together but still outside the 95% of each other that we consider an indication they are statistically distinct. The most significant differences arise from the discharge-driven scenarios, with the changes in the drainage area ΔD^* evolving slower with increased rainfall.

365

366

367

368

369

For every rainfall distribution illustrated under homogeneous lithology, calculating χ_Q or χ_A leads to statistically distinct ΔD^* distributions for the A and the Q -driven scenarios. Disorder can thus be used as a tool to recognize the dominating incision rule in numerical simulations: when $\Delta D^* < 0$, the incision is drainage area-driven, whereas $\Delta D^* > 0$ implies that discharge is the main incision mechanism.

370

3.1.2 k_{sn} distortion

371

372

373

374

We quantify k_{sn} distortion based on the cases outlined in section 2.4. We remind the reader of the three distortion cases we consider in this study *i*) change in θ , *ii*) change in incision rule, and *iii*) change in both. Similar patterns in changes in k_{sn} can arise from either of the three cases.

375

376

377

378

379

Figure 4 illustrates each of the distortion cases along a series of rainfall gradients for the discharge simulations. Panels A and B correspond to changes in θ (Case i). Panel C represents a change in incision rule (Case ii) and Panel D reflects a combined change in incision rule and θ values (Case iii). In all plots we indicate the no-distortion scenario at $y = 0$ with a solid black line.

380

381

382

383

384

385

386

387

388

389

Figure 4A reflects data from k_{sn-q} calculations, which capture the rainfall range used for the discharge-driven simulations. The associated distortion remains close to 1, indicating that using $\theta = 0.45$ as opposed to θ_{best} has minimal effects in the basin-averaged k_{sn} values. This can be explained by referring to the model set up. In the discharge-driven model with $m/n = 0.45$, with no other external factors to disturb equilibrium, we obtain steady state channel profiles with $\theta_{best} = 0.45$. This value is obtained from disorder minimization including rainfall in the calculations. Figure 4B reflects the results of not including a rainfall range in the disorder minimization procedure when calculating θ_{best} . Starting with a null distortion for the 0 m/yr rainfall range, distortion gradually increases with rainfall ranges. The distortion values reach 23% where $\theta_{best} > 0.45$

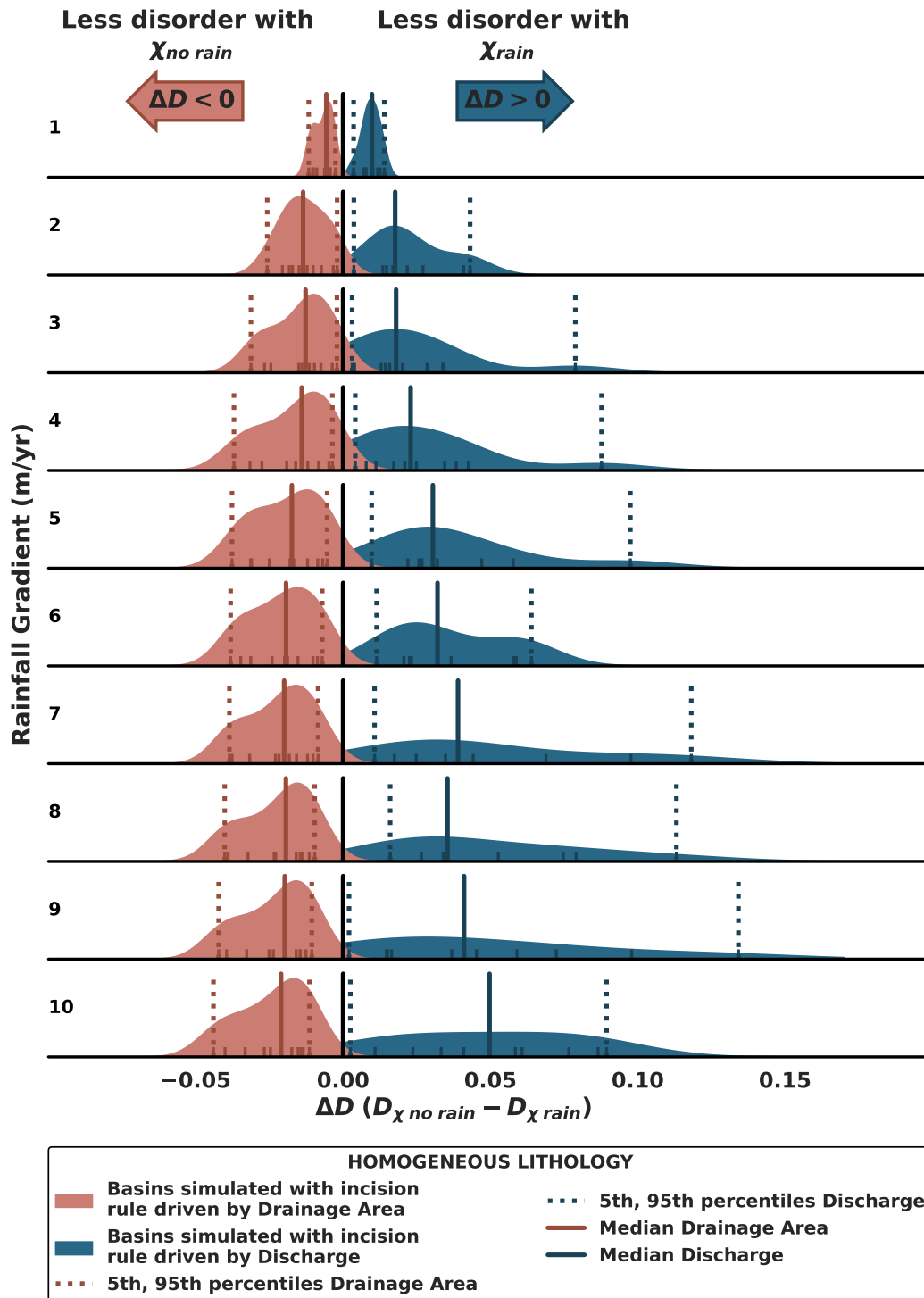


Figure 3. Comparison of the median values for ΔD^* for each of the rainfall gradients for A and Q -driven incision under homogeneous lithology for an initial $m/n=0.45$. The two models are always distinguishable: each of the distributions is on either side of the 0 line, with 95% confidence. The larger the rainfall gradient, the more separated the distribution medians become.

390 (above 1) and 15% when $\theta_{best} < 0.45$ (below 1). As the rainfall range increases, θ_{best}
 391 values diverge from 0.45. Figure 4C shows the distortion in case ii, which results from
 392 a difference in the assumed incision rule at a fixed concavity index ($\theta = 0.45$). The distortion
 393 pattern follows a similar path to Figure 4B: as rainfall ranges increase, so does
 394 the k_{sn} distortion. In this case, the values > 1 correspond to the windward (wetter) basins,
 395 where rainfall decreases as we move towards the mountain range. Distortion < 1 cor-
 396 responds to leeward (drier) basins where rainfall decreases as we move away from the
 397 mountain range. In both cases, distortion reaches 11%, with differences originating from
 398 the magnitude and the direction of the rainfall gradient. Figure 4D depicts distortion
 399 case iii: the effects of both a change in θ and a change in the incision rule. The percent-
 400 age of k_{sn} distortion is larger than in the other three scenarios: a 34% increase at the
 401 highest point against 23% and 11% in Figure 4B and C respectively. This arises from
 402 the basins having different θ_{best} depending on the incision rule used to calculate the k_{sn}
 403 distortion. The effect in the distortion is additive, meaning that compared to the cor-
 404 rect case for both incision and θ ($k_{sn-q}(\theta = \theta_{best})$), optimizing θ for the wrong inci-
 405 sion case would lead to the greatest distortion out of the three cases considered.

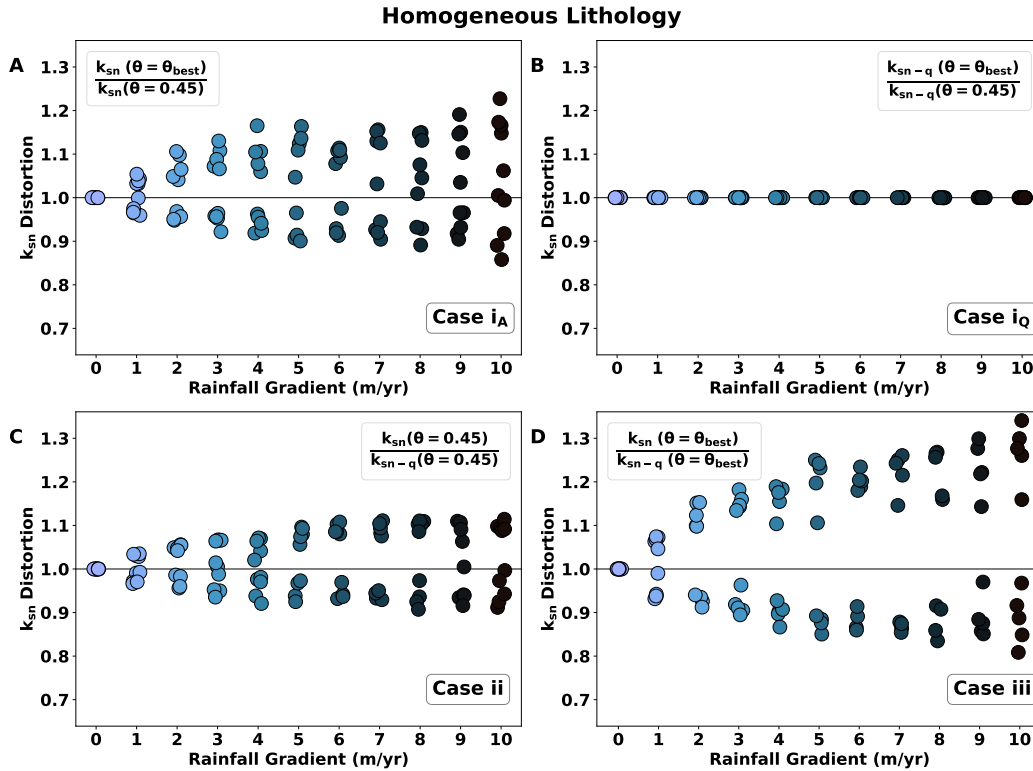


Figure 4. Distortion in k_{sn} for the Q -driven incision case under homogeneous lithology and initial $m/n=0.45$. A distortion of 1 (solid black line) keeps the value of k_{sn} unchanged. (B, Case i_Q) indicates that no k_{sn} distortion occurs when the concavity index and the incision case match the model scenario. (A), (C) and (D) show the possible distortion scenarios that one might encounter under different assumptions. (A) highlights the effects of optimizing concavity index under an incorrect incision scenario, (C) assumes concavity index is kept at 0.45 but the incision scenario changes and (D) comprises the effects of θ optimization under different assumptions of incision scenarios, where we see the largest k_{sn} distortions of up to 34%.

Distortion in the channel steepness index can be caused both by incorrectly assuming concavity indices and incorrectly assuming incision rules. That is, to calculate k_{sn} one must set a value of θ , and one must choose whether or not to incorporate a proxy for discharge, and either of these assumptions may not be the best reflection of reality in any given landscape. Optimizing θ will decrease the distortion in k_{sn} values, for cases when the incision mechanism is unknown. If we identify an incision mechanism, then distortion can also be decreased by using either k_{sn} or k_{sn-q} , depending on the case. However, we find that optimizing θ for an incorrect incision case leads to the highest distortion values.

3.2 Heterogeneous lithology

We have shown that it is possible to differentiate a signal from an A -driven incision scenario from a Q -driven scenario, under homogeneous lithology. However, many natural landscapes contain a range of lithologies with different erodibilities. We complement our analysis with data from simulations with heterogeneous lithologies, as described in Section 2.1.2. We illustrate the behavior from results from the most densely varying lithology (dense blob), with two extra cases (blob and striped lithology) included in the Supplementary Information.

In Figure 5 we see that in contrast with the homogeneous lithology case, we see that the disorder metrics derived from the A -driven and Q -driven basins are not statistically distinct. Both distribution medians are similar regardless of the rainfall range and they fall within each other's 95% percentile of the population. The more heterogeneous the erodibility, the harder it becomes to distinguish between the original incision rules. The dense blob lithology simulations feature channel metrics where it is most difficult to differentiate A -driven from Q -driven incision rules using, with other lithologic types having larger differences in median disorder (see Supplementary Information).

We also quantify how heterogeneous lithologies impact the distortion of k_{sn} values. We start by looking at the result of adding lithology to the discharge-driven model scenario and compare the results to Figure 4. We highlight that in the heterogeneous lithology cases, we do not expect θ to be 0.45 at a rainfall range of 0m/yr. We have introduced a perturbation, leading the system to diverge from $\theta = 0.45$ that we obtained in an unperturbed, steady state scenario. This is reflected in a distortion between 10% - 20% at rainfall ranges of 0 m/yr in all distortion cases. Irrespective of the range in rainfall, this distortion remains within the same bounds. We see consistently higher distortion values for all rainfall ranges in 6B, as a result of using the incorrect incision scenario when optimizing θ . In Figure 6C we see the distortion associated with Case ii (caused by changes in incision rule), when keeping $\theta = 0.45$. As the rainfall range increases, the distortion shifts towards being larger, up to 44% in leeward basins. When we optimize θ and compare between the two incision scenarios 6D, the distortion in both the windward and the leeward side is increasing at a similar rate with increasing rainfall ranges. This is the only distortion case where we see a systematic increase in distortion with rainfall ranges.

Heterogeneities in lithology add to the distortions in channel steepness index caused by rainfall ranges. The signal from the rainfall is reflected as a systematic increase in distortion in A -driven cases. In Q -driven scenarios the systematic increase of distortion with rainfall range is masked by the lithological heterogeneities when comparing between θ values. Optimizing θ will remove the distortion that we incorporate by using $\theta = 0.45$, which is more prominent in heterogeneous than homogeneous lithologies. Making a decision on the type of incision, will also reduce the distortion. However, this can end up with an increased distortion if the incision type assumed for calculating χ is incorrect and θ is subsequently optimized using channel information obtained from that incorrect incision type.

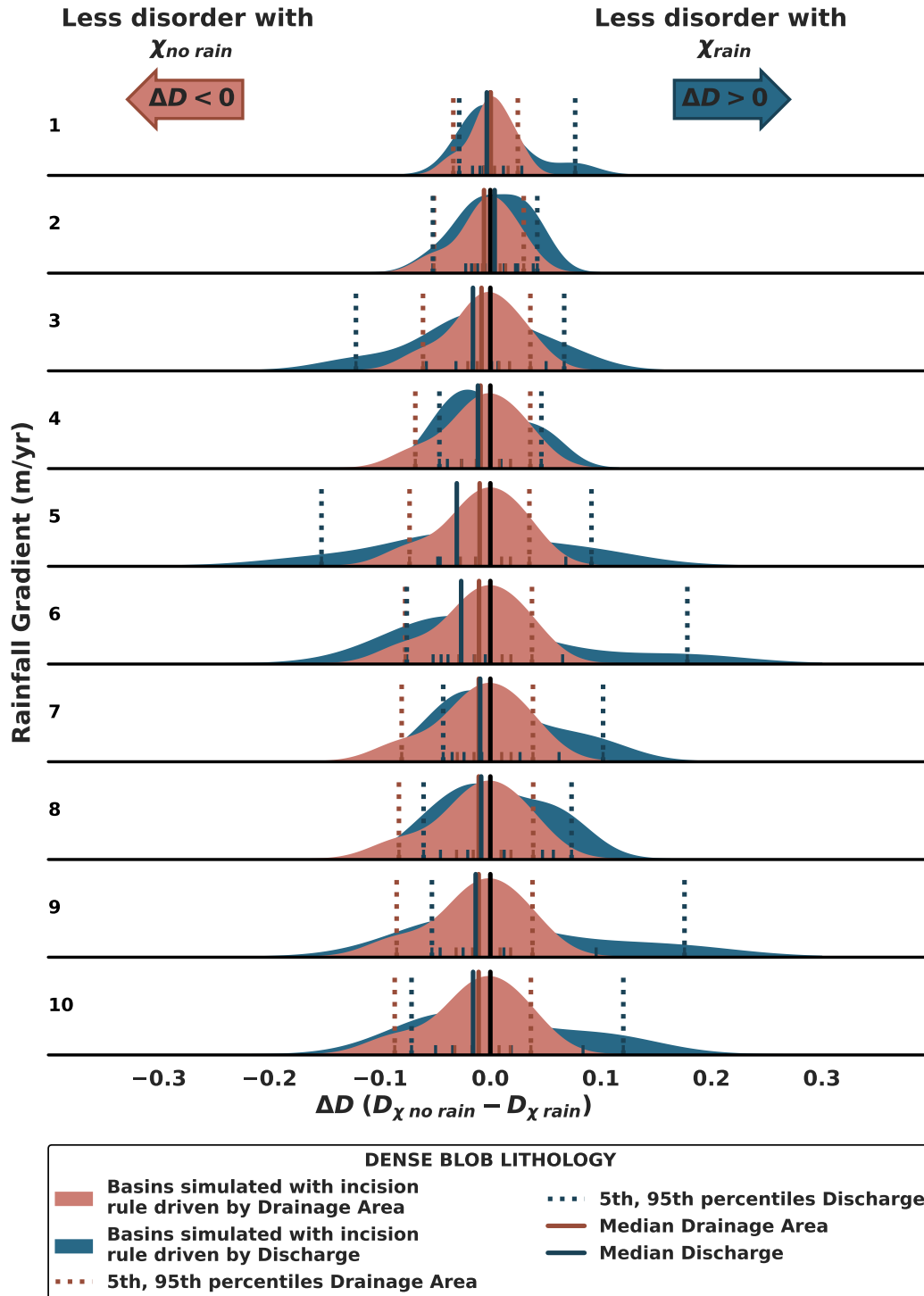


Figure 5. Comparison of the median values for ΔD^* for each of the rainfall ranges for A and Q -driven incision under dense blob lithology for an initial $m/n=0.45$. The distribution medians and percentiles largely overlap, meaning that the models are not distinguishable, regardless of the rainfall gradient.

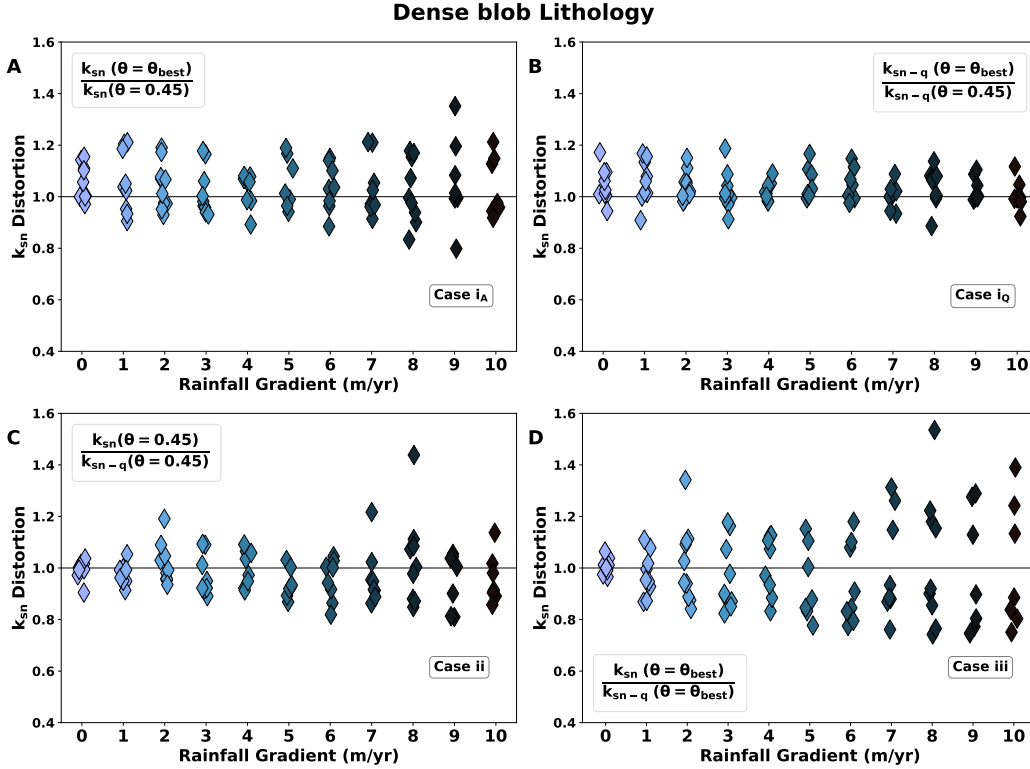


Figure 6. Distortion in k_{sn} for the Q -driven incision case under heterogeneous lithology and initial $m/n=0.45$. A distortion of 1 (solid black line) keeps the value of k_{sn} unchanged. We show the possible distortion scenarios that one might encounter under different assumptions of concavity index and incision. (A) highlights the effects of optimizing concavity under the incorrect incision scenario (drainage area), whereas (B) shows the distortion incurred by not optimizing θ under Q -driven incision. (C) keeps concavity index at 0.45 but compares incision scenario and (D) comprises the effects of θ optimization under different assumptions of incision scenarios, where we see the largest k_{sn} distortions of up to 54%.

457

3.3 Natural Landscape Study Cases

458

459

460

461

462

463

464

465

466

467

468

469

470

471

We have quantified how a changing range of rainfall can lead to differences in k_{sn} and θ_{best} under various incision scenarios in simulated landscapes. Our numerical experiments suggest that it is possible to statistically distinguish A -driven and Q -driven incision landscapes in a lithologically homogeneous model using disorder metrics. Heterogeneous lithologies capture how the rainfall signal is obscured by additional forcings, namely spatial variation in erodibility, a common feature in natural landscapes. Having isolated these signals in experiments, we now apply this knowledge to real landscapes, where we only have *a posteriori* topographic states from which to infer the landscape incision rule. We remind readers, when interpreting our results, that $D^*(\theta_{best,Q}) < D^*(\theta_{best,A})$ suggests that the basin has been shaped by rainfall as a main incision mechanism. On the other hand, $D^*(\theta_{best,Q}) > D^*(\theta_{best,A})$ suggests that basin incision is driven by drainage area. Our numerical experiments suggest that $\Delta D^* < 0$ in landscapes with A -driven incision. In Q -driven, $\Delta D^* > 0$. We calculate ΔD^* for natural landscapes in the same fashion.

472 For each basin, we repeat the calculations outlined in section 2.2, and plot the me-
 473 dian values of normalized distortion (ΔD^*) and their distributions in Figure 7. As a re-
 474 minder, this metric quantifies which of the two assumed incision scenarios results in lower
 475 distortion of the channel network. If all basins are positive, or all are negative, we view
 476 this as an indication that one of the two assumed incision signals better describes the
 477 observed topographic data. We see in Figure 7, most natural landscapes have basins that
 478 straddle $\Delta D^* = 0$, meaning that we cannot determine the most likely incision scenario
 479 with any confidence. Only in the cases of the Colorado Front Range and the Massif Cen-
 480 tral do we see a statistically significant imprint on ΔD^* . Those basins lie on the pos-
 481 itive side of the x-axis, favoring discharge as the predominant incision mechanism. The
 482 other sites show smaller confidence intervals in ΔD^* values, and their basins only a slight
 483 trend towards an incision scenario (drainage area -Pyrénées, Alburz, Qinling- and dis-
 484 charge -Perú, Argentina, Kaçkar-). The distributions center largely around the $\Delta D^* =$
 485 0 with spreads at either side of the incision case division.

486 If we are not able to distinguish the correct incision scenario using the disorder met-
 487 rics, how uncertain will our interpretations of channel steepness become? In Figure 8 we
 488 investigate distortions in the channel steepness index. We highlight the difference in scale
 489 of the results shown here. In the modeling experiments, some scenarios show a distor-
 490 tion of no more than 10% under low rainfall (eg. Figures 4A, S12B, S3 (A-C)). In real
 491 landscapes, we observe larger distortion values for all cases, in some instances reaching
 492 36% in 8D, 50% in 8B and above 75% distortion in 8A and C. In natural basins, using
 493 $\theta = 0.45$ becomes a large source of distortion to the channel steepness index, regard-
 494 less of the assumed incision scenario. This is a consequence of the θ_{best} values diverg-
 495 ing from 0.45, which corresponds to the m/n value of the models. Compared to these
 496 large distortion values incurred by using $\theta = 0.45$, the distortion values arising from
 497 choosing A -driven or Q -driven incision scenarios fall considerably. We see most distor-
 498 tion falls within the 25% bounds, regardless of the mountain range, although with dif-
 499 ferent amounts of spread around the null distortion line at $y = 1$. This shows that in
 500 natural landscapes, optimizing the concavity index is more important than choosing the
 501 correct incision scenario. As opposed to the model, in natural topography we do not see
 502 an increase in the distortion originated from case *iii* compared to the other two cases.

503 We plot the distributions of k_{sn} and k_{sn-q} for θ_{best} and $\theta = 0.45$. Under $\theta = 0.45$
 504 (9B), the differences in channel steepness index are larger, for instance in Argentina or
 505 Colorado, where the peak of the distribution is shifted and the distributions changing shape.
 506 However, cases such as the Pyrénées or the Massif Central show little differences in the
 507 distributions. 9A shows the channel steepness index distributions for θ_{best} . We see that
 508 the shape of the curves is better preserved, with less variation in the location of the peak
 509 between the A and the Q cases.

510 4 Discussion

511 4.1 Channel steepness index and Erosion Rates

512 Our numerical experiments show that in lithologically homogeneous landscapes it
 513 is possible to distinguish between drainage area and discharge-driven landscapes from
 514 topographic metrics alone. If the imposed incision law is discharge-driven, but channel
 515 steepness is calculated assuming an area-driven incision driver (that is, χ is calculated
 516 only taking A into account), the distortions to the channel steepness index can be as high
 517 as 34% within our simulations, with varying patterns depending on the lithology and the
 518 type of rainfall. Homogeneous lithology leads to k_{sn} distortion that increases monoton-
 519 ically with increasing rainfall ranges (Figure 4A, C, D), whereas heterogeneous litholo-
 520 gies totally overprint rainfall-related signals (see Figure 6A, B, C). Adding heterogeneous
 521 lithologies in the model simulations also induces a systematic increase in the disorder
 522 metric. This makes it harder to identify a pattern whereby a worker can clearly extract

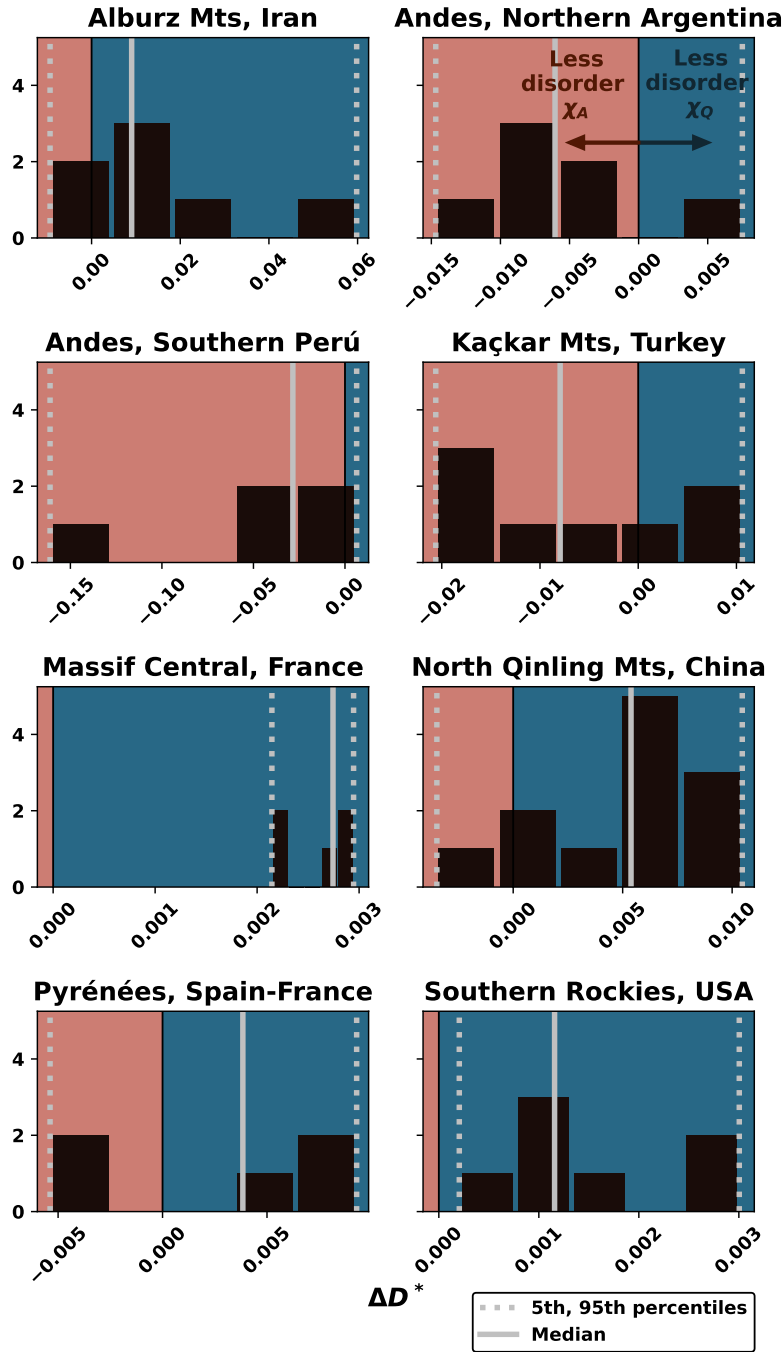


Figure 7. Comparison of the median values for ΔD^* for each of the mountain ranges. Results that lie above the $y=0$ line correspond to cases driven by rainfall. Points that lie below the $y=0$ line are cases where other forcings aside from rainfall (such as tectonics or lithology) are dominating over the rainfall signal. Some cases show a slight preference towards χ_A (Perú, Argentina, Turkey) whereas the rest prefer χ_Q . However, the confidence interval for this is lower than 95%, meaning that the results are largely basin dependent. Topographic analysis is not sufficient to draw conclusions about the incision mechanisms and further field observations of erosion rates would be needed.

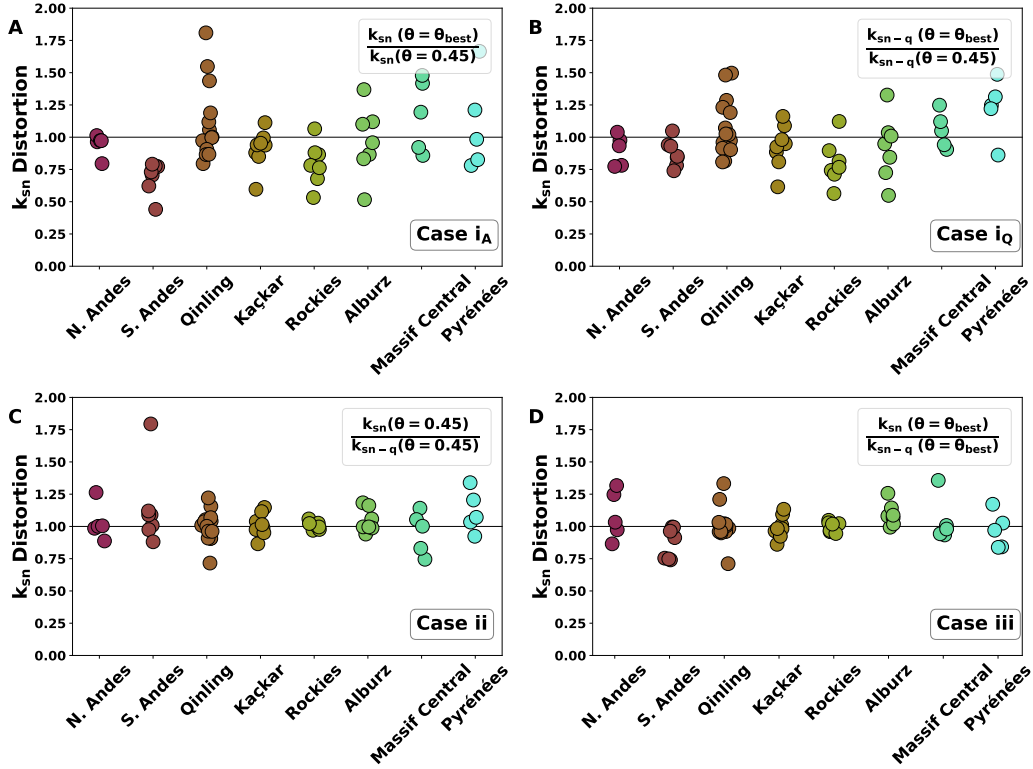


Figure 8. Distortion in k_{sn} for a range of natural landscapes. A distortion of 1 (solid black line) keeps the value of k_{sn} unchanged. The distortion scenarios are a representation of how one might introduce bias in k_{sn} under an unknown incision scenario, as is the case in many sites. Keeping $\theta=0.45$ under different incision scenarios can lead to distortions of up to 79% (C). We show as well the distortion introduced by choosing $\theta=0.45$ instead of θ_{best} , reaching 81% under A -driven incision (A) and 50% under Q -driven incision (B). (D) depicts the distortion introduced by optimizing θ under both incision regimes, with values of up to 36%.

523 the range of rainfall across the mountain range. For instance, in the striped lithology case
 524 (Figure S2, SI) all basins are affected by both the two erodibilities and the rainfall ranges,
 525 but at different parts of the catchment, because some tributaries will only have one rock
 526 type.

527 Distortions in channel steepness index are not solely caused by external forcings,
 528 such as rainfall or erodibility. In simulations depicted in Figure 4 we have imposed a discharge-
 529 driven incision rule, with a θ of 0.45. The largest distortions result from comparing the
 530 imposed incision law with the correct θ against the incorrect incision law with an opti-
 531 mized θ (Figure 4D). However, in a real landscape we will not know the “true” erosion
 532 law or the “true” value of θ , and we find that the distortions associated with changing
 533 the θ value between 0.45 (used in many studies) and an optimized θ is similar to the
 534 distortions introduced by not accounting for rainfall (Figure 4A and C).

535 A change in distortion is a reflection of differences between tributaries and trunk
 536 behavior as a result of spatial changes in rainfall. For instance, tributaries represent a
 537 larger percentage of the channels in smaller basins, meaning that their signal becomes
 538 amplified in those cases (Leonard et al., 2023). We then expect different parts of the catch-
 539 ment and channels of different sizes to react differently to spatially heterogenous rain-

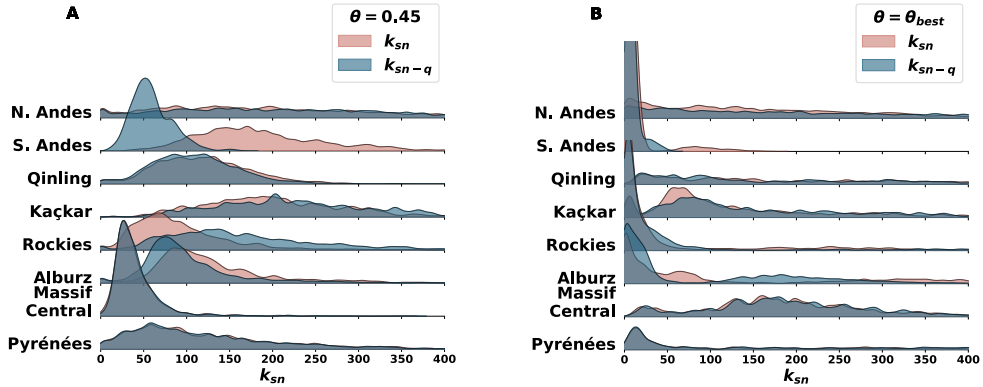


Figure 9. Distribution of k_{sn} and k_{sn-q} values for all the basins across each mountain range. Assuming $\theta=0.45$, we see large difference in k_{sn} values and distribution shape for the Southern Andes and the Rockies, other areas, such as the Massif Central or the Pyrénées do not experience significant changes. Under θ_{best} (B), the distribution largely changes from (A), shifting towards smaller channel steepness index. Mountain ranges like the Rockies now show a closer agreement between the k_{sn} and the k_{sn-q} distributions.

540 fall and lithology. According to the modeling work by Han et al. (2015), smaller chan-
 541 nels are more affected by rainfall, with large variability in k_{sn} reflecting the precipita-
 542 tion gradient. Recent work by Leonard et al. (2023) proposes that smaller catchments
 543 are more prone to biases because their contribution to the overall basin metrics is larger.
 544 In line with this, we have set bounds for basin drainage area size and minimum tribu-
 545 tary size. This will lead to more consistent k_{sn} values and avoid incorporating tributaries
 546 dominated by hillslope diffusivity processes. Our modeling results suggest that in Q -driven
 547 basins, given that the concavity index is optimized, the distortion will be minimal when
 548 using k_{sn-q} . This agrees with the study by Leonard et al. (2023), where in areas of
 549 the Andean Cordillera with strong rainfall gradients k_{sn-q} and $\theta_{ref} = 0.50$ yield a minimal
 550 distortion.

551 Natural topography, however, shows more complexity than our sandbox models,
 552 which leads to difficulties in identifying the different incision scenarios. We choose a small
 553 number of basins across a multitude of different areas (as opposed to (Leonard et al., 2023)),
 554 where the study is along a single geographical region) to identify topographic metrics
 555 than can differentiate between incision scenarios. This offers the worker an estimate of
 556 how much of a distortion they would introduce given the incorrect incision rule or con-
 557 cavities index. Leonard et al. (2023) also show that in the Andes, the differences between
 558 the trunk and tributaries are starker when using the incorrect incision mechanism than
 559 when comparing k_{sn} under different -incorrect- concavity index scenarios.

560 Determining the incision rule that is more consistent with observed topography will
 561 help in interpreting topography in areas with large changes in rainfall across the study
 562 area. The distortion that we have found in our study can then be translated into uncer-
 563 tainties in erosion rates. (Adams et al., 2020) found that the erosion rates from Be-10

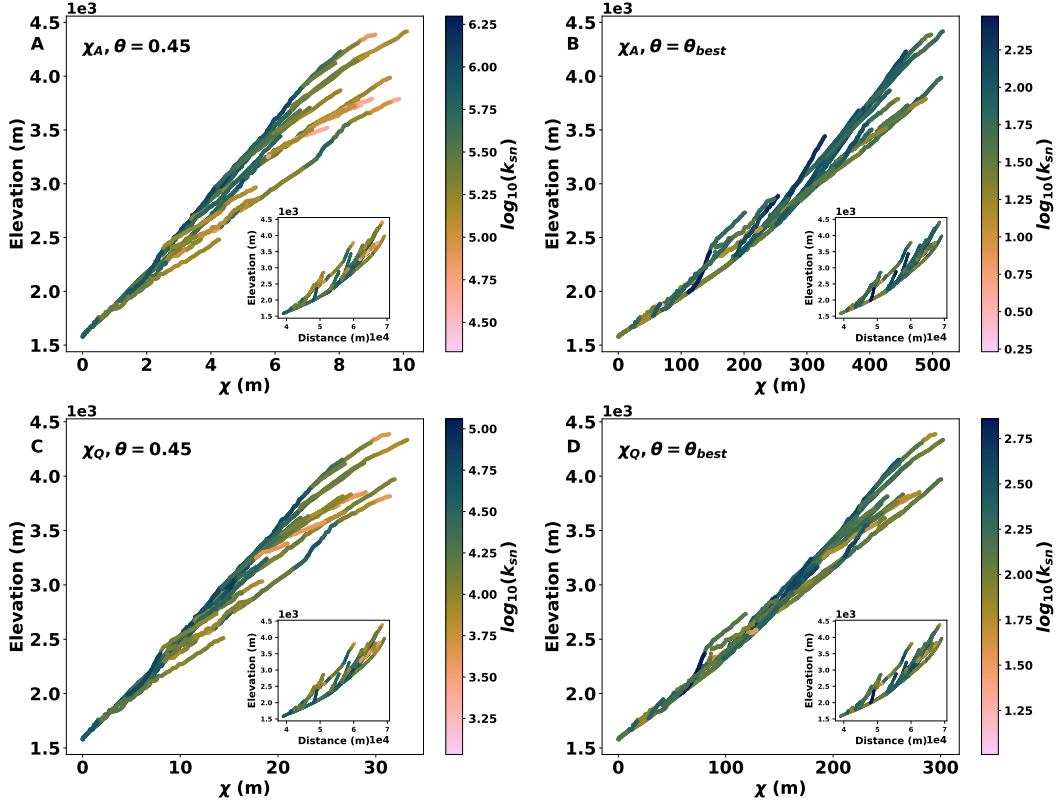


Figure 10. χ profiles for a basin in the Argentinian Andes, under different incision and concavity index scenarios. The disorder decreases when we optimize the concavity index (θ_{best}) ((B) and (D)). The channel steepness index is higher when $\theta=0.45$ ((A) and (C)). Compared to the effects that changes in concavity index have in the profiles, the choice of incision rule introduce secondary differences in the channels.

564 in the Himalayas and Bhutan are better constrained when using k_{sn-q} instead of k_{sn} (which
 565 (Leonard et al., 2023) corroborates), otherwise causing them to be artificially high. We
 566 find that changes in the concavity index can lead to changes in channel steepness index
 567 which are often larger than those caused by spatially varying rainfall, suggesting a po-
 568 tential cumulative effect of the different biases.

569 However, these changes in θ values are linked not only to different rainfall (Harries
 570 et al., 2021; Zaprowski et al., 2005) and lithological regimes (Duvall et al., 2004). The
 571 nature of the river bed (Howard & Kerby, 1983; Tucker & Whipple, 2002), the sediment
 572 availability (Wickert & Schildgen, 2019), and the tectonic setting (Kirby & Whipple, 2001)
 573 can also affect the value of θ in different reaches of the rivers in a way that would be-
 574 come hard to disentangle from spatial changes in rainfall. Han et al. (2015) explores changes
 575 that spatially varied rainfall can have on the concavity index through modeling exper-
 576 iments. In natural landscapes, changes around their chosen value of 0.5 vary compar-
 577 atively less due to rain gradients than changes caused by factors such as the type of chan-
 578 nel bed (Whipple & Tucker, 2002), sediment amounts (Gasparini et al., 2007) or uplift
 579 rate changes (Kirby & Whipple, 2001).

580 The distribution of k_{sn} and k_{sn-q} values for natural landscapes shows the variabil-
 581 ity in behavior between mountain ranges (Figure 9). For $\theta = \theta_{best}$, the variability be-
 582 tween k_{sn} and k_{sn-q} is smaller than for $\theta = 0.45$. This means that as long as the con-

583 cavity index has been constrained, the channel steepness index variations between A and
 584 Q -scenarios will be smaller than if $\theta = 0.45$ was chosen. We note that the mountain
 585 ranges where the distributions diverge for A and Q cases often correspond to the ones
 586 where the disorder is high, demonstrating once more that using unconstrained values of
 587 θ to extract geomorphometrics can amplify process-linked biases. For instance Ar-
 588 gentina shows consistently distortion between 25-75% in Figure 8, seeing some of the largest
 589 variability in channel steepness index for some of the basins. Plotting the χ -elevation plots
 590 for one of the basins with the strongest distortion Figure 10, we can see that the disorder
 591 of the tributaries with respect to the main stem is decreased the most when using
 592 χ_Q and $\theta = \theta_{best}$. Most of the changes in channel steepness index due to concavity in-
 593 dex optimization affect the upstream tributaries, we see as well how the profiles collapse
 594 more as a result of choosing θ_{best} than by including or removing rainfall in the calcula-
 595 tions.

596 4.2 Rainfall and climate

597 In this work, we have chosen to simplify the rainfall patterns in manner mirroring
 598 (Leonard & Whipple, 2021) by approximating the orographic behavior using a linear in-
 599 crease of rainfall with distance along the mountain range, emulating the effect that oro-
 600 graphic rainfall has on real landscapes. The rainfall asymmetry generates a displacement
 601 of the divide towards the drier side of the mountain, where the erosion is smaller. We
 602 observe different levels of channel steepness index distortion for the wet and the dry side
 603 of the simulated mountain ranges, and making it possible to identify the type of rain-
 604 fall gradient (top-heavy or bottom-heavy - following the nomenclature in (Leonard & Whip-
 605 ple, 2021)- from the value of the distortion ratio. This difference between the wet and
 606 the dry side of natural landscapes has been studied in depth in natural settings such as
 607 Hawai'i (Ferrier et al., 2013), albeit in tectonically complex regions outside our scope.

608 In the modeling framework, we have assumed that the rainfall pattern remains con-
 609 stant throughout time, but this is not necessarily the case in natural landscapes. Even
 610 small climate changes can lead to changes in the rainfall pattern and discharge amounts
 611 at different parts of the catchment, altering the local erosion rates and displacing the land-
 612 scape from an equilibrium state (Leonard & Whipple, 2021). The regions of study lie
 613 within the mid-latitudes, where the climate has remained largely unchanged (Roe et al.,
 614 2002). Changes in atmospheric circulation patterns or temperature changes (Herman et
 615 al., 2013; Bradley, 2015; Ward & Galewsky, 2014) are some examples of cases when other
 616 climate variable can affect erosion rates. Glaciations are also important when consider-
 617 ing a large portion of the Earth's landscapes, and they also show a relation with the ero-
 618 sion rates and the relief of the landscape. From our simulations, we have seen how the
 619 relief decreases as precipitation rates increase, as expected. In natural landscapes, the
 620 relationship between relief and rainfall is complex and influenced by local processes be-
 621 yond the scope of this project (Montgomery et al., 2001; Champagnac et al., 2012).

622 4.3 Disorder to indicate incision rate

623 Our hypothesis states that basins undergoing a strong rainfall gradient are distin-
 624 guishable based on their disorder values. This is true under homogeneous lithologies and
 625 in cases where the erodibility differences happen smoothly over the scale of multiple basins.
 626 In this case, it is possible to distinguish with 95% confidence between A -driven incision
 627 and Q -driven incision, regardless of the rainfall gradient. Adding sudden changes in lithol-
 628 ogy within basins and natural topographies makes identifying the correct incision rule
 629 challenging. The shape of the basins can have an effect on the disorder values. (Han et
 630 al., 2015) highlight how longer and narrower catchments experience a similar rainfall gra-
 631 dient between the tributaries and the trunk channel, whereas wider basins where the trib-
 632 utaries are more misaligned experience a higher disorder. In our experiments, we are look-
 633 ing at the overall behavior of the landscape, thus mixing basin shapes which would in-

trinsically have different disorders based on their shape, regardless of the forcing. Since in the disorder calculations we only compare each basin with itself under different incision scenarios, the intrinsic disorder differences between basins should not pose a bias.

4.4 Limitations

One of the limitations of our study lies in the precipitation treatment, both in the modeling study and in the natural landscapes. While it is possible to reproduce a realistic rainfall pattern using the Fastscape module adapted from (Smith & Barstad, 2004), it is computationally expensive and requires knowledge of the wind patterns of the region of interest, which change at different atmospheric layers. We assume that the orographic rainfall can be approximated in the modeling framework by a linear rainfall trend that does not change through the simulation, regardless of the relief (Roe et al., 2003). In real orographic rainfall scenarios, there would be a positive feedback between the rainfall and the topography, which our model does not capture.

In our natural sites, we also assume that the rainfall pattern, derived from the average rainfall from 20 years (2000-2020), is representative of the precipitation at that site throughout its history, in geologic timescales. Climate patterns have changed throughout the centuries driven by changes in atmospheric condition, solar irradiance, and biosphere and ocean changes (Bradley, 2015). The regions of study lie within the mid-latitudes, where the climate has remained largely unchanged (Roe et al., 2002). However, due to having taken into account data from the 21st century, recent changes in rainfall pattern due to human made climate change cannot be ruled out to have intervened in the data from the past years compared to data prior to industrial revolution.

The question of whether mean annual precipitation should be used to describe the climate of a region is also a highly debated topic, with studies suggesting that it is the storms and extreme events which contribute the most to mean annual precipitation and do the most erosive work (Sorensen & Yanites, 2019; DiBiase & Whipple, 2011; Deal et al., 2017, 2018; Rasmussen et al., 2016). Other studies prefer the use of mean annual precipitation (Leonard & Whipple, 2021; Adams et al., 2020; Rossi et al., 2016; Anders et al., 2006; D'Arcy & Whittaker, 2014; Gasparini & Whipple, 2014; Armitage et al., 2011), especially when capturing the erosion work longer climatic trend or incorporating it in long-term landscape evolution models.

In the modeling framework, many processes have been simplified. We have already mentioned the rainfall patterns, which is the main focus of this study. The representation of lithological units, the exclusion of sediment supply and the homogeneous uplift, have all been choices made to isolate the climatic signal as much as possible. We are also assuming that the detachment limited SPM forms a good basis for how rainfall interacts with uplift and erosion, which many studies support (e.g., Leonard et al., 2023; Leonard & Whipple, 2021; Adams et al., 2020; Gasparini & Whipple, 2014; Harries et al., 2021), while acknowledging it still does not fully explain all geomorphic processes at the landscape scale.

5 Conclusions

In this study, we explore whether it is possible to determine whether channel incision is most closely related to drainage area or discharge (or some proxy thereof) from topographic metrics alone. Many past papers quantify channel steepness calculated based on drainage area as an indicator of river incision rates (e.g., Kirby & Whipple, 2012; Harel et al., 2016), but now that precipitation records are more readily available (Skofronick-Jackson et al., 2017), we must question whether adding rainfall gradients to the equation will yield different topographic outcomes in river channels.

In a simple numerical model with homogeneous lithology, disorder metrics (Mudd et al., 2018; Gailleton et al., 2021; Goren et al., 2014) yield a clear distinction between A and Q -driven incision basins with a monotonic dependence on rainfall gradients. When the system is perturbed by adding areas with different erodibilities, the incision signal is obscured. However, including rainfall gradients is not the only way to distort a signal. We have quantified the effects that optimizing the concavity index θ can have in the channels, concluding that using the standard value of $\theta = 0.45$ amplifies the distortion caused by rainfall effects.

In natural landscapes, we cannot establish a general topographic rule to distinguish between A and Q -shaped basins. We find catchments that are better described by discharge and others by drainage area, in some cases with quite a stark contrast. Given that we are not able to separate those cases topographically, we quantify how much distortion we would introduce in channel steepness index if we failed to identify the incision mechanism. Our results suggest that in most basins we would see maximum changes in channel steepness index of up to 25%, which does not constitute enough to drastically change the interpretation of erosion rates across the landscape. We compare this to distortions in k_{sn} of 50% obtained from using $\theta = 0.45$ instead of optimizing the concavity index. We suggest readers to use θ_{best} as an efficient method to reduce distortions already introduced by an unknown incision mechanism.

6 Open Research

Analyses have been run using open source software (lsdtopotools v0.9, lsdtopotools). Precipitation data was retrieved using the package `gpm_precipitation_tools`. Visualization scripts and model workflows are available in the Github repository https://github.com/MarinaRuizSO/JGR_paper, which will be archived and assigned a doi if the manuscript is accepted for publication.

Acknowledgments

Funding for MRSO was provided by the Natural Environment Research Council (NERC NE/S007407/1). This research has been supported by the H2020 European Research Council (grant no. 803721). Perceptually uniform scientific color maps (Crameri, 2023) are used in this study to prevent visual distortion of the data and exclusion of readers with color-vision deficiencies (Crameri et al., 2020).

References

- Adams, B. A., Whipple, K. X., Forte, A. M., Heimsath, A. M., & Hodges, K. V. (2020). Climate controls on erosion in tectonically active landscapes. *Science Advances*, *6*, 3166–3182. doi: 10.1126/sciadv.aaz3166
- Anders, A. M., Roe, G. H., Hallet, B., Montgomery, D. R., Finnegan, N. J., & Putkonen, J. (2006). Spatial patterns of precipitation and topography in the Himalaya. *Special Paper of the Geological Society of America*, *398*, 39–53. doi: 10.1130/2006.2398(03)
- Armitage, J. J., Duller, R. A., Whittaker, A. C., & Allen, P. A. (2011). Transformation of tectonic and climatic signals from source to sedimentary archive. *Nature Geoscience*, *4*(4), 231–235. doi: 10.1038/ngeo1087
- Babault, J., Viaplana-Muzas, M., Legrand, X., Van Den Driessche, J., González-Quijano, M., & Mudd, S. M. (2018). Source-to-sink constraints on tectonic and sedimentary evolution of the western Central Range and Cenderawasih Bay (Indonesia). *Journal of Asian Earth Sciences*, *156*, 265–287. doi: 10.1016/j.jseaes.2018.02.004
- Baynes, E. R., Lague, D., Steer, P., Bonnet, S., & Illien, L. (2020). Sediment flux-

- 730 driven channel geometry adjustment of bedrock and mixed gravel–bedrock
 731 rivers. *Earth Surface Processes and Landforms*, 45(14), 3714–3731. doi:
 732 10.1002/esp.4996
- 733 Bernard, T., Sinclair, H. D., Gailleton, B., & Fox, M. (2021). Formation of Lon-
 734 gitudinal River Valleys and the Fixing of Drainage Divides in Response to
 735 Exhumation of Crystalline Basement. *Geophysical Research Letters*, 48(8),
 736 e2020GL092210. doi: 10.1029/2020GL092210
- 737 Bookhagen, B., & Burbank, D. W. (2006). Topography, relief, and TRMM-derived
 738 rainfall variations along the Himalaya. *Geophysical Research Letters*, 33(8),
 739 L08405. doi: 10.1029/2006GL026037
- 740 Bookhagen, B., & Strecker, M. R. (2008). Orographic barriers, high-resolution
 741 TRMM rainfall, and relief variations along the eastern Andes. *Geophysical
 742 Research Letters*, 35(6), L06403. doi: 10.1029/2007GL032011
- 743 Bovy, B., & Lange, R. (2023). *fastscape-lem/fastscape: Release v0.1.0*. Zenodo. doi:
 744 10.5281/ZENODO.8375653
- 745 Bradley, R. S. (2015). Climate and Climatic Variation. *Paleoclimatology*, 13–54. doi:
 746 10.1016/B978-0-12-386913-5.00002-8
- 747 Braun, J., & Willett, S. D. (2013). A very efficient O(n), implicit and par-
 748 allel method to solve the stream power equation governing fluvial inci-
 749 sion and landscape evolution. *Geomorphology*, 180–181, 170–179. doi:
 750 10.1016/j.geomorph.2012.10.008
- 751 Champagnac, J.-D., Molnar, P., Sue, C., & Herman, F. (2012). Tectonics, climate,
 752 and mountain topography. *Journal of Geophysical Research: Solid Earth*,
 753 117(B2). doi: 10.1029/2011JB008348
- 754 Cox, N. J. (2007). Kernel estimation as a basic tool for geomorphological data anal-
 755 ysis. *Earth Surface Processes and Landforms*, 32(12), 1902–1912. doi: 10.1002/
 756 esp.1518
- 757 Craddock, W. H., Burbank, D. W., Bookhagen, B., & Gabet, E. J. (2007). Bedrock
 758 channel geometry along an orographic rainfall gradient in the upper Marsyandi
 759 River valley in central Nepal. *Journal of Geophysical Research: Earth Surface*,
 760 112(3). doi: 10.1029/2006JF000589
- 761 Crameri, F. (2023). *Scientific colour maps*. Zenodo. doi: 10.5281/zenodo.8409685
- 762 Crameri, F., Shephard, G. E., & Heron, P. J. (2020). The misuse of colour in science
 763 communication. *Nature Communications*, 11. doi: 10.1038/s41467-020-19160-
 764 -7
- 765 D’Arcy, M., & Whittaker, A. C. (2014). Geomorphic constraints on landscape sen-
 766 sitivity to climate in tectonically active areas. *Geomorphology*, 204, 366–381.
 767 doi: 10.1016/j.geomorph.2013.08.019
- 768 Deal, E., Braun, J., & Botter, G. (2018). Understanding the Role of Rainfall and
 769 Hydrology in Determining Fluvial Erosion Efficiency. *Journal of Geophysical
 770 Research: Earth Surface*, 123(4), 744–778. doi: 10.1002/2017JF004393
- 771 Deal, E., Favre, A.-C., & Braun, J. (2017). Rainfall variability in the Himalayan oro-
 772 gen and its relevance to erosion processes. *Water Resources Research*, 53(5),
 773 4004–4021. doi: 10.1002/2016WR020030
- 774 DiBiase, R. A., & Whipple, K. X. (2011). The influence of erosion thresholds and
 775 runoff variability on the relationships among topography, climate, and erosion
 776 rate. *Journal of Geophysical Research: Earth Surface*, 116(F4), 4036. doi:
 777 10.1029/2011JF002095
- 778 DiBiase, R. A., Whipple, K. X., Heimsath, A. M., & Ouimet, W. B. (2010).
 779 Landscape form and millennial erosion rates in the San Gabriel Moun-
 780 tains, CA. *Earth and Planetary Science Letters*, 289(1–2), 134–144. doi:
 781 10.1016/J.EPSL.2009.10.036
- 782 Dunne, K. B. J., & Jerolmack, D. J. (2020). What sets river width? *Science Ad-
 783 vances*, 6(41), eabc1505. doi: 10.1126/sciadv.abc1505
- 784 Duvall, A., Kirby, E., Burbank, D., Duvall, C. ., Kirby, E., & Burbank, D. (2004).

- 785 Tectonic and lithologic controls on bedrock channel profiles and processes in
786 coastal California. *Journal of Geophysical Research: Earth Surface*, 109(F3),
787 3002. doi: 10.1029/2003JF000086
- 788 Ferrier, K. L., Huppert, K. L., & Perron, J. T. (2013). Climatic control of bedrock
789 river incision. *Nature*, 496(7444), 206–209. doi: 10.1038/nature11982
- 790 Finnegan, N. J., Sklar, L. S., & Fuller, T. K. (2007). Interplay of sediment supply,
791 river incision, and channel morphology revealed by the transient evolution of
792 an experimental bedrock channel. *Journal of Geophysical Research: Earth
793 Surface*, 112(F3). doi: 10.1029/2006JF000569
- 794 Flint, J. J. (1974). Stream gradient as a function of order, magnitude, and discharge.
795 *Water Resources Research*, 10(5), 969–973. doi: 10.1029/WR010i005p00969
- 796 Forte, A. M., Yanites, B. J., & Whipple, K. X. (2016). Complexities of landscape
797 evolution during incision through layered stratigraphy with contrasts in rock
798 strength. *Earth Surface Processes and Landforms*, 41(12), 1736–1757. doi:
799 10.1002/esp.3947
- 800 Fournier, A., Fussell, D., & Carpenter, L. (1982). Computer Rendering of Stochastic
801 Models. *Commun. ACM*, 25(6), 371–384. doi: 10.1145/358523.358553
- 802 Gailleton, B., Mudd, S. M., Clubb, F. J., Grieve, S. W., & Hurst, M. D. (2021).
803 Impact of Changing Concavity Indices on Channel Steepness and Divide Mi-
804 gration Metrics. *Journal of Geophysical Research: Earth Surface*, 126(10). doi:
805 10.1029/2020JF006060
- 806 Gasparini, N. M., & Brandon, M. T. (2011). A generalized power law approximation
807 for fluvial incision of bedrock channels. *Journal of Geophysical Research: Earth
808 Surface*, 116(2), 1–16. doi: 10.1029/2009JF001655
- 809 Gasparini, N. M., & Whipple, K. X. (2014). Diagnosing climatic and tectonic
810 controls on topography: Eastern flank of the northern Bolivian Andes. *Litho-
811 sphere*, 6(4). doi: 10.1130/L322.1
- 812 Gasparini, N. M., Whipple, K. X., & Bras, R. L. (2007). Predictions of steady
813 state and transient landscape morphology using sediment-flux-dependent river
814 incision models. *Journal of Geophysical Research*, 112(F3), F03S09. doi:
815 10.1029/2006JF000567
- 816 Gilbert, G. (1877). *Geology of the Henry Mountains* (Tech. Rep.). Washington,
817 D.C.: Government Printing Office.
- 818 Goren, L., Fox, M., & Willett, S. D. (2014). Tectonics from fluvial topography using
819 formal linear inversion: Theory and applications to the Inyo Mountains, Cal-
820 ifornia. *Journal of Geophysical Research: Earth Surface*, 119(8), 1651–1681.
821 doi: 10.1002/2014JF003079
- 822 Grujic, D., Govin, G., Barrier, L., Bookhagen, B., Coutand, I., Cowan, B., ... Naj-
823 man, Y. (2018). Formation of a Rain Shadow: O and H Stable Isotope Records
824 in Authigenic Clays From the Siwalik Group in Eastern Bhutan. *Geochemistry,
825 Geophysics, Geosystems*, 19(9), 3430–3447. doi: 10.1029/2017GC007254
- 826 Hack, J. T. (1960). Interpretation of erosional topography in humid temperate re-
827 gions. *American Journal of Science*, 258(A), 80–97.
- 828 Han, J., Gasparini, N. M., & Johnson, J. P. (2015). Measuring the imprint of oro-
829 graphic rainfall gradients on the morphology of steady-state numerical fluvial
830 landscapes. *Earth Surface Processes and Landforms*, 40(10), 1334–1350. doi:
831 10.1002/esp.3723
- 832 Harel, M. A., Mudd, S. M., & Attal, M. (2016). Global analysis of the stream power
833 law parameters based on worldwide ¹⁰Be denudation rates. *Geomorphology*,
834 268, 184–196. doi: 10.1016/j.geomorph.2016.05.035
- 835 Harries, R. M., Gailleton, B., Kirstein, L. A., Attal, M., Whittaker, A. C., & Mudd,
836 S. M. (2021). Impact of climate on landscape form, sediment transfer and the
837 sedimentary record. *Earth Surface Processes and Landforms*, 46(5), 990–1006.
838 doi: 10.1002/esp.5075
- 839 Hergarten, S., & Robl, J. (2022). The linear feedback precipitation model (LFPM

- 1.0) – a simple and efficient model for orographic precipitation in the context
of landform evolution modeling. *Geoscientific Model Development*, 15(5),
2063–2084. doi: 10.5194/gmd-15-2063-2022
- Hergarten, S., Robl, J., & Stüwe, K. (2016). Tectonic geomorphology at small catch-
ment sizes—extensions of the stream-power approach and the χ method. *Earth
Surface Dynamics*, 4, 1–9. doi: 10.5194/esurf-4-1-2016
- Herman, F., Seward, D., Valla, P. G., Carter, A., Kohn, B., Willett, S. D., & Ehlers,
T. A. (2013). Worldwide acceleration of mountain erosion under a cooling
climate. *Nature*, 504(7480), 423–426. doi: 10.1038/nature12877
- Howard, A. D. (1987). Modelling fluvial systems: rock-, gravel- and sand-bed chan-
nels. In K. Richards (Ed.), *River channels* (p. 69-94). Oxford: Basil Blackwell.
- Howard, A. D., & Kerby, G. (1983). Channel changes in badlands. *GSA Bulletin*,
94(6), 739–752. doi: 10.1130/0016-7606(1983)94<739:CCIB>2.0.CO;2
- Johnson, J. P. L., & Whipple, K. X. (2010). Evaluating the controls of shear
stress, sediment supply, alluvial cover, and channel morphology on experimen-
tal bedrock incision rate. *Journal of Geophysical Research: Earth Surface*,
115(F2). doi: 10.1029/2009JF001335
- Kirby, E., & Whipple, K. (2001). Quantifying differential rock-uplift rates
via stream profile analysis. *Geology*, 29(5), 415–418. doi: 10.1130/
0091-7613(2001)029<0415:QDRURV>2.0.CO;2
- Kirby, E., & Whipple, K. X. (2012). Expression of active tectonics in erosional land-
scapes. *Journal of Structural Geology*, 44, 54–75. doi: 10.1016/J.JSG.2012.07
.009
- Kummerow, C., Simpson, J., Thiele, O., Barnes, W., Chang, A. T., Stocker, E., ...
Nakamura, K. (2000). The status of the tropical rainfall measuring mission
(TRMM) after two years in orbit. *Journal of Applied Meteorology*, 39(12
PART 1), 1965–1982. doi: 10.1175/1520-0450(2001)040<1965:tsottr>2.0.co;2
- Lague, D. (2014). The stream power river incision model: Evidence, theory and be-
yond. *Earth Surface Processes and Landforms*, 39(1), 38–61. doi: 10.1002/esp
.3462
- Leonard, J. S., & Whipple, K. X. (2021). Influence of spatial rainfall gradients on
river longitudinal profiles and the topographic expression of spatially and tem-
porally variable climates in mountain landscapes. *Journal of Geophysical Re-
search: Earth Surface*, 126(12), e2021JF006183. doi: 10.1029/2021JF006183
- Leonard, J. S., Whipple, K. X., & Heimsath, A. M. (2023). Isolating climatic,
tectonic, and lithologic controls on mountain landscape evolution. *Science
advances*, 9(3), eadd8915. doi: 10.1126/sciadv.add8915
- Montgomery, D. R., Balco, G., & Willett, S. D. (2001). Climate, tectonics, and
the morphology of the Andes. *Geology*, 29(7), 579–582. doi: 10.1130/0091
-7613(2001)029<0579:CTATMO>2.0.CO;2
- Morisawa, M. E. (1962). Quantitative Geomorphology of Some Watersheds in the
Appalachian Plateau. *Geological Society of America Bulletin*, 73(9), 1025–
1046. doi: 10.1130/0016-7606(1962)73[1025:QGOSWI]2.0.CO;2
- Mudd, S. M., Attal, M., Milodowski, D. T., Grieve, S. W., & Valters, D. A. (2014).
A statistical framework to quantify spatial variation in channel gradients us-
ing the integral method of channel profile analysis. *Journal of Geophysical
Research: Earth Surface*, 119(2), 138–152. doi: 10.1002/2013JF002981
- Mudd, S. M., Clubb, F. J., Gailleton, B., & Hurst, M. D. (2018). How concave are
river channels? *Earth Surface Dynamics*, 6(2), 505–523. doi: 10.5194/ESURF
-6-505-2018
- Peifer, D., Persano, C., Hurst, M. D., Bishop, P., & Fabel, D. (2021). Growing to-
pography due to contrasting rock types in a tectonically dead landscape. *Earth
Surface Dynamics*, 9(2), 167–181. doi: 10.5194/ESURF-9-167-2021
- Perlin, K. (1985). Image synthesizer. *Computer Graphics (ACM)*, 19, 287–296. doi:
10.1145/325165.325247

- 895 Perron, J. T., & Royden, L. (2013). An integral approach to bedrock river profile
896 analysis. *Earth Surface Processes and Landforms*, *38*(6), 570–576. doi: 10
897 .1002/esp.3302
- 898 Pfeiffer, A. M., Finnegan, N. J., & Willenbring, J. K. (2017). Sediment supply con-
899 trols equilibrium channel geometry in gravel rivers. *Proceedings of the National*
900 *Academy of Sciences*, *114*(13), 3346–3351. doi: 10.1073/pnas.1612907114
- 901 Phillips, C. B., & Jerolmack, D. J. (2016). Self-organization of river channels as a
902 critical filter on climate signals. *Science*, *352*(6286), 694–697. doi: 10.1126/
903 science.aad3348
- 904 Rasmussen, K. L., Chaplin, M. M., Zuluaga, M. D., & Houze, R. A. (2016). Contri-
905 bution of Extreme Convective Storms to Rainfall in South America. *Journal of*
906 *Hydrometeorology*, *17*(1), 353–367. doi: 10.1175/JHM-D-15-0067.1
- 907 Roe, G. H., Montgomery, D. R., & Hallet, B. (2002). Effects of orographic precipi-
908 tation variations on the concavity of steady-state river profiles. *Geology*, *30*(2),
909 143–146. doi: 10.1130/0091-7613(2002)030<0143:EOOPVO>2.0.CO;2
- 910 Roe, G. H., Montgomery, D. R., & Hallet, B. (2003). Orographic precipitation and
911 the relief of mountain ranges. *Journal of Geophysical Research: Solid Earth*,
912 *108*(B6), 2315. doi: 10.1029/2001JB001521
- 913 Rossi, M. W., Whipple, K. X., & Vivoni, E. R. (2016). Precipitation and evapotran-
914 spiration controls on daily runoff variability in the contiguous United States
915 and Puerto Rico. *Journal of Geophysical Research: Earth Surface*, *121*(1). doi:
916 10.1002/2015JF003446
- 917 Royden, L., & Perron, J. T. (2013). Solutions of the stream power equation and ap-
918 plication to the evolution of river longitudinal profiles. *Journal of Geophysical*
919 *Research: Earth Surface*, *118*(2), 497–518. doi: 10.1002/jgrf.20031
- 920 Royden, L. H., Clark, M. K., & Whipple, K. X. (2000). Evolution of river elevation
921 profiles by bedrock incision: Analytical solutions for transient river profiles
922 related to changing uplift and precipitation rates. *Eos Trans. AGU*, *81*(48),
923 *Fall Meet. Suppl., Abstract T62F-09*. doi: 10.1002/eost.v81.16
- 924 Silverman, B. W. (1998). *Density estimation for statistics and data analysis*. Rout-
925 ledge. doi: 10.1201/9781315140919
- 926 Skofronick-Jackson, G., Petersen, W. A., Berg, W., Kidd, C., Stocker, E. F.,
927 Kirschbaum, D. B., ... Wilheit, T. (2017). The global precipitation mea-
928 surement (GPM) mission for science and Society. *Bulletin of the American*
929 *Meteorological Society*, *98*(8), 1679–1695. doi: 10.1175/BAMS-D-15-00306.1
- 930 Smith, R. B., & Barstad, I. (2004). A linear theory of orographic precipi-
931 tation. *Journal of the Atmospheric Sciences*, *61*(12), 1377–1391. doi:
932 10.1175/1520-0469(2004)061<1377:ALTOOP>2.0.CO;2
- 933 Sorensen, C. S., & Yanites, B. J. (2019). Latitudinal trends in modern fluvial ero-
934 sional efficiency along the Andes. *Geomorphology*, *329*, 170–183. doi: 10.1016/
935 j.geomorph.2018.12.030
- 936 Tucker, G. E., & Whipple, K. X. (2002). Topographic outcomes predicted by stream
937 erosion models: Sensitivity analysis and intermodel comparison. *Journal of*
938 *Geophysical Research: Solid Earth*, *107*(B9), 1–1. doi: 10.1029/2001JB000162
- 939 Ward, D. J., & Galewsky, J. (2014). Exploring landscape sensitivity to the Pacific
940 Trade Wind Inversion on the subsiding island of Hawaii. *Journal of Geophysi-
941 cal Research: Earth Surface*, *119*(9), 2048–2069. doi: 10.1002/2014JF003155
- 942 Whipple, K. X., & Tucker, G. E. (1999). Dynamics of the stream-power river in-
943 cision model: Implications for height limits of mountain ranges, landscape
944 response timescales, and research needs. *Journal of Geophysical Research:
945 Solid Earth*, *104*(B8), 17661–17674. doi: 10.1029/1999JB900120
- 946 Whipple, K. X., & Tucker, G. E. (2002). Implications of sediment-flux-dependent
947 river incision models for landscape evolution. *Journal of Geophysical Research:
948 Solid Earth*, *107*(B2), 3–1. doi: 10.1029/2000JB000044
- 949 Wickert, A. D., & Schildgen, T. F. (2019). Long-profile evolution of transport-

- 950 limited gravel-bed rivers. *Earth Surface Dynamics*, 7(1), 17–43. doi: 10.5194/
951 ESURF-7-17-2019
- 952 Wobus, C. W., Tucker, G. E., & Anderson, R. S. (2006). Self-formed bedrock
953 channels. *Geophysical Research Letters*, 33(18), 18408. doi: 10.1029/
954 2006GL027182
- 955 Wobus, C. W., Tucker, G. E., & Anderson, R. S. (2010). Does climate change create
956 distinctive patterns of landscape incision? *Journal of Geophysical Research:*
957 *Earth Surface*, 115(4). doi: 10.1029/2009JF001562
- 958 Zaprowski, B. J., Pazzaglia, F. J., & Evenson, E. B. (2005). Climatic influences
959 on profile concavity and river incision. *Journal of Geophysical Research: Earth*
960 *Surface*, 110(F3), 3004. doi: 10.1029/2004JF000138

1 **Can we use topography to differentiate between area**
2 **and discharge-driven incision rules, and if not how bad**
3 **are our estimates of channel steepness?**

4 **Marina Ruiz Sánchez-Oro¹, Simon M. Mudd¹, and Boris Gailleton²**

5 ¹School of GeoSciences, University of Edinburgh, Edinburgh, UK
6 ²CNRS - Geosciences Rennes, Université de Rennes, France

7 **Key Points:**

- 8 • Discharge-driven incision can be identified *a posteriori* in simulated landscapes
9 but not in natural topography.
10 • The choice of concavity index (θ) can distort the channel steepness index more
11 than the choice of incision type.
12 • Topographic metrics should be accompanied by field explorations to fully describe
13 the erosional history of a landscape.

Corresponding author: Marina Ruiz Sánchez-Oro, marina.ruiz.so@ed.ac.uk

Abstract

The rate of channel incision in bedrock rivers is often described using a power law relationship that scales erosion with drainage area. However, erosion in landscapes that experience strong rainfall gradients may be better described by discharge instead of drainage area. In this study we test if these two end member scenarios result in identifiable topographic signatures in both idealized numerical simulations and in natural landscapes. We find that in simulations using homogeneous lithology, we can differentiate *a posteriori* between drainage area and discharge-driven incision scenarios by quantifying the relative disorder of channel profiles, as measured by how well tributary profiles mimic both the main stem channel and each other. The more heterogeneous the landscape becomes, the harder it proves to identify the disorder signatures of the end member incision rules. We then apply these indicators to natural landscapes, and find, among 8 test areas, no clear topographic signal that allows us to conclude a discharge or area-driven incision rule is more appropriate. We then quantify the distortion in the channel steepness index induced by changing the incision rule. Distortion in the channel steepness index can also be driven by changes to the assumed reference concavity index, and we find that distortions in the normalized channel steepness index, frequently used as a proxy for erosion rates, is more sensitive to changes in the concavity index than to changes in the assumed incision rule. This makes it a priority to optimize the concavity index even under an unknown incision mechanism.

Plain Language Summary

Rivers erode into mountains as a result of both the sediment transported as the water flows downstream and the amount of water that the river transports. The amount of rainfall that each part of the river receives affects how much the channel cuts into the rock. In this study, we assess whether it is possible to differentiate between rivers where sediment is responsible for most of the erosion work and rivers where rainfall has a larger erosive power. Through computer simulations, we measure the river fingerprint in the landscape through calculations involving how tributary and main channel slopes compare, and how quickly a channel steepens as it travels away from the headwaters. We extract these fingerprints and search for them in the more complex natural landscapes, measuring how much they change under heavy rainfall. We find that these fingerprints are camouflaged by factors such as changes in rock types, making it a challenge to identify them without field observations.

1 Introduction

Physical intuition suggests that, if all other factors are equal, a steeper river will erode faster than a gentler one. This basic relationship has been proposed by geomorphologists for over a century (Gilbert, 1877). It is unusual, however, to find two channels identical in their properties with the exception of their gradient. Headwaters are, for example, frequently steeper than downstream rivers they feed. In the early 1960s geomorphologists realized that gradient could be related to drainage area in a power law with a negative exponent (Hack, 1960; Morisawa, 1962). This basic relationship was formalized by Flint (1974):

$$S = k_s A^{-\theta} \quad (1)$$

where the concavity index, θ , describes how fast the gradient of the river changes downstream and the constant k_s , channel steepness index, describes the dependence of gradient normalized for drainage area. We can further fix the value of θ to a fixed reference value (θ_{ref}), after which we denote the channel steepness index with k_{sn} . This normal-

61 ization allows us to compare the relative steepness of rivers with different drainage ar-
62 eas (Flint, 1974).

63 Numerous studies have found that this relative steepness (k_{sn}) is positively cor-
64 related with measured erosion rates in upland landscapes (Wobus et al., 2006; DiBiase
65 et al., 2010; Kirby & Whipple, 2012; Harel et al., 2016; Adams et al., 2020; Gailleton et
66 al., 2021; Harries et al., 2021; Peifer et al., 2021). In regions without data on erosion rates
67 we might therefore use k_{sn} as a proxy for erosion rate (Kirby & Whipple, 2012). This
68 is not quite as straightforward as it sounds, however. If we return to physical intuition,
69 consider two channels with all properties equal apart from the amount of water they con-
70 vey (quantified as, e.g., their mean annual discharge or some other statistical represen-
71 tation of runoff). Many authors have proposed relationships between channel incision
72 and the physical properties of bedrock rivers, and these proposals include the influence
73 of sediment supply (dependent on A), sediment transport capacity (dependent on hy-
74 draulic conditions and gradient), shear stress (dependent on flow depth, and thus hy-
75 draulic conditions), stream power (again, hydraulic conditions), and thresholding behav-
76 ior of all the above factors (Howard, 1987; Wobus et al., 2010; Finnegan et al., 2007; John-
77 son & Whipple, 2010; Baynes et al., 2020). This means that computation of k_{sn} based
78 on drainage area rather than hydraulic conditions (e.g., discharge) may not represent the
79 incision process.

80 One reason erosion rate proxies have tended towards using an area-based k_{sn} is
81 because drainage area is trivial to extract from topographic data. Discharge (Q) records
82 are not always easy to obtain, and gauging stations are at points rather than distributed
83 throughout the landscape. However, various global datasets, for example TRMM (Kummerow
84 et al., 2000) and GPM (Skofronick-Jackson et al., 2017) have made it relatively simple
85 to estimate and aggregate precipitation over a basin, over a variety of timescales, which
86 means it is now quite simple to obtain an estimate of discharge in a basin given a lin-
87 ear relationship between aggregate precipitation and discharge.

88 These precipitation datasets enable us to calculate the channel steepness index, k_{sn} ,
89 based on effective discharge rather than drainage area. And indeed, a number of recent
90 authors have taken this approach (e.g., Babault et al., 2018; Adams et al., 2020; Leonard
91 & Whipple, 2021; Harries et al., 2021; Leonard et al., 2023). If precipitation rates are
92 uniform across a catchment, the drainage area-gradient relationship will have the same
93 spatial pattern as the drainage area-discharge relationship. But rainfall can be influenced
94 by mountains (Roe et al., 2002; Anders et al., 2006; Bookhagen & Burbank, 2006; Bookha-
95 gen & Strecker, 2008; Craddock et al., 2007; Gasparini & Whipple, 2014), meaning that
96 the patterns of k_{sn} might be different if one uses A or a more direct estimate of Q that
97 incorporates spatially varied precipitation.

98 One might assume that the latter is always “better” than the former. But there
99 are some reasons why erosion rates, and gradients, might be more sensitive to drainage
100 area than discharge. The main reason for this is that water does not erode the bed of
101 rivers, sediment does. And the amount of sediment fluxing through any part of the chan-
102 nel in a steadily uplifting mountain range should depend on drainage area and not dis-
103 charge. In addition, rivers transporting gravel will alter their geometry, for example their
104 width (Dunne & Jerolmack, 2020; Phillips & Jerolmack, 2016; Pfeiffer et al., 2017), to
105 accommodate sediment supply and this could cause a damping effect on the relationship
106 between discharge and erosion rates. So although it intuitively might make sense to al-
107 ways use discharge-based calculations of k_{sn} , we are not, at present, certain if this is bet-
108 ter than a calculation using A .

109 Any proposed erosion rule, be it area or discharge driven, can be transformed into
110 a prediction of topography. For example, the most basic erosion law incorporating gra-
111 dient and area of takes the form (Howard & Kerby, 1983):

112

$$E = KA^m S^n \quad (2)$$

113

114

115

116

117

118

119

120

121

122

123

where K is an erodibility and m and n are empirical coefficients. If one rearranges equation 2 to isolate S and compares the result with equation 1, one can see that, if equation 2 is correct, $k_{sn} = (E/K)^{1/n}$ and $\theta = m/n$. Thus equation 2 predicts a power law relationship between gradient and drainage area where erosion rates are invariant in time and space. It can also be shown that this power law relationship holds in segments of constant erosion that move upstream in transiently eroding landscapes (L. Royden & Perron, 2013). Various threshold models have been proposed as more complex versions of equation 2, but much of their relevant behavior can be captured by altering the n exponent (Gasparini & Brandon, 2011). While this approach is not without controversy (Lague, 2014), it is at least not clearly falsified by relationships between topographic data and measured erosion rates.

124

125

126

127

128

129

130

131

132

Such topographic predictions suggest a basic test: if there are strong gradients in precipitation, we expect the topographic outcomes of incision rules that are driven by either A or Q to differ. In this contribution we first explore the question: if we know erosion rates are driven by either A or Q , could we tell the difference just based on topography? We use numerical experiments to answer this question. We explore the extent to which heterogeneity in uplift rates and erodibilities can cloud this signal. Finally, we explore real landscapes to see if we can find locations, based on our proposed metrics, where it is clear that an area-based or discharge-based calculation of k_{sn} is more appropriate.

133

2 Methods

134

135

136

137

138

139

140

Our study includes three components. First, we perform a series of numerical experiments using a simple landscape evolution model with different imposed incision rules, and in addition alter other model parameters such as rainfall gradient. The aim of these simulations is to produce landscapes under idealized and controlled conditions against which metrics for determining the most likely incision rule may be tested. We then develop metrics that allow us to test if a particular incision rule better describes observed topography. Finally, we deploy these metrics on real landscapes.

141

2.1 Numerical simulations

142

143

144

145

146

We simulate landscapes where bedrock channels incise through an uplifting landscape. We thus must select an incision rule for our simulations. For the purposes of simplicity, we use the basic form of the stream power incision model (equation 2), which can emulate different incision mechanisms by altering the n exponent (Gasparini & Brandon, 2011).

147

148

149

150

Equation 2 is not influenced by discharge. For discharge-based incision, we follow other authors (e.g. Adams et al., 2020) and replace drainage area with a proxy for discharge, which we compute with the substitution $Q = A \times \text{Rainfall}$ where the rainfall is converted into runoff and accumulated downstream, yielding:

151

$$E = K_{lp} Q^m S^n. \quad (3)$$

152

153

In reality, the discharge will be modulated by other features such as evapotranspiration and infiltration rates, but these factors are subsumed into the parameter K_{lp} .

154

The model then simulates topographic evolution with a simple mass balance:

$$\frac{\partial z}{\partial t} = U - E \quad (4)$$

where U is the uplift rate and the erosion rate, E , is solved by either equation 2 or 3. Simulations are performed using the FastScape framework (Bovy & Lange, 2023). FastScape uses the methods developed by Braun and Willett (2013) that takes advantage of graph theory to efficiently solve equations 2 (or 3) with an implicit finite different scheme.

In order to implement equation 3, we must assign a precipitation pattern. In our experiments, we explore different precipitation gradients. Models do exist where precipitation depends on elevation and prevailing wind direction, for example the model of Smith and Barstad (2004) which was used by Han et al. (2015). Such models involve multiple parameters, and to obtain the desired precipitation gradient one must engage in fine tuning each of these parameters. For consistency across experiments, we decided instead to increase precipitation linearly as a function of distance from the mountain front, with precipitation gradients comparable to real orographic rainfall gradients. Leonard and Whipple (2021) found that a linear rainfall gradient can be a good approximation to studying orographic precipitation patterns in natural landscapes.

We impose rainfall gradients that will mimic natural orographic patterns found in natural landscapes. In the driest scenario, we impose a rainfall gradient across the simulated mountain range of 1 m/yr (that is, the precipitation is 1 m/yr greater at the peak rainfall location than at the minimum rainfall location). In our wettest scenario, the increase in rainfall reaches 10 m/yr across the simulation domain, corresponding to the highest rainfall achieved in the Bhutan Himalayas (Grujic et al., 2018; Anders et al., 2006).

2.1.1 Homogeneous Lithologies

We run experiments on a regular grid ($\Delta x = 30m$) grid over a mountain range that is 15 km by 30 km (see Table 1 in S1 for full parameter details). This size was selected as a compromise between the number of basins that could be formed during a simulation and computational expense. We begin each landscape with a random surface generated using the diamond square algorithm (Fournier et al., 1982; Perron & Royden, 2013) with noise ranging from 0 to 1 m. We choose this initial condition as it produces a greater variety of channel network structures than the more widely used white noise. Each simulation is run to steady state, where the change in erosion is balanced by uplift.

For a given uplift and precipitation gradient, we calculate the landscape resulting from each of the two incision laws as described by equations 2 and 3. Initial experiments use uniform erodibility to simulate homogeneous lithology. The boundary conditions include a fixed elevation on the east and west edges (which allow flux to exit the model) and periodic boundaries at the north and south of the model domain. The resulting mountain range emerges in the North-South direction.

Within the discharge-driven model, we set up one simulation for each rainfall scenario, starting from a gradient of 0 m/yr to 10 m/yr (increasing from East to West in the simulation domain), for a total of 11 simulations. The precipitation runs explore how different rainfall amounts affect river incision mechanisms and whether larger gradients generate a stronger signal in the landscape.

Both the erodibility coefficient and the uplift rate are kept constant across all simulations at 3×10^{-8} and uplift rate is 1×10^{-5} respectively, yielding landscape reliefs within the ranges of those found on Earth. Similarly, n is chosen as 1 and m as 0.45 to keep the m/n ratio equal to 0.45, which is the central tendency of the concavity index across a large number of global landscapes (Kirby & Whipple, 2012; Gailleton et al., 2021; Tucker & Whipple, 2002). Although n is thought to take values other than unity in most landscapes (Lague, 2014; Harel et al., 2016), the value of this parameter is only man-

203 ifested in topographic outcomes during landscape transience (Whipple & Tucker, 1999;
 204 L. Royden & Perron, 2013) and does not affect our simulations since the landscapes are
 205 brought to steady state. When studying the channel steepness index across multiple basins,
 206 we set a reference value, θ_{ref} , (Gailleton et al., 2021) of 0.45 to establish a comparison
 207 between basins.

208 **2.1.2 Heterogeneous Lithologies**

209 To study the role of lithology in the prevalence of rainfall patterns we run a set of
 210 simulations with spatially varying values of erodibility, K . These simulations are designed
 211 to be closer to natural landscapes where the lithological landscape is more complex.

212 Within this study, we choose two lithological units reflecting the properties of a harder
 213 and a softer rock, with erodibility values ranging between $1e-7 < K < 5e-8$. This is
 214 in line with (Forte et al., 2016; Bernard et al., 2021; Peifer et al., 2021). Peifer et al. (2021),
 215 which determined that hard rocks can be related by a factor from 2-10 in erodibility to
 216 softer rocks (Forte et al., 2016; Bernard et al., 2021).

217 We simulate three heterogeneous lithologies scenarios: striped (a), sparse blob (b)
 218 and dense blob (c) lithologies (see SI, Figure S1).

- 219 1. **Striped lithology:** band of hard rock ($K = 5e - 8$) in the center of our sim-
 220 ulated mountain range, surrounded by soft rock ($K = 1e - 7$) to emulate cases
 221 like the Pyrénées.
- 222 2. **Sparse blob lithology:** 4 large hard rock ($K = 5e-8$) blobs evenly distributed
 223 on the landscape domain.
- 224 3. **Dense blob lithology:** many small hard rock blobs ($K = 5e-8$) of a few square
 225 meters in diameter, generated using Perlin noise (Perlin, 1985).

226 **2.1.3 Natural Landscapes**

227 We have chosen natural landscapes for this analysis on the basis of precipitation
 228 gradients and lithological structure, avoiding areas that have complex layers of soft rocks
 229 (Table 1). We analyze basins with a minimum drainage area of $1e7m^2$. We incorporate
 230 all channel pixels within tributaries that have a source area greater than $1.35km^2$ (which
 231 corresponds to 1500 pixels in topographic data with 30 m grid spacing).

Table 1. Geographical areas chosen along with the number of selected basins in each regions, area and rainfall range across the basin, from the outlet to the headwaters of the catchment. We choose a varied range of area sizes and precipitation gradients with to study prevalent trends across regions. Data extracted from the 30m Copernicus DEM and NASA’s Global Precipitation Measurement Mission (GPM) (Skofronick-Jackson et al., 2017).

Location	N basins	Area (km^2)	Precipitation Range (m/yr)
Andes, Southern Perú	5	29979	0.687-3.983
Andes, Northern Argentina	7	5932	0.045-0.010
North Qinling Mts, China	14	30832	0.734-0.938
Kaçkar Mts, Turkey	8	4279	0.784-1.673
Colorado Front Range, USA	7	9282	3.726-4.220
Alburz Mts, Iran	7	8167	0.357-0.849
Massif Central, France	5	1945	0.977-1.092
Pyrénées, Spain-France	5	6632	0.097-0.117

232 **2.1.4 Varying the simulation concavity index, θ (i.e. m/n ratio)**

233 We assess the impact of running the homogeneous lithology simulation with a fur-
 234 ther two choices of m/n : 0.35 and 0.55. The rationale for these experiments is to deter-
 235 mine if changes to the imposed m/n ratio causes distortions to k_{sn} of the same magni-
 236 tude as those induced by changing the incision rule. The broad effect on the landscapes
 237 with different values of m/n compared to the base case of $m/n = 0.45$ is that at 0.35 the
 238 landscape is smoother with lower relief and higher drainage density with sinuous trib-
 239 utaries, whereas at $m/n = 0.55$ the landscape has sharper features, with higher relief and
 240 lower drainage density, forming straighter tributaries. For detailed results of these sim-
 241 ulations, see SI (Text S6, Figures S16-S19, Tables S8-9).

242 **2.2 Metrics to quantify topographic outcomes**

243 Our models simulate river incision, and so we use river profiles to explore topographic
 244 outcomes of simulations. Because gradients should scale by either A or Q (depending
 245 on the incision rule) we use a coordinate transformation, first proposed by (L. H. Roy-
 246 den et al., 2000), that integrates either A or Q along the river profile:

247
$$\chi_A = \int_{x_0}^x \left(\frac{A_0}{A(x)} \right)^\theta dx \quad (5)$$

248
$$\chi_Q = \int_{x_0}^x \left(\frac{Q_0}{Q(x)} \right)^\theta dx \quad (6)$$

249 This transformation has various useful features. The gradient in χ_A -elevation space is
 250 equivalent to k_s if $A_0 = 1 \text{ m}^2$ (e.g., Perron & Royden, 2013; L. Royden & Perron, 2013;
 251 Mudd et al., 2014), and the gradient in χ_Q -elevation space is equivalent a metric k_{s-q}
 252 where gradient is scaled by Q instead of A in the form:

253
$$S = k_{s-q} Q^{-\theta} \quad (7)$$

254 when $Q_0 = \text{unity}$ in the units of Q used to calculate both χ_q and k_{s-q} (e.g., Adams et
 255 al., 2020; Leonard et al., 2023; Leonard & Whipple, 2021; D’Arcy & Whittaker, 2014;
 256 Harries et al., 2021). These steepness metrics can be used both in steady state and tran-
 257 sient landscapes (L. Royden & Perron, 2013). Another advantage of using the χ trans-
 258 formation is that tributaries to the main channel at the same elevation yield the same
 259 χ value, regardless of their drainage area. Given a landscape in steady state, the main
 260 channel and its tributaries should follow the same linear relationship on a χ - z plot, as-
 261 suming the same erosion and uplift rates (Perron & Royden, 2013) and the optimal con-
 262 cavity index value.

263 We exploit this latter feature in our efforts to discriminate, topographically, between
 264 incision rules. Regardless of the incision rule, selection of the incorrect value of θ will re-
 265 sult in tributaries that are not collinear, introducing distortions in channel steepness in-
 266 dex (Perron & Royden, 2013; Mudd et al., 2018; Hergarten & Robl, 2022; Gailleton et
 267 al., 2021; Goren et al., 2014; Harries et al., 2021). Computing χ_A or χ_Q also affects the
 268 channel steepness index values and the spread of the data, which can lead to different
 269 patterns of the channel steepness index and spreading the data in χ space (Figure 1).
 270 Because k_{sn} values are used to infer relative erosion rates across tectonically active re-
 271 gions, distortions to the spatial patterns of the channel steepness index can cloud inter-
 272 pretations of topographic pattern (e.g., Gailleton et al., 2021).

273 We quantify the spread of the χ - z profiles using a disorder metric, first proposed
 274 by Goren et al. (2014) and further developed by Hergarten et al. (2016) and Mudd et

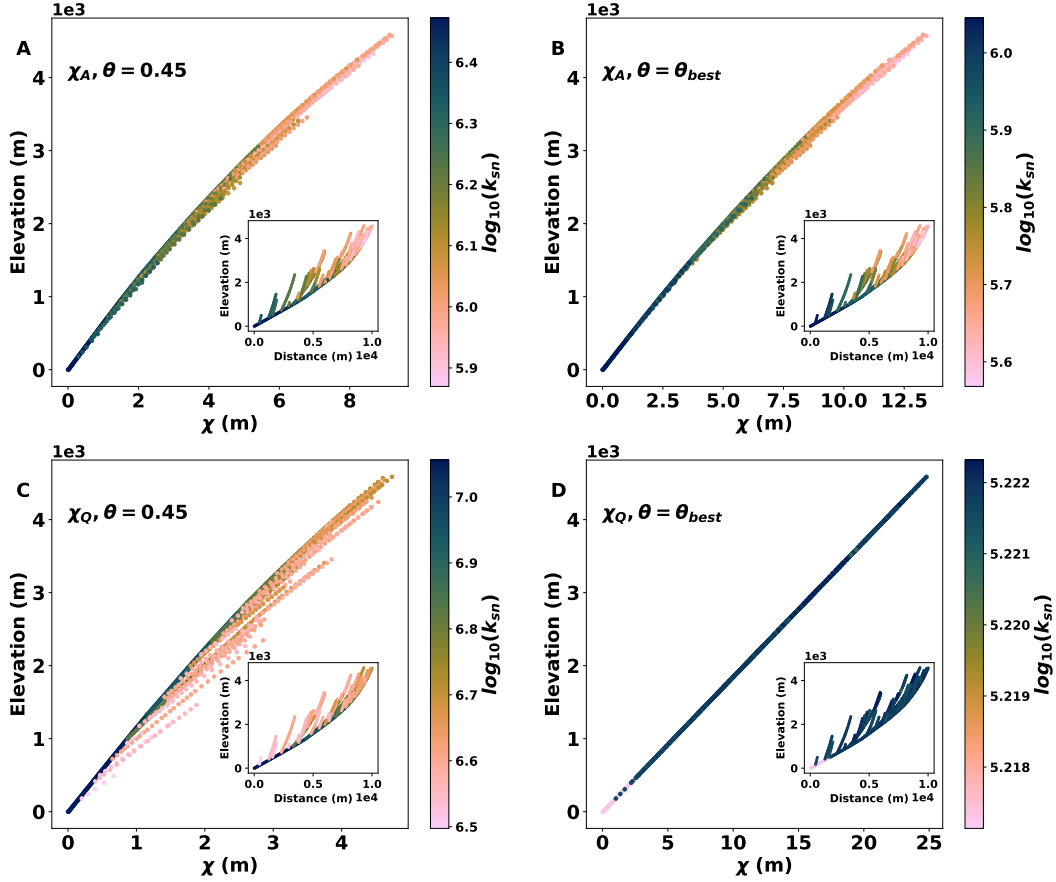


Figure 1. Illustration of how χ profiles and k_{sn} change based on the choice of incision scenario and concavity index values. The χ profiles result from simulations with a range of precipitation of 10m/yr (increasing west to east) under initial $m/n=0.35$. The basin shown is located on the wetter side of the domain, draining to the east. (D) shows perfect collinearity under χ_q and θ_{best} , which match the simulation parameters. (A) shows distortions using both the incorrect incision rule and the wrong θ , (B) shows a slightly more collinear profile, in this case only having the incorrect incision. (C) captures the correct incision (discharge) but uses $\theta=0.45$, where we see the largest increase in disorder and changes in k_{sn} .

275 al. (2018). One begins by ranking every point in the channel network by increasing el-
 276 levation, and then checks to see if the associated χ coordinates are similarly ranked (or
 277 not):

$$278 \quad R = \sum_{i=1}^N |\chi_{s,i+1} - \chi_{s,i}|, \quad (8)$$

279 where the the subscript s, i represents the i^{th} χ coordinate that has been sorted by its
 280 elevation ($\chi_{s,i}$). This sum, R , is minimal if elevation and χ are related monotonically.
 281 However it scales with the absolute values of χ , which are sensitive to the concavity in-
 282 dex (see equations 5 and 6), so following Hergarten et al. (2016) we scale the disorder
 283 metric, D , by the maximum value of χ in the tributary network (χ_{max}):

$$D(\theta) = \frac{1}{\chi_{max}(\theta)} \left(\sum_{i=1}^N |\chi_{s,i+1}(\theta) - \chi_{s,i}(\theta)| - \chi_{max}(\theta) \right). \quad (9)$$

We use the method of Mudd et al. (2018) to constrain uncertainty of this metric by creating subset networks formed from the trunk stream and every possible combination of three tributaries in a particular basin. This creates a population of D values for a given basin from which a median and interquartile range may be reported.

We normalize the disorder values across all tributary combinations, obtaining:

$$D^*(\theta) = \frac{D(\theta)}{D_{max}(\theta)} \quad (10)$$

where D_θ is the disorder for each tributary combination and $D_{max}(\theta)$ is the maximum disorder over all combinations.

In our analysis we aim to decipher whether we can identify the signal from a landscape shaped by rainfall *a posteriori*. To quantify this, we focus on the effect of rainfall in the $\chi - z$ profiles and in the disorder metrics. To emulate what the analysis would look like if we did not know the incision rule, we calculate the χ profiles in two ways for each simulation scenario - regardless of what the actual imposed incision rule is for a given numerical experiment. We calculate these metrics for each basin in the simulation draining to the edge and reaching the main drainage divide (Figure 2). For each of the basins simulated in each model scenario, we calculate the following:

1. χ_A : assumes a drainage area-driven incision (equation 5).
2. χ_Q : assumes a discharge-driven incision (equation 6).

For each of the χ cases, we calculate the disorder metric (equation 9). The disorder constrains the value for the optimal concavity index, θ_{best} , that will lead to the most collinear river profile configuration (Mudd et al., 2018; Gailleton et al., 2021).

2.3 Statistical Analysis

For each incision scenario, we calculate minimum normalized disorder values ($D^*(\theta)$) corresponding to each of the basins under each of the incision and χ scenarios. To measure if $D^*(\theta)$ for the basins in the simulations where incision is purely a function of A is statistically distinguishable from the basins where incision is driven by Q , we extract the value for $D^*(\theta)$ for each basin and χ case. We then calculate the absolute error between $D^*(\theta)$ in the two χ cases. The true value corresponds to calculating $D^*(\theta)$ with the χ of the matching incision scenario. The distribution of error values (ΔD^*) for all basins for each incision case can then be expressed as:

$$\Delta D^* = D_{rain}^* - D_{norain}^* \quad (11)$$

Since we are dealing with non-parametric distributions, we take the median of ΔD^* to quantify whether the A -based incision models may be distinguished from the Q -based incision models. We represent the distributions with kernel density estimates (KDE) (Cox, 2007; Silverman, 1998). If a percentage smaller than 5% is shared between the two distributions we consider them to be distinguishable from each other with 95% confidence.

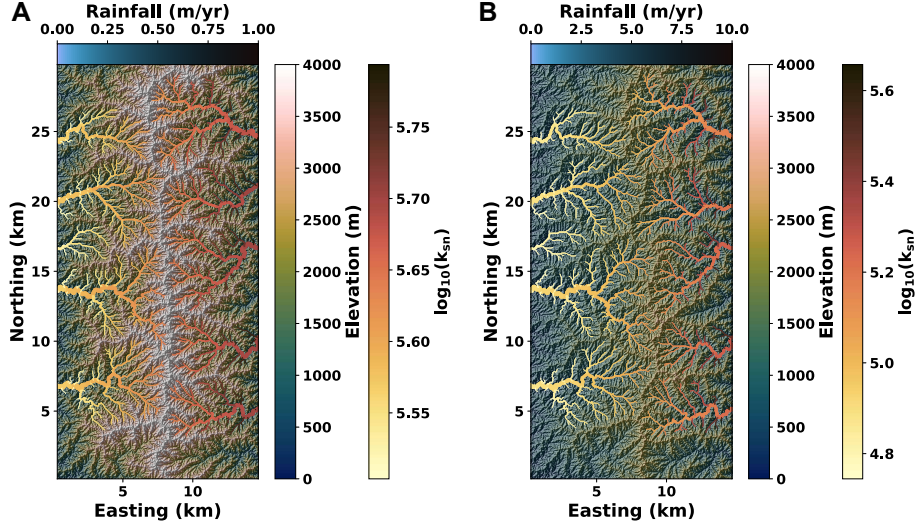


Figure 2. River networks generated with the numerical model under two discharge-driven incision scenarios, with rainfall ranges between (A) 0-1m/yr and (B) 0-10m/yr in the East-West direction. The smaller rainfall ranges in (A) lead to higher relief, steeper channels and a symmetric drainage divide. The higher rainfall in (B) leads to lower relief and a more sinuous and asymmetric drainage divide.

321

2.4 Measuring the effects of rainfall and θ on k_{sn}

322

323

324

325

326

327

328

329

330

331

In our numerical landscapes, we impose an erosion rule and then quantify the extent to which profiles are disordered when applying the appropriate or incorrect χ transformation (that is, using either A or Q). In real landscapes, however, we can only infer which of the two χ transformations is correct based upon relative disorder, and indeed neither may be correct. We resort to distortion in the χ -elevation profiles to quantify the impact of the choice of A or Q to scale χ when the correct choice is unclear. Specifically the distortion metrics quantify the degree to which k_{sn} changes if different choices in calculating χ are made. Determining the distortion of k_{sn} due to the choice of A or Q in calculating k_{sn} is important because it can affect the interpretations of the tectonic and erosional history of a landscape (Kirby & Whipple, 2012).

332

333

334

335

336

We quantify distortion by calculating the ratio between median upstream and downstream k_{sn} values and then investigating how this ratio varies depending on concavity index (Case *i*), incision scenario (Case *ii*) or both (Case *iii*), following the methods in (Gailleton et al., 2021). A full derivation of equations used to calculate the distortion is included in the SI, Text S1.

337

3 Results

338

339

340

In this section we present the numerical experiments and explore the effects of rainfall gradient on channel steepness and concavity index. We cover both homogeneous and heterogeneous lithologies.

341

3.1 Homogeneous lithology

342

3.1.1 Drainage area or discharge-driven incision?

343

344

345

346

347

348

Figure 3 shows the distributions of ΔD^* in each experiment using KDE fitting for Q -driven incision rule (equation 3) and A -driven incision rule (equation 2). Each kernel estimate is obtained for the collection of basins in the simulated domain. We obtain the median (solid line), 95th and 5th (dashed lines) percentiles for each kernel, repeating this procedure for each of the rainfall gradients. We consider $\Delta D^* = 0$ as the point where calculating χ_Q or χ_A would have no effect on the minimum disorder.

349

350

351

352

353

354

355

356

357

358

359

Figure 3 shows the distribution of ΔD^* values. Basins where the χ and the incision scenario match have lower D^* values. This is represented by the A -driven distributions lying on the negative side of the x-axis, meaning that the disorder value calculated using χ_A is lower than the disorder calculated using χ_Q . That is, unsurprisingly, using the version of χ that corresponds with the imposed incision rule results in less disordered channel profiles. The opposite is true of the Q -driven basins, which lie on the positive x-axis range, where the disorder is lower when calculating χ_Q than χ_A . This is true of all three indicated metrics: median, 95th and 5th percentiles. None of the distribution tails overlap inside of the 5-95th percentile ranges. For every rainfall distribution illustrated, the drainage area and the discharge driven incision are statistically far enough apart to be considered distinct distributions.

360

361

362

363

364

As rainfall gradients increase, the medians of the distributions diverge. For smaller rainfall gradients, the distribution medians appear closer together but still outside the 95% of each other that we consider an indication they are statistically distinct. The most significant differences arise from the discharge-driven scenarios, with the changes in the drainage area ΔD^* evolving slower with increased rainfall.

365

366

367

368

369

For every rainfall distribution illustrated under homogeneous lithology, calculating χ_Q or χ_A leads to statistically distinct ΔD^* distributions for the A and the Q -driven scenarios. Disorder can thus be used as a tool to recognize the dominating incision rule in numerical simulations: when $\Delta D^* < 0$, the incision is drainage area-driven, whereas $\Delta D^* > 0$ implies that discharge is the main incision mechanism.

370

3.1.2 k_{sn} distortion

371

372

373

374

We quantify k_{sn} distortion based on the cases outlined in section 2.4. We remind the reader of the three distortion cases we consider in this study *i*) change in θ , *ii*) change in incision rule, and *iii*) change in both. Similar patterns in changes in k_{sn} can arise from either of the three cases.

375

376

377

378

379

Figure 4 illustrates each of the distortion cases along a series of rainfall gradients for the discharge simulations. Panels A and B correspond to changes in θ (Case i). Panel C represents a change in incision rule (Case ii) and Panel D reflects a combined change in incision rule and θ values (Case iii). In all plots we indicate the no-distortion scenario at $y = 0$ with a solid black line.

380

381

382

383

384

385

386

387

388

389

Figure 4A reflects data from k_{sn-q} calculations, which capture the rainfall range used for the discharge-driven simulations. The associated distortion remains close to 1, indicating that using $\theta = 0.45$ as opposed to θ_{best} has minimal effects in the basin-averaged k_{sn} values. This can be explained by referring to the model set up. In the discharge-driven model with $m/n = 0.45$, with no other external factors to disturb equilibrium, we obtain steady state channel profiles with $\theta_{best} = 0.45$. This value is obtained from disorder minimization including rainfall in the calculations. Figure 4B reflects the results of not including a rainfall range in the disorder minimization procedure when calculating θ_{best} . Starting with a null distortion for the 0 m/yr rainfall range, distortion gradually increases with rainfall ranges. The distortion values reach 23% where $\theta_{best} > 0.45$

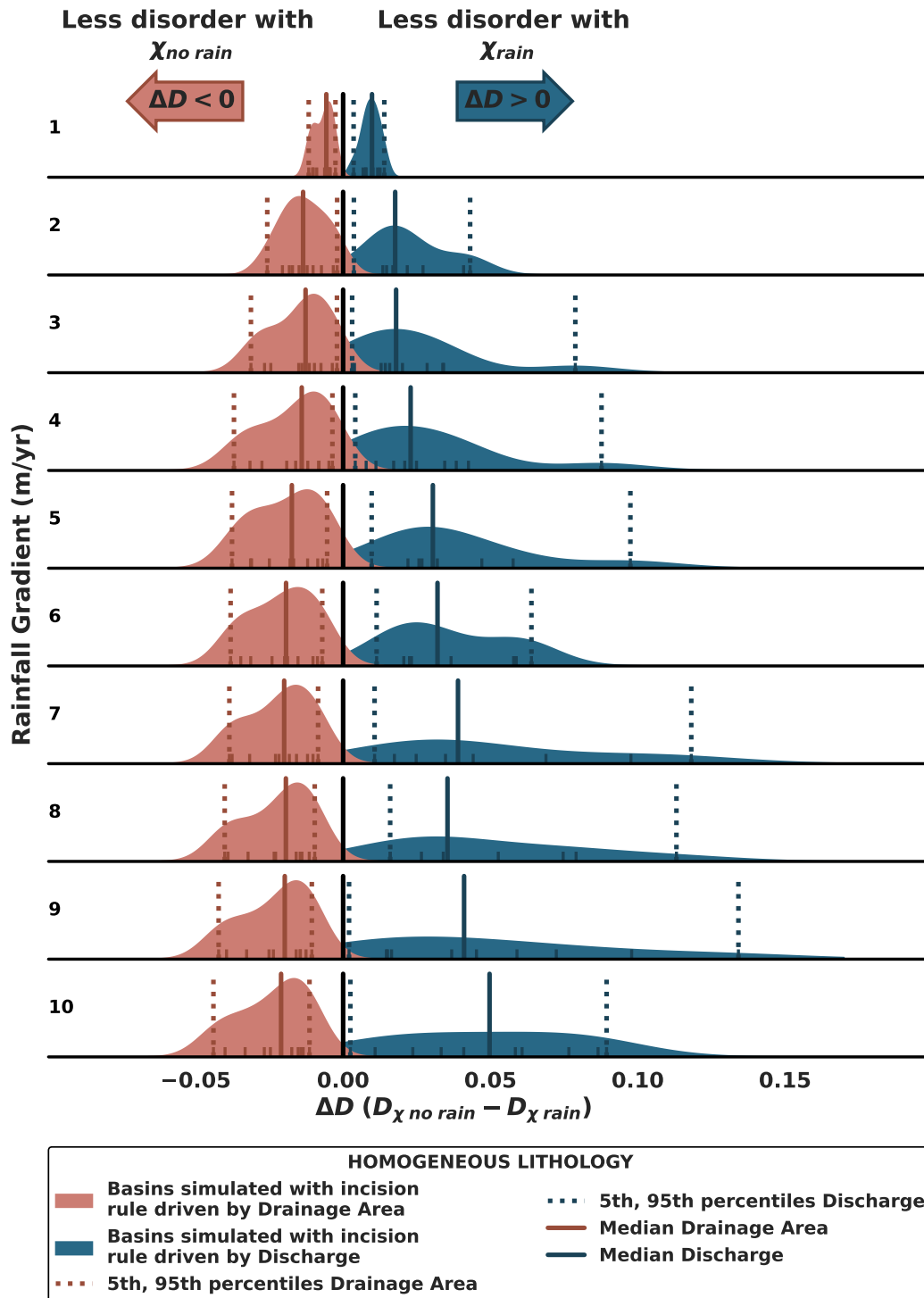


Figure 3. Comparison of the median values for ΔD^* for each of the rainfall gradients for A and Q -driven incision under homogeneous lithology for an initial $m/n=0.45$. The two models are always distinguishable: each of the distributions is on either side of the 0 line, with 95% confidence. The larger the rainfall gradient, the more separated the distribution medians become.

390 (above 1) and 15% when $\theta_{best} < 0.45$ (below 1). As the rainfall range increases, θ_{best}
 391 values diverge from 0.45. Figure 4C shows the distortion in case ii, which results from
 392 a difference in the assumed incision rule at a fixed concavity index ($\theta = 0.45$). The distortion
 393 pattern follows a similar path to Figure 4B: as rainfall ranges increase, so does
 394 the k_{sn} distortion. In this case, the values > 1 correspond to the windward (wetter) basins,
 395 where rainfall decreases as we move towards the mountain range. Distortion < 1 cor-
 396 responds to leeward (drier) basins where rainfall decreases as we move away from the
 397 mountain range. In both cases, distortion reaches 11%, with differences originating from
 398 the magnitude and the direction of the rainfall gradient. Figure 4D depicts distortion
 399 case iii: the effects of both a change in θ and a change in the incision rule. The percent-
 400 age of k_{sn} distortion is larger than in the other three scenarios: a 34% increase at the
 401 highest point against 23% and 11% in Figure 4B and C respectively. This arises from
 402 the basins having different θ_{best} depending on the incision rule used to calculate the k_{sn}
 403 distortion. The effect in the distortion is additive, meaning that compared to the cor-
 404 rect case for both incision and θ ($k_{sn-q}(\theta = \theta_{best})$), optimizing θ for the wrong inci-
 405 sion case would lead to the greatest distortion out of the three cases considered.

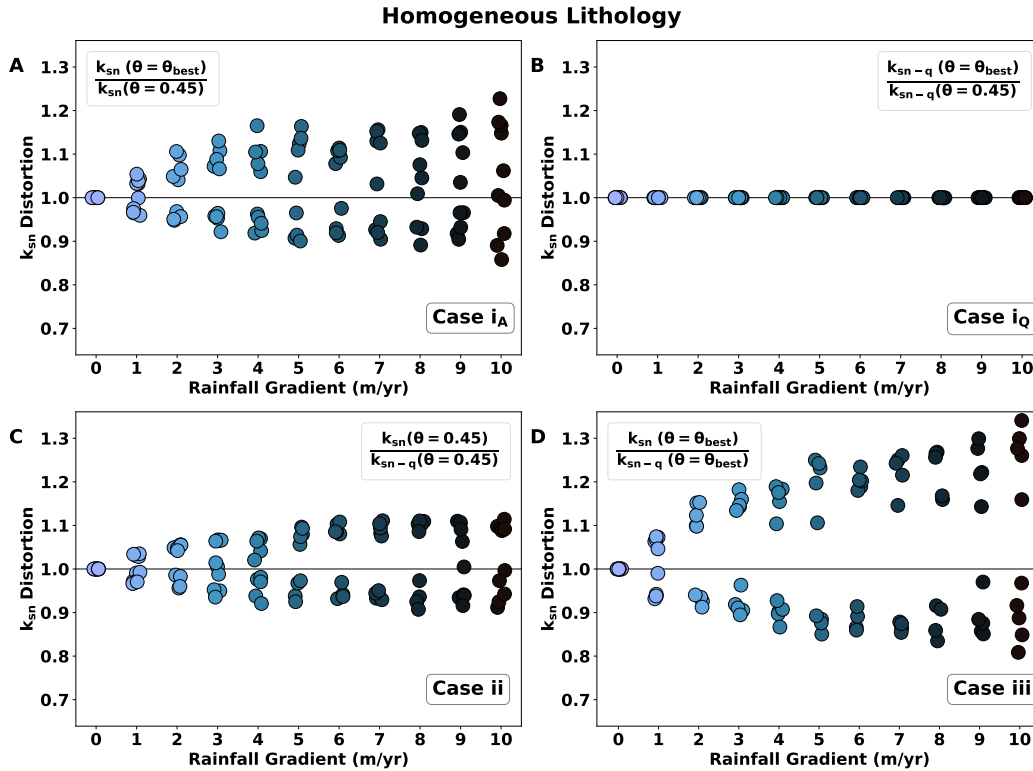


Figure 4. Distortion in k_{sn} for the Q -driven incision case under homogeneous lithology and initial $m/n=0.45$. A distortion of 1 (solid black line) keeps the value of k_{sn} unchanged. (B, Case i_Q) indicates that no k_{sn} distortion occurs when the concavity index and the incision case match the model scenario. (A), (C) and (D) show the possible distortion scenarios that one might encounter under different assumptions. (A) highlights the effects of optimizing concavity index under an incorrect incision scenario, (C) assumes concavity index is kept at 0.45 but the incision scenario changes and (D) comprises the effects of θ optimization under different assumptions of incision scenarios, where we see the largest k_{sn} distortions of up to 34%.

Distortion in the channel steepness index can be caused both by incorrectly assuming concavity indices and incorrectly assuming incision rules. That is, to calculate k_{sn} one must set a value of θ , and one must choose whether or not to incorporate a proxy for discharge, and either of these assumptions may not be the best reflection of reality in any given landscape. Optimizing θ will decrease the distortion in k_{sn} values, for cases when the incision mechanism is unknown. If we identify an incision mechanism, then distortion can also be decreased by using either k_{sn} or k_{sn-q} , depending on the case. However, we find that optimizing θ for an incorrect incision case leads to the highest distortion values.

3.2 Heterogeneous lithology

We have shown that it is possible to differentiate a signal from an A -driven incision scenario from a Q -driven scenario, under homogeneous lithology. However, many natural landscapes contain a range of lithologies with different erodibilities. We complement our analysis with data from simulations with heterogeneous lithologies, as described in Section 2.1.2. We illustrate the behavior from results from the most densely varying lithology (dense blob), with two extra cases (blob and striped lithology) included in the Supplementary Information.

In Figure 5 we see that in contrast with the homogeneous lithology case, we see that the disorder metrics derived from the A -driven and Q -driven basins are not statistically distinct. Both distribution medians are similar regardless of the rainfall range and they fall within each other's 95% percentile of the population. The more heterogeneous the erodibility, the harder it becomes to distinguish between the original incision rules. The dense blob lithology simulations feature channel metrics where it is most difficult to differentiate A -driven from Q -driven incision rules using, with other lithologic types having larger differences in median disorder (see Supplementary Information).

We also quantify how heterogeneous lithologies impact the distortion of k_{sn} values. We start by looking at the result of adding lithology to the discharge-driven model scenario and compare the results to Figure 4. We highlight that in the heterogeneous lithology cases, we do not expect θ to be 0.45 at a rainfall range of 0m/yr. We have introduced a perturbation, leading the system to diverge from $\theta = 0.45$ that we obtained in an unperturbed, steady state scenario. This is reflected in a distortion between 10% - 20% at rainfall ranges of 0 m/yr in all distortion cases. Irrespective of the range in rainfall, this distortion remains within the same bounds. We see consistently higher distortion values for all rainfall ranges in 6B, as a result of using the incorrect incision scenario when optimizing θ . In Figure 6C we see the distortion associated with Case ii (caused by changes in incision rule), when keeping $\theta = 0.45$. As the rainfall range increases, the distortion shifts towards being larger, up to 44% in leeward basins. When we optimize θ and compare between the two incision scenarios 6D, the distortion in both the windward and the leeward side is increasing at a similar rate with increasing rainfall ranges. This is the only distortion case where we see a systematic increase in distortion with rainfall ranges.

Heterogeneities in lithology add to the distortions in channel steepness index caused by rainfall ranges. The signal from the rainfall is reflected as a systematic increase in distortion in A -driven cases. In Q -driven scenarios the systematic increase of distortion with rainfall range is masked by the lithological heterogeneities when comparing between θ values. Optimizing θ will remove the distortion that we incorporate by using $\theta = 0.45$, which is more prominent in heterogeneous than homogeneous lithologies. Making a decision on the type of incision, will also reduce the distortion. However, this can end up with an increased distortion if the incision type assumed for calculating χ is incorrect and θ is subsequently optimized using channel information obtained from that incorrect incision type.

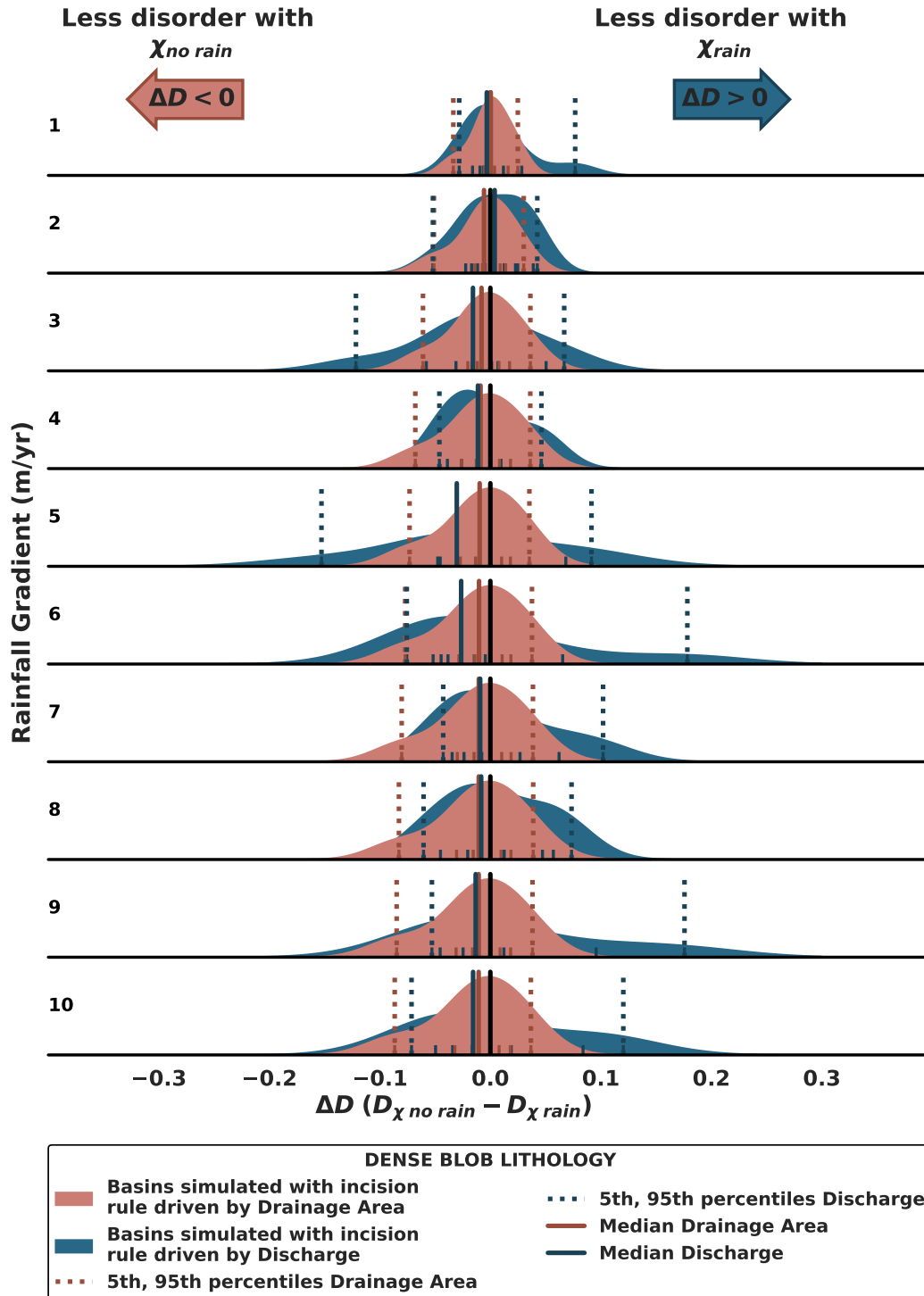


Figure 5. Comparison of the median values for ΔD^* for each of the rainfall ranges for A and Q -driven incision under dense blob lithology for an initial $m/n=0.45$. The distribution medians and percentiles largely overlap, meaning that the models are not distinguishable, regardless of the rainfall gradient.

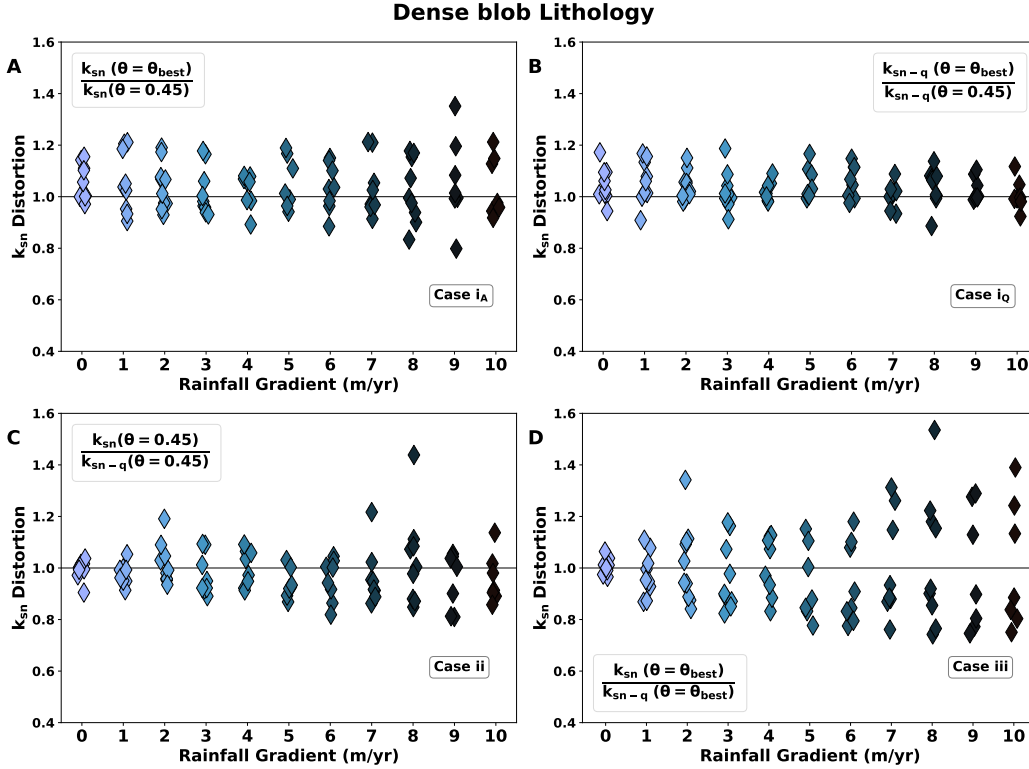


Figure 6. Distortion in k_{sn} for the Q -driven incision case under heterogeneous lithology and initial $m/n=0.45$. A distortion of 1 (solid black line) keeps the value of k_{sn} unchanged. We show the possible distortion scenarios that one might encounter under different assumptions of concavity index and incision. (A) highlights the effects of optimizing concavity under the incorrect incision scenario (drainage area), whereas (B) shows the distortion incurred by not optimizing θ under Q -driven incision. (C) keeps concavity index at 0.45 but compares incision scenario and (D) comprises the effects of θ optimization under different assumptions of incision scenarios, where we see the largest k_{sn} distortions of up to 54%.

457

3.3 Natural Landscape Study Cases

458

459

460

461

462

463

464

465

466

467

468

469

470

471

We have quantified how a changing range of rainfall can lead to differences in k_{sn} and θ_{best} under various incision scenarios in simulated landscapes. Our numerical experiments suggest that it is possible to statistically distinguish A -driven and Q -driven incision landscapes in a lithologically homogeneous model using disorder metrics. Heterogeneous lithologies capture how the rainfall signal is obscured by additional forcings, namely spatial variation in erodibility, a common feature in natural landscapes. Having isolated these signals in experiments, we now apply this knowledge to real landscapes, where we only have *a posteriori* topographic states from which to infer the landscape incision rule. We remind readers, when interpreting our results, that $D^*(\theta_{best,Q}) < D^*(\theta_{best,A})$ suggests that the basin has been shaped by rainfall as a main incision mechanism. On the other hand, $D^*(\theta_{best,Q}) > D^*(\theta_{best,A})$ suggests that basin incision is driven by drainage area. Our numerical experiments suggest that $\Delta D^* < 0$ in landscapes with A -driven incision. In Q -driven, $\Delta D^* > 0$. We calculate ΔD^* for natural landscapes in the same fashion.

472 For each basin, we repeat the calculations outlined in section 2.2, and plot the me-
 473 dian values of normalized distortion (ΔD^*) and their distributions in Figure 7. As a re-
 474 minder, this metric quantifies which of the two assumed incision scenarios results in lower
 475 distortion of the channel network. If all basins are positive, or all are negative, we view
 476 this as an indication that one of the two assumed incision signals better describes the
 477 observed topographic data. We see in Figure 7, most natural landscapes have basins that
 478 straddle $\Delta D^* = 0$, meaning that we cannot determine the most likely incision scenario
 479 with any confidence. Only in the cases of the Colorado Front Range and the Massif Cen-
 480 tral do we see a statistically significant imprint on ΔD^* . Those basins lie on the pos-
 481 itive side of the x-axis, favoring discharge as the predominant incision mechanism. The
 482 other sites show smaller confidence intervals in ΔD^* values, and their basins only a slight
 483 trend towards an incision scenario (drainage area -Pyrénées, Alburz, Qinling- and dis-
 484 charge -Perú, Argentina, Kaçkar-). The distributions center largely around the $\Delta D^* =$
 485 0 with spreads at either side of the incision case division.

486 If we are not able to distinguish the correct incision scenario using the disorder met-
 487 rics, how uncertain will our interpretations of channel steepness become? In Figure 8 we
 488 investigate distortions in the channel steepness index. We highlight the difference in scale
 489 of the results shown here. In the modeling experiments, some scenarios show a distor-
 490 tion of no more than 10% under low rainfall (eg. Figures 4A, S12B, S3 (A-C)). In real
 491 landscapes, we observe larger distortion values for all cases, in some instances reaching
 492 36% in 8D, 50% in 8B and above 75% distortion in 8A and C. In natural basins, using
 493 $\theta = 0.45$ becomes a large source of distortion to the channel steepness index, regard-
 494 less of the assumed incision scenario. This is a consequence of the θ_{best} values diverg-
 495 ing from 0.45, which corresponds to the m/n value of the models. Compared to these
 496 large distortion values incurred by using $\theta = 0.45$, the distortion values arising from
 497 choosing A -driven or Q -driven incision scenarios fall considerably. We see most distor-
 498 tion falls within the 25% bounds, regardless of the mountain range, although with dif-
 499 ferent amounts of spread around the null distortion line at $y = 1$. This shows that in
 500 natural landscapes, optimizing the concavity index is more important than choosing the
 501 correct incision scenario. As opposed to the model, in natural topography we do not see
 502 an increase in the distortion originated from case *iii* compared to the other two cases.

503 We plot the distributions of k_{sn} and k_{sn-q} for θ_{best} and $\theta = 0.45$. Under $\theta = 0.45$
 504 (9B), the differences in channel steepness index are larger, for instance in Argentina or
 505 Colorado, where the peak of the distribution is shifted and the distributions changing shape.
 506 However, cases such as the Pyrénées or the Massif Central show little differences in the
 507 distributions. 9A shows the channel steepness index distributions for θ_{best} . We see that
 508 the shape of the curves is better preserved, with less variation in the location of the peak
 509 between the A and the Q cases.

510 4 Discussion

511 4.1 Channel steepness index and Erosion Rates

512 Our numerical experiments show that in lithologically homogeneous landscapes it
 513 is possible to distinguish between drainage area and discharge-driven landscapes from
 514 topographic metrics alone. If the imposed incision law is discharge-driven, but channel
 515 steepness is calculated assuming an area-driven incision driver (that is, χ is calculated
 516 only taking A into account), the distortions to the channel steepness index can be as high
 517 as 34% within our simulations, with varying patterns depending on the lithology and the
 518 type of rainfall. Homogeneous lithology leads to k_{sn} distortion that increases monoton-
 519 ically with increasing rainfall ranges (Figure 4A, C, D), whereas heterogeneous litholo-
 520 gies totally overprint rainfall-related signals (see Figure 6A, B, C). Adding heterogeneous
 521 lithologies in the model simulations also induces a systematic increase in the disorder
 522 metric. This makes it harder to identify a pattern whereby a worker can clearly extract

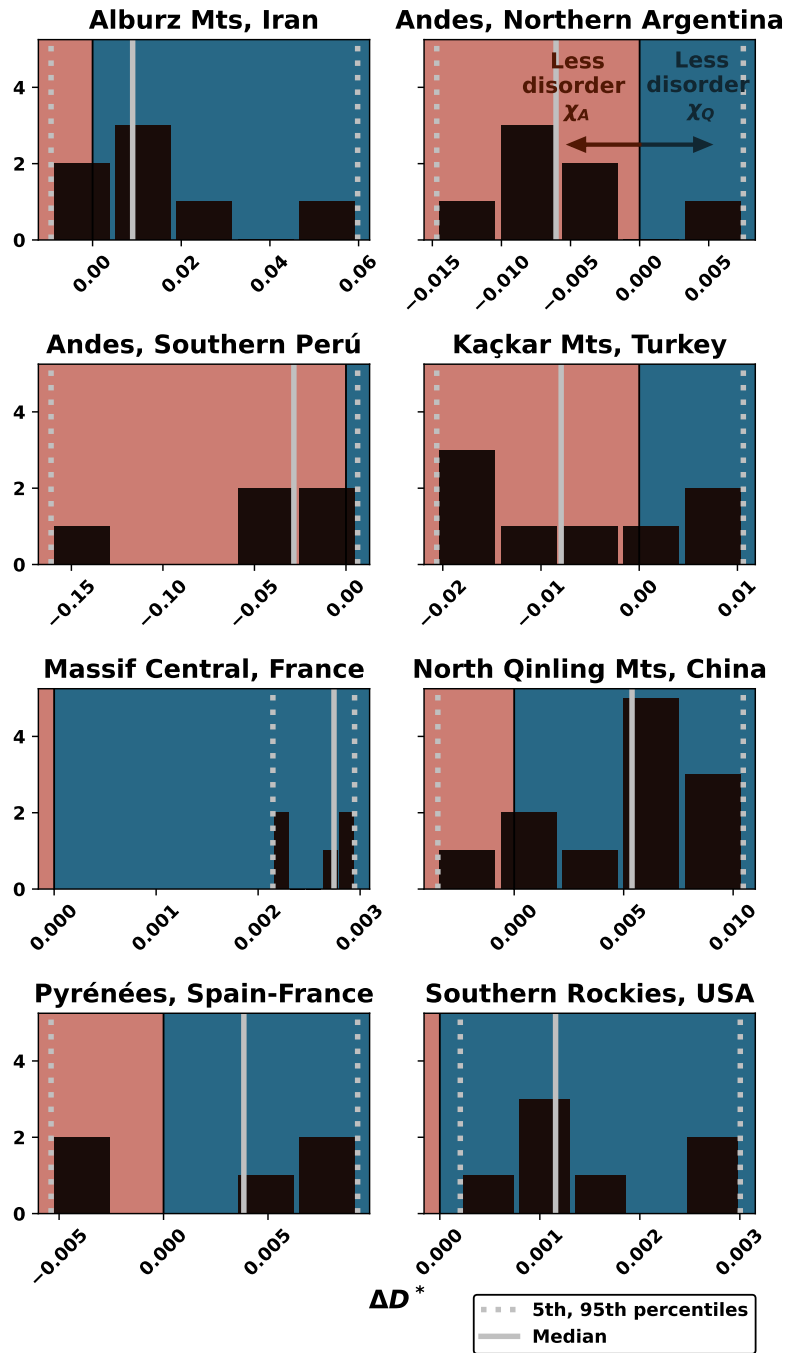


Figure 7. Comparison of the median values for ΔD^* for each of the mountain ranges. Results that lie above the $y=0$ line correspond to cases driven by rainfall. Points that lie below the $y=0$ line are cases where other forcings aside from rainfall (such as tectonics or lithology) are dominating over the rainfall signal. Some cases show a slight preference towards χ_A (Perú, Argentina, Turkey) whereas the rest prefer χ_Q . However, the confidence interval for this is lower than 95%, meaning that the results are largely basin dependent. Topographic analysis is not sufficient to draw conclusions about the incision mechanisms and further field observations of erosion rates would be needed.

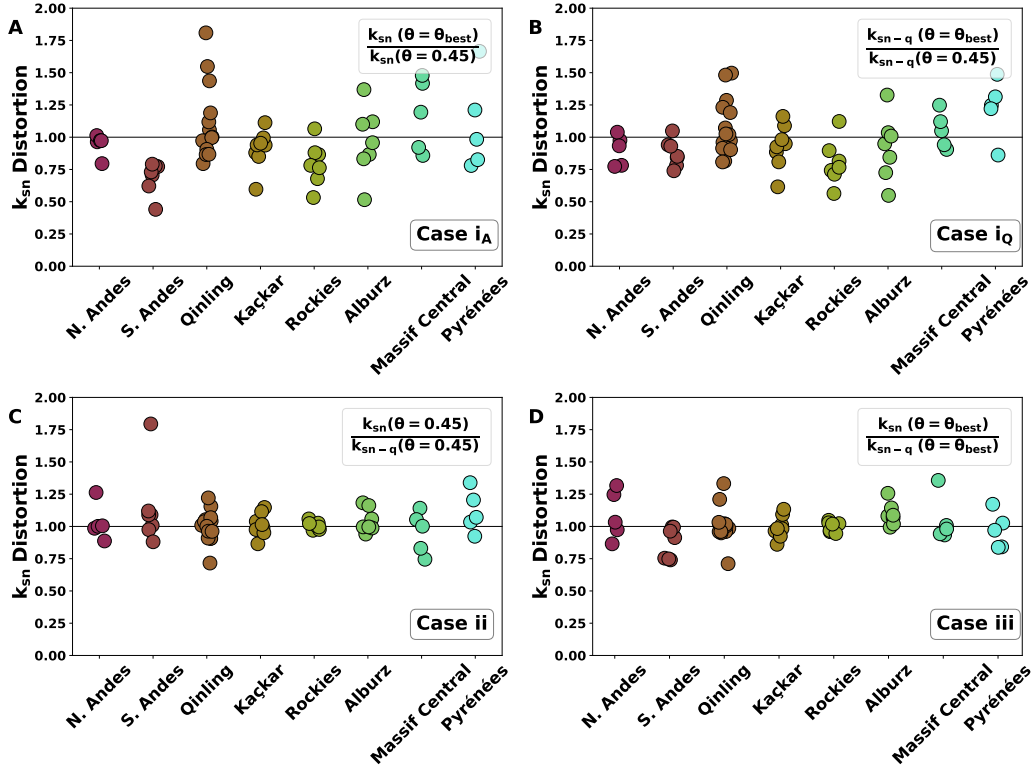


Figure 8. Distortion in k_{sn} for a range of natural landscapes. A distortion of 1 (solid black line) keeps the value of k_{sn} unchanged. The distortion scenarios are a representation of how one might introduce bias in k_{sn} under an unknown incision scenario, as is the case in many sites. Keeping $\theta=0.45$ under different incision scenarios can lead to distortions of up to 79% (C). We show as well the distortion introduced by choosing $\theta=0.45$ instead of θ_{best} , reaching 81% under A -driven incision (A) and 50% under Q -driven incision (B). (D) depicts the distortion introduced by optimizing θ under both incision regimes, with values of up to 36%.

523 the range of rainfall across the mountain range. For instance, in the striped lithology case
 524 (Figure S2, SI) all basins are affected by both the two erodibilities and the rainfall ranges,
 525 but at different parts of the catchment, because some tributaries will only have one rock
 526 type.

527 Distortions in channel steepness index are not solely caused by external forcings,
 528 such as rainfall or erodibility. In simulations depicted in Figure 4 we have imposed a discharge-
 529 driven incision rule, with a θ of 0.45. The largest distortions result from comparing the
 530 imposed incision law with the correct θ against the incorrect incision law with an opti-
 531 mized θ (Figure 4D). However, in a real landscape we will not know the “true” erosion
 532 law or the “true” value of θ , and we find that the distortions associated with changing
 533 the θ value between 0.45 (used in many studies) and an optimized θ is similar to the dis-
 534 tortions introduced by not accounting for rainfall (Figure 4A and C).

535 A change in distortion is a reflection of differences between tributaries and trunk
 536 behavior as a result of spatial changes in rainfall. For instance, tributaries represent a
 537 larger percentage of the channels in smaller basins, meaning that their signal becomes
 538 amplified in those cases (Leonard et al., 2023). We then expect different parts of the catch-
 539 ment and channels of different sizes to react differently to spatially heterogenous rain-

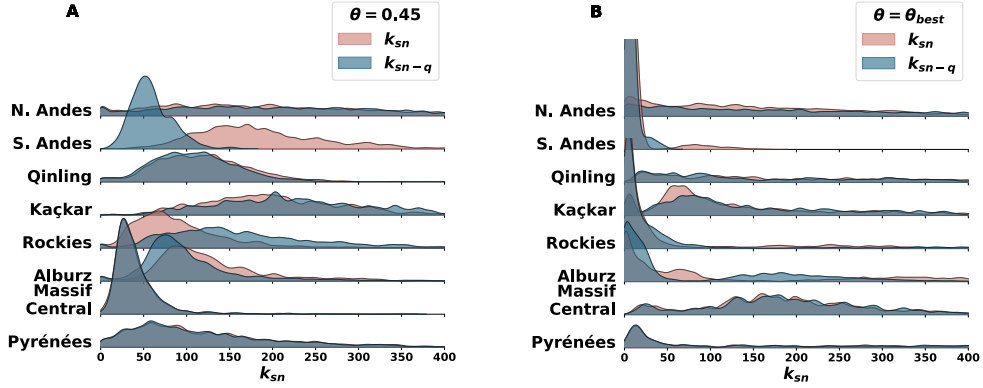


Figure 9. Distribution of k_{sn} and k_{sn-q} values for all the basins across each mountain range. Assuming $\theta=0.45$, we see large difference in k_{sn} values and distribution shape for the Southern Andes and the Rockies, other areas, such as the Massif Central or the Pyrénées do not experience significant changes. Under θ_{best} (B), the distribution largely changes from (A), shifting towards smaller channel steepness index. Mountain ranges like the Rockies now show a closer agreement between the k_{sn} and the k_{sn-q} distributions.

540 fall and lithology. According to the modeling work by Han et al. (2015), smaller chan-
 541 nels are more affected by rainfall, with large variability in k_{sn} reflecting the precipita-
 542 tion gradient. Recent work by Leonard et al. (2023) proposes that smaller catchments
 543 are more prone to biases because their contribution to the overall basin metrics is larger.
 544 In line with this, we have set bounds for basin drainage area size and minimum tribu-
 545 tary size. This will lead to more consistent k_{sn} values and avoid incorporating tributaries
 546 dominated by hillslope diffusivity processes. Our modeling results suggest that in Q -driven
 547 basins, given that the concavity index is optimized, the distortion will be minimal when
 548 using k_{sn-q} . This agrees with the study by Leonard et al. (2023), where in areas of
 549 the Andean Cordillera with strong rainfall gradients k_{sn-q} and $\theta_{ref} = 0.50$ yield a minimal
 550 distortion.

551 Natural topography, however, shows more complexity than our sandbox models,
 552 which leads to difficulties in identifying the different incision scenarios. We choose a small
 553 number of basins across a multitude of different areas (as opposed to (Leonard et al., 2023)),
 554 where the study is along a single geographical region) to identify topographic metrics
 555 than can differentiate between incision scenarios. This offers the worker an estimate of
 556 how much of a distortion they would introduce given the incorrect incision rule or con-
 557 cavities index. Leonard et al. (2023) also show that in the Andes, the differences between
 558 the trunk and tributaries are starker when using the incorrect incision mechanism than
 559 when comparing k_{sn} under different -incorrect- concavity index scenarios.

560 Determining the incision rule that is more consistent with observed topography will
 561 help in interpreting topography in areas with large changes in rainfall across the study
 562 area. The distortion that we have found in our study can then be translated into uncer-
 563 tainties in erosion rates. (Adams et al., 2020) found that the erosion rates from Be-10

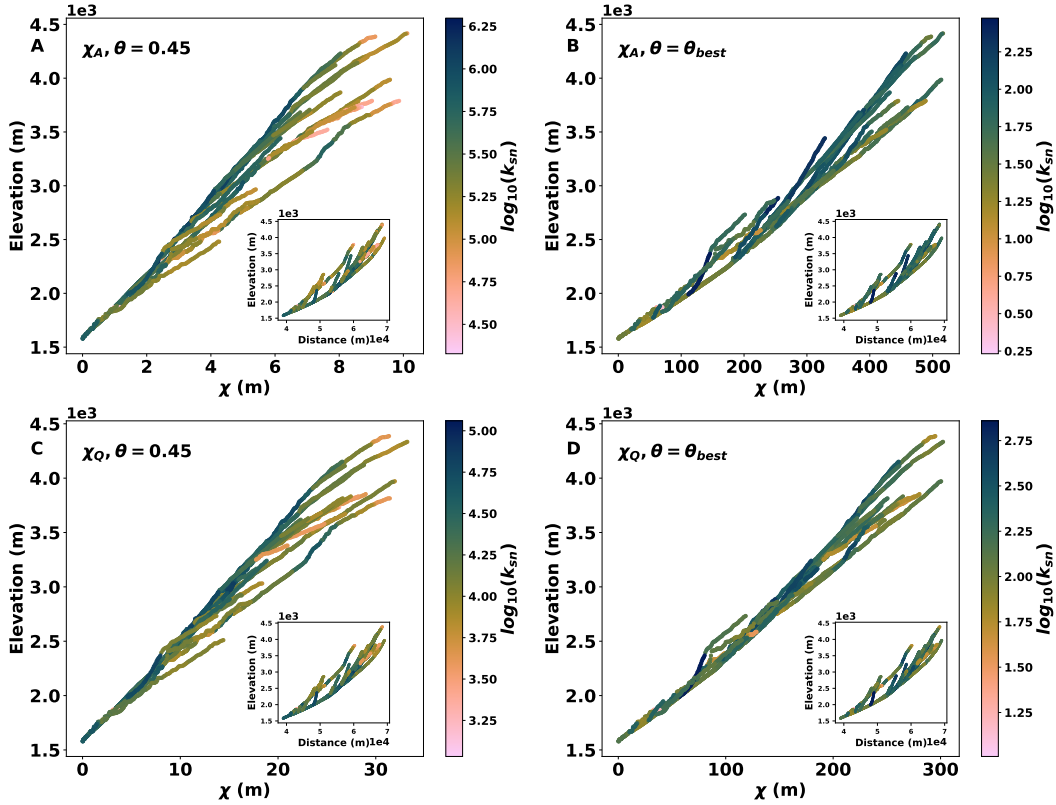


Figure 10. χ profiles for a basin in the Argentinian Andes, under different incision and concavity index scenarios. The disorder decreases when we optimize the concavity index (θ_{best}) ((B) and (D)). The channel steepness index is higher when $\theta=0.45$ ((A) and (C)). Compared to the effects that changes in concavity index have in the profiles, the choice of incision rule introduce secondary differences in the channels.

564 in the Himalayas and Bhutan are better constrained when using k_{sn-q} instead of k_{sn} (which
 565 (Leonard et al., 2023) corroborates), otherwise causing them to be artificially high. We
 566 find that changes in the concavity index can lead to changes in channel steepness index
 567 which are often larger than those caused by spatially varying rainfall, suggesting a po-
 568 tential cumulative effect of the different biases.

569 However, these changes in θ values are linked not only to different rainfall (Harries
 570 et al., 2021; Zaprowski et al., 2005) and lithological regimes (Duvall et al., 2004). The
 571 nature of the river bed (Howard & Kerby, 1983; Tucker & Whipple, 2002), the sediment
 572 availability (Wickert & Schildgen, 2019), and the tectonic setting (Kirby & Whipple, 2001)
 573 can also affect the value of θ in different reaches of the rivers in a way that would be-
 574 come hard to disentangle from spatial changes in rainfall. Han et al. (2015) explores changes
 575 that spatially varied rainfall can have on the concavity index through modeling exper-
 576 iments. In natural landscapes, changes around their chosen value of 0.5 vary compar-
 577 atively less due to rain gradients than changes caused by factors such as the type of chan-
 578 nel bed (Whipple & Tucker, 2002), sediment amounts (Gasparini et al., 2007) or uplift
 579 rate changes (Kirby & Whipple, 2001).

580 The distribution of k_{sn} and k_{sn-q} values for natural landscapes shows the variabil-
 581 ity in behavior between mountain ranges (Figure 9). For $\theta = \theta_{best}$, the variability be-
 582 tween k_{sn} and k_{sn-q} is smaller than for $\theta = 0.45$. This means that as long as the con-

583 cavity index has been constrained, the channel steepness index variations between A and
 584 Q -scenarios will be smaller than if $\theta = 0.45$ was chosen. We note that the mountain
 585 ranges where the distributions diverge for A and Q cases often correspond to the ones
 586 where the disorder is high, demonstrating once more that using unconstrained values of
 587 θ to extract geomorphometrics can amplify process-linked biases. For instance Ar-
 588 gentina shows consistently distortion between 25-75% in Figure 8, seeing some of the largest
 589 variability in channel steepness index for some of the basins. Plotting the χ -elevation plots
 590 for one of the basins with the strongest distortion Figure 10, we can see that the disorder
 591 of the tributaries with respect to the main stem is decreased the most when using
 592 χ_Q and $\theta = \theta_{best}$. Most of the changes in channel steepness index due to concavity in-
 593 dex optimization affect the upstream tributaries, we see as well how the profiles collapse
 594 more as a result of choosing θ_{best} than by including or removing rainfall in the calcula-
 595 tions.

596 4.2 Rainfall and climate

597 In this work, we have chosen to simplify the rainfall patterns in manner mirroring
 598 (Leonard & Whipple, 2021) by approximating the orographic behavior using a linear in-
 599 crease of rainfall with distance along the mountain range, emulating the effect that oro-
 600 graphic rainfall has on real landscapes. The rainfall asymmetry generates a displacement
 601 of the divide towards the drier side of the mountain, where the erosion is smaller. We
 602 observe different levels of channel steepness index distortion for the wet and the dry side
 603 of the simulated mountain ranges, and making it possible to identify the type of rain-
 604 fall gradient (top-heavy or bottom-heavy - following the nomenclature in (Leonard & Whip-
 605 ple, 2021)- from the value of the distortion ratio. This difference between the wet and
 606 the dry side of natural landscapes has been studied in depth in natural settings such as
 607 Hawai'i (Ferrier et al., 2013), albeit in tectonically complex regions outside our scope.

608 In the modeling framework, we have assumed that the rainfall pattern remains con-
 609 stant throughout time, but this is not necessarily the case in natural landscapes. Even
 610 small climate changes can lead to changes in the rainfall pattern and discharge amounts
 611 at different parts of the catchment, altering the local erosion rates and displacing the land-
 612 scape from an equilibrium state (Leonard & Whipple, 2021). The regions of study lie
 613 within the mid-latitudes, where the climate has remained largely unchanged (Roe et al.,
 614 2002). Changes in atmospheric circulation patterns or temperature changes (Herman et
 615 al., 2013; Bradley, 2015; Ward & Galewsky, 2014) are some examples of cases when other
 616 climate variable can affect erosion rates. Glaciations are also important when consider-
 617 ing a large portion of the Earth's landscapes, and they also show a relation with the ero-
 618 sion rates and the relief of the landscape. From our simulations, we have seen how the
 619 relief decreases as precipitation rates increase, as expected. In natural landscapes, the
 620 relationship between relief and rainfall is complex and influenced by local processes be-
 621 yond the scope of this project (Montgomery et al., 2001; Champagnac et al., 2012).

622 4.3 Disorder to indicate incision rate

623 Our hypothesis states that basins undergoing a strong rainfall gradient are distin-
 624 guishable based on their disorder values. This is true under homogeneous lithologies and
 625 in cases where the erodibility differences happen smoothly over the scale of multiple basins.
 626 In this case, it is possible to distinguish with 95% confidence between A -driven incision
 627 and Q -driven incision, regardless of the rainfall gradient. Adding sudden changes in lithol-
 628 ogy within basins and natural topographies makes identifying the correct incision rule
 629 challenging. The shape of the basins can have an effect on the disorder values. (Han et
 630 al., 2015) highlight how longer and narrower catchments experience a similar rainfall gra-
 631 dient between the tributaries and the trunk channel, whereas wider basins where the trib-
 632 utaries are more misaligned experience a higher disorder. In our experiments, we are look-
 633 ing at the overall behavior of the landscape, thus mixing basin shapes which would in-

trinsically have different disorders based on their shape, regardless of the forcing. Since in the disorder calculations we only compare each basin with itself under different incision scenarios, the intrinsic disorder differences between basins should not pose a bias.

4.4 Limitations

One of the limitations of our study lies in the precipitation treatment, both in the modeling study and in the natural landscapes. While it is possible to reproduce a realistic rainfall pattern using the Fastscape module adapted from (Smith & Barstad, 2004), it is computationally expensive and requires knowledge of the wind patterns of the region of interest, which change at different atmospheric layers. We assume that the orographic rainfall can be approximated in the modeling framework by a linear rainfall trend that does not change through the simulation, regardless of the relief (Roe et al., 2003). In real orographic rainfall scenarios, there would be a positive feedback between the rainfall and the topography, which our model does not capture.

In our natural sites, we also assume that the rainfall pattern, derived from the average rainfall from 20 years (2000-2020), is representative of the precipitation at that site throughout its history, in geologic timescales. Climate patterns have changed throughout the centuries driven by changes in atmospheric condition, solar irradiance, and biosphere and ocean changes (Bradley, 2015). The regions of study lie within the mid-latitudes, where the climate has remained largely unchanged (Roe et al., 2002). However, due to having taken into account data from the 21st century, recent changes in rainfall pattern due to human made climate change cannot be ruled out to have intervened in the data from the past years compared to data prior to industrial revolution.

The question of whether mean annual precipitation should be used to describe the climate of a region is also a highly debated topic, with studies suggesting that it is the storms and extreme events which contribute the most to mean annual precipitation and do the most erosive work (Sorensen & Yanites, 2019; DiBiase & Whipple, 2011; Deal et al., 2017, 2018; Rasmussen et al., 2016). Other studies prefer the use of mean annual precipitation (Leonard & Whipple, 2021; Adams et al., 2020; Rossi et al., 2016; Anders et al., 2006; D'Arcy & Whittaker, 2014; Gasparini & Whipple, 2014; Armitage et al., 2011), especially when capturing the erosion work longer climatic trend or incorporating it in long-term landscape evolution models.

In the modeling framework, many processes have been simplified. We have already mentioned the rainfall patterns, which is the main focus of this study. The representation of lithological units, the exclusion of sediment supply and the homogeneous uplift, have all been choices made to isolate the climatic signal as much as possible. We are also assuming that the detachment limited SPM forms a good basis for how rainfall interacts with uplift and erosion, which many studies support (e.g., Leonard et al., 2023; Leonard & Whipple, 2021; Adams et al., 2020; Gasparini & Whipple, 2014; Harries et al., 2021), while acknowledging it still does not fully explain all geomorphic processes at the landscape scale.

5 Conclusions

In this study, we explore whether it is possible to determine whether channel incision is most closely related to drainage area or discharge (or some proxy thereof) from topographic metrics alone. Many past papers quantify channel steepness calculated based on drainage area as an indicator of river incision rates (e.g., Kirby & Whipple, 2012; Harel et al., 2016), but now that precipitation records are more readily available (Skofronick-Jackson et al., 2017), we must question whether adding rainfall gradients to the equation will yield different topographic outcomes in river channels.

In a simple numerical model with homogeneous lithology, disorder metrics (Mudd et al., 2018; Gailleton et al., 2021; Goren et al., 2014) yield a clear distinction between A and Q -driven incision basins with a monotonic dependence on rainfall gradients. When the system is perturbed by adding areas with different erodibilities, the incision signal is obscured. However, including rainfall gradients is not the only way to distort a signal. We have quantified the effects that optimizing the concavity index θ can have in the channels, concluding that using the standard value of $\theta = 0.45$ amplifies the distortion caused by rainfall effects.

In natural landscapes, we cannot establish a general topographic rule to distinguish between A and Q -shaped basins. We find catchments that are better described by discharge and others by drainage area, in some cases with quite a stark contrast. Given that we are not able to separate those cases topographically, we quantify how much distortion we would introduce in channel steepness index if we failed to identify the incision mechanism. Our results suggest that in most basins we would see maximum changes in channel steepness index of up to 25%, which does not constitute enough to drastically change the interpretation of erosion rates across the landscape. We compare this to distortions in k_{sn} of 50% obtained from using $\theta = 0.45$ instead of optimizing the concavity index. We suggest readers to use θ_{best} as an efficient method to reduce distortions already introduced by an unknown incision mechanism.

6 Open Research

Analyses have been run using open source software (lsdtopotools v0.9, lsdtopotools). Precipitation data was retrieved using the package `gpm_precipitation_tools`. Visualization scripts and model workflows are available in the Github repository https://github.com/MarinaRuizSO/JGR_paper, which will be archived and assigned a doi if the manuscript is accepted for publication.

Acknowledgments

Funding for MRSO was provided by the Natural Environment Research Council (NERC NE/S007407/1). This research has been supported by the H2020 European Research Council (grant no. 803721). Perceptually uniform scientific color maps (Crameri, 2023) are used in this study to prevent visual distortion of the data and exclusion of readers with color-vision deficiencies (Crameri et al., 2020).

References

- Adams, B. A., Whipple, K. X., Forte, A. M., Heimsath, A. M., & Hodges, K. V. (2020). Climate controls on erosion in tectonically active landscapes. *Science Advances*, *6*, 3166–3182. doi: 10.1126/sciadv.aaz3166
- Anders, A. M., Roe, G. H., Hallet, B., Montgomery, D. R., Finnegan, N. J., & Putkonen, J. (2006). Spatial patterns of precipitation and topography in the Himalaya. *Special Paper of the Geological Society of America*, *398*, 39–53. doi: 10.1130/2006.2398(03)
- Armitage, J. J., Duller, R. A., Whittaker, A. C., & Allen, P. A. (2011). Transformation of tectonic and climatic signals from source to sedimentary archive. *Nature Geoscience*, *4*(4), 231–235. doi: 10.1038/ngeo1087
- Babault, J., Viaplana-Muzas, M., Legrand, X., Van Den Driessche, J., González-Quijano, M., & Mudd, S. M. (2018). Source-to-sink constraints on tectonic and sedimentary evolution of the western Central Range and Cenderawasih Bay (Indonesia). *Journal of Asian Earth Sciences*, *156*, 265–287. doi: 10.1016/j.jseaes.2018.02.004
- Baynes, E. R., Lague, D., Steer, P., Bonnet, S., & Illien, L. (2020). Sediment flux-

- 730 driven channel geometry adjustment of bedrock and mixed gravel–bedrock
 731 rivers. *Earth Surface Processes and Landforms*, 45(14), 3714–3731. doi:
 732 10.1002/esp.4996
- 733 Bernard, T., Sinclair, H. D., Gailleton, B., & Fox, M. (2021). Formation of Lon-
 734 gitudinal River Valleys and the Fixing of Drainage Divides in Response to
 735 Exhumation of Crystalline Basement. *Geophysical Research Letters*, 48(8),
 736 e2020GL092210. doi: 10.1029/2020GL092210
- 737 Bookhagen, B., & Burbank, D. W. (2006). Topography, relief, and TRMM-derived
 738 rainfall variations along the Himalaya. *Geophysical Research Letters*, 33(8),
 739 L08405. doi: 10.1029/2006GL026037
- 740 Bookhagen, B., & Strecker, M. R. (2008). Orographic barriers, high-resolution
 741 TRMM rainfall, and relief variations along the eastern Andes. *Geophysical
 742 Research Letters*, 35(6), L06403. doi: 10.1029/2007GL032011
- 743 Bovy, B., & Lange, R. (2023). *fastscape-lem/fastscape: Release v0.1.0*. Zenodo. doi:
 744 10.5281/ZENODO.8375653
- 745 Bradley, R. S. (2015). Climate and Climatic Variation. *Paleoclimatology*, 13–54. doi:
 746 10.1016/B978-0-12-386913-5.00002-8
- 747 Braun, J., & Willett, S. D. (2013). A very efficient O(n), implicit and par-
 748 allel method to solve the stream power equation governing fluvial inci-
 749 sion and landscape evolution. *Geomorphology*, 180–181, 170–179. doi:
 750 10.1016/j.geomorph.2012.10.008
- 751 Champagnac, J.-D., Molnar, P., Sue, C., & Herman, F. (2012). Tectonics, climate,
 752 and mountain topography. *Journal of Geophysical Research: Solid Earth*,
 753 117(B2). doi: 10.1029/2011JB008348
- 754 Cox, N. J. (2007). Kernel estimation as a basic tool for geomorphological data anal-
 755 ysis. *Earth Surface Processes and Landforms*, 32(12), 1902–1912. doi: 10.1002/
 756 esp.1518
- 757 Craddock, W. H., Burbank, D. W., Bookhagen, B., & Gabet, E. J. (2007). Bedrock
 758 channel geometry along an orographic rainfall gradient in the upper Marsyandi
 759 River valley in central Nepal. *Journal of Geophysical Research: Earth Surface*,
 760 112(3). doi: 10.1029/2006JF000589
- 761 Crameri, F. (2023). *Scientific colour maps*. Zenodo. doi: 10.5281/zenodo.8409685
- 762 Crameri, F., Shephard, G. E., & Heron, P. J. (2020). The misuse of colour in science
 763 communication. *Nature Communications*, 11. doi: 10.1038/s41467-020-19160-
 764 -7
- 765 D’Arcy, M., & Whittaker, A. C. (2014). Geomorphic constraints on landscape sen-
 766 sitivity to climate in tectonically active areas. *Geomorphology*, 204, 366–381.
 767 doi: 10.1016/j.geomorph.2013.08.019
- 768 Deal, E., Braun, J., & Botter, G. (2018). Understanding the Role of Rainfall and
 769 Hydrology in Determining Fluvial Erosion Efficiency. *Journal of Geophysical
 770 Research: Earth Surface*, 123(4), 744–778. doi: 10.1002/2017JF004393
- 771 Deal, E., Favre, A.-C., & Braun, J. (2017). Rainfall variability in the Himalayan oro-
 772 gen and its relevance to erosion processes. *Water Resources Research*, 53(5),
 773 4004–4021. doi: 10.1002/2016WR020030
- 774 DiBiase, R. A., & Whipple, K. X. (2011). The influence of erosion thresholds and
 775 runoff variability on the relationships among topography, climate, and erosion
 776 rate. *Journal of Geophysical Research: Earth Surface*, 116(F4), 4036. doi:
 777 10.1029/2011JF002095
- 778 DiBiase, R. A., Whipple, K. X., Heimsath, A. M., & Ouimet, W. B. (2010).
 779 Landscape form and millennial erosion rates in the San Gabriel Moun-
 780 tains, CA. *Earth and Planetary Science Letters*, 289(1–2), 134–144. doi:
 781 10.1016/J.EPSL.2009.10.036
- 782 Dunne, K. B. J., & Jerolmack, D. J. (2020). What sets river width? *Science Ad-
 783 vances*, 6(41), eabc1505. doi: 10.1126/sciadv.abc1505
- 784 Duvall, A., Kirby, E., Burbank, D., Duvall, C. ., Kirby, E., & Burbank, D. (2004).

- 785 Tectonic and lithologic controls on bedrock channel profiles and processes in
786 coastal California. *Journal of Geophysical Research: Earth Surface*, 109(F3),
787 3002. doi: 10.1029/2003JF000086
- 788 Ferrier, K. L., Huppert, K. L., & Perron, J. T. (2013). Climatic control of bedrock
789 river incision. *Nature*, 496(7444), 206–209. doi: 10.1038/nature11982
- 790 Finnegan, N. J., Sklar, L. S., & Fuller, T. K. (2007). Interplay of sediment supply,
791 river incision, and channel morphology revealed by the transient evolution of
792 an experimental bedrock channel. *Journal of Geophysical Research: Earth
793 Surface*, 112(F3). doi: 10.1029/2006JF000569
- 794 Flint, J. J. (1974). Stream gradient as a function of order, magnitude, and discharge.
795 *Water Resources Research*, 10(5), 969–973. doi: 10.1029/WR010i005p00969
- 796 Forte, A. M., Yanites, B. J., & Whipple, K. X. (2016). Complexities of landscape
797 evolution during incision through layered stratigraphy with contrasts in rock
798 strength. *Earth Surface Processes and Landforms*, 41(12), 1736–1757. doi:
799 10.1002/esp.3947
- 800 Fournier, A., Fussell, D., & Carpenter, L. (1982). Computer Rendering of Stochastic
801 Models. *Commun. ACM*, 25(6), 371–384. doi: 10.1145/358523.358553
- 802 Gailleton, B., Mudd, S. M., Clubb, F. J., Grieve, S. W., & Hurst, M. D. (2021).
803 Impact of Changing Concavity Indices on Channel Steepness and Divide Mi-
804 gration Metrics. *Journal of Geophysical Research: Earth Surface*, 126(10). doi:
805 10.1029/2020JF006060
- 806 Gasparini, N. M., & Brandon, M. T. (2011). A generalized power law approximation
807 for fluvial incision of bedrock channels. *Journal of Geophysical Research: Earth
808 Surface*, 116(2), 1–16. doi: 10.1029/2009JF001655
- 809 Gasparini, N. M., & Whipple, K. X. (2014). Diagnosing climatic and tectonic
810 controls on topography: Eastern flank of the northern Bolivian Andes. *Litho-
811 sphere*, 6(4). doi: 10.1130/L322.1
- 812 Gasparini, N. M., Whipple, K. X., & Bras, R. L. (2007). Predictions of steady
813 state and transient landscape morphology using sediment-flux-dependent river
814 incision models. *Journal of Geophysical Research*, 112(F3), F03S09. doi:
815 10.1029/2006JF000567
- 816 Gilbert, G. (1877). *Geology of the Henry Mountains* (Tech. Rep.). Washington,
817 D.C.: Government Printing Office.
- 818 Goren, L., Fox, M., & Willett, S. D. (2014). Tectonics from fluvial topography using
819 formal linear inversion: Theory and applications to the Inyo Mountains, Cal-
820 ifornia. *Journal of Geophysical Research: Earth Surface*, 119(8), 1651–1681.
821 doi: 10.1002/2014JF003079
- 822 Grujic, D., Govin, G., Barrier, L., Bookhagen, B., Coutand, I., Cowan, B., ... Naj-
823 man, Y. (2018). Formation of a Rain Shadow: O and H Stable Isotope Records
824 in Authigenic Clays From the Siwalik Group in Eastern Bhutan. *Geochemistry,
825 Geophysics, Geosystems*, 19(9), 3430–3447. doi: 10.1029/2017GC007254
- 826 Hack, J. T. (1960). Interpretation of erosional topography in humid temperate re-
827 gions. *American Journal of Science*, 258(A), 80–97.
- 828 Han, J., Gasparini, N. M., & Johnson, J. P. (2015). Measuring the imprint of oro-
829 graphic rainfall gradients on the morphology of steady-state numerical fluvial
830 landscapes. *Earth Surface Processes and Landforms*, 40(10), 1334–1350. doi:
831 10.1002/esp.3723
- 832 Harel, M. A., Mudd, S. M., & Attal, M. (2016). Global analysis of the stream power
833 law parameters based on worldwide ¹⁰Be denudation rates. *Geomorphology*,
834 268, 184–196. doi: 10.1016/j.geomorph.2016.05.035
- 835 Harries, R. M., Gailleton, B., Kirstein, L. A., Attal, M., Whittaker, A. C., & Mudd,
836 S. M. (2021). Impact of climate on landscape form, sediment transfer and the
837 sedimentary record. *Earth Surface Processes and Landforms*, 46(5), 990–1006.
838 doi: 10.1002/esp.5075
- 839 Hergarten, S., & Robl, J. (2022). The linear feedback precipitation model (LFPM

- 1.0) – a simple and efficient model for orographic precipitation in the context
of landform evolution modeling. *Geoscientific Model Development*, 15(5),
2063–2084. doi: 10.5194/gmd-15-2063-2022
- Hergarten, S., Robl, J., & Stüwe, K. (2016). Tectonic geomorphology at small catch-
ment sizes—extensions of the stream-power approach and the χ method. *Earth
Surface Dynamics*, 4, 1–9. doi: 10.5194/esurf-4-1-2016
- Herman, F., Seward, D., Valla, P. G., Carter, A., Kohn, B., Willett, S. D., & Ehlers,
T. A. (2013). Worldwide acceleration of mountain erosion under a cooling
climate. *Nature*, 504(7480), 423–426. doi: 10.1038/nature12877
- Howard, A. D. (1987). Modelling fluvial systems: rock-, gravel- and sand-bed chan-
nels. In K. Richards (Ed.), *River channels* (p. 69-94). Oxford: Basil Blackwell.
- Howard, A. D., & Kerby, G. (1983). Channel changes in badlands. *GSA Bulletin*,
94(6), 739–752. doi: 10.1130/0016-7606(1983)94<739:CCIB>2.0.CO;2
- Johnson, J. P. L., & Whipple, K. X. (2010). Evaluating the controls of shear
stress, sediment supply, alluvial cover, and channel morphology on experimen-
tal bedrock incision rate. *Journal of Geophysical Research: Earth Surface*,
115(F2). doi: 10.1029/2009JF001335
- Kirby, E., & Whipple, K. (2001). Quantifying differential rock-uplift rates
via stream profile analysis. *Geology*, 29(5), 415–418. doi: 10.1130/
0091-7613(2001)029<0415:QDRURV>2.0.CO;2
- Kirby, E., & Whipple, K. X. (2012). Expression of active tectonics in erosional land-
scapes. *Journal of Structural Geology*, 44, 54–75. doi: 10.1016/J.JSG.2012.07
.009
- Kummerow, C., Simpson, J., Thiele, O., Barnes, W., Chang, A. T., Stocker, E., ...
Nakamura, K. (2000). The status of the tropical rainfall measuring mission
(TRMM) after two years in orbit. *Journal of Applied Meteorology*, 39(12
PART 1), 1965–1982. doi: 10.1175/1520-0450(2001)040<1965:tsottr>2.0.co;2
- Lague, D. (2014). The stream power river incision model: Evidence, theory and be-
yond. *Earth Surface Processes and Landforms*, 39(1), 38–61. doi: 10.1002/esp
.3462
- Leonard, J. S., & Whipple, K. X. (2021). Influence of spatial rainfall gradients on
river longitudinal profiles and the topographic expression of spatially and tem-
porally variable climates in mountain landscapes. *Journal of Geophysical Re-
search: Earth Surface*, 126(12), e2021JF006183. doi: 10.1029/2021JF006183
- Leonard, J. S., Whipple, K. X., & Heimsath, A. M. (2023). Isolating climatic,
tectonic, and lithologic controls on mountain landscape evolution. *Science
advances*, 9(3), eadd8915. doi: 10.1126/sciadv.add8915
- Montgomery, D. R., Balco, G., & Willett, S. D. (2001). Climate, tectonics, and
the morphology of the Andes. *Geology*, 29(7), 579–582. doi: 10.1130/0091
-7613(2001)029<0579:CTATMO>2.0.CO;2
- Morisawa, M. E. (1962). Quantitative Geomorphology of Some Watersheds in the
Appalachian Plateau. *Geological Society of America Bulletin*, 73(9), 1025–
1046. doi: 10.1130/0016-7606(1962)73[1025:QGOSWI]2.0.CO;2
- Mudd, S. M., Attal, M., Milodowski, D. T., Grieve, S. W., & Valters, D. A. (2014).
A statistical framework to quantify spatial variation in channel gradients us-
ing the integral method of channel profile analysis. *Journal of Geophysical
Research: Earth Surface*, 119(2), 138–152. doi: 10.1002/2013JF002981
- Mudd, S. M., Clubb, F. J., Gailleton, B., & Hurst, M. D. (2018). How concave are
river channels? *Earth Surface Dynamics*, 6(2), 505–523. doi: 10.5194/ESURF
-6-505-2018
- Peifer, D., Persano, C., Hurst, M. D., Bishop, P., & Fabel, D. (2021). Growing to-
pography due to contrasting rock types in a tectonically dead landscape. *Earth
Surface Dynamics*, 9(2), 167–181. doi: 10.5194/ESURF-9-167-2021
- Perlin, K. (1985). Image synthesizer. *Computer Graphics (ACM)*, 19, 287–296. doi:
10.1145/325165.325247

- 895 Perron, J. T., & Royden, L. (2013). An integral approach to bedrock river profile
896 analysis. *Earth Surface Processes and Landforms*, *38*(6), 570–576. doi: 10
897 .1002/esp.3302
- 898 Pfeiffer, A. M., Finnegan, N. J., & Willenbring, J. K. (2017). Sediment supply con-
899 trols equilibrium channel geometry in gravel rivers. *Proceedings of the National*
900 *Academy of Sciences*, *114*(13), 3346–3351. doi: 10.1073/pnas.1612907114
- 901 Phillips, C. B., & Jerolmack, D. J. (2016). Self-organization of river channels as a
902 critical filter on climate signals. *Science*, *352*(6286), 694–697. doi: 10.1126/
903 science.aad3348
- 904 Rasmussen, K. L., Chaplin, M. M., Zuluaga, M. D., & Houze, R. A. (2016). Contri-
905 bution of Extreme Convective Storms to Rainfall in South America. *Journal of*
906 *Hydrometeorology*, *17*(1), 353–367. doi: 10.1175/JHM-D-15-0067.1
- 907 Roe, G. H., Montgomery, D. R., & Hallet, B. (2002). Effects of orographic precipi-
908 tation variations on the concavity of steady-state river profiles. *Geology*, *30*(2),
909 143–146. doi: 10.1130/0091-7613(2002)030<0143:EOOPVO>2.0.CO;2
- 910 Roe, G. H., Montgomery, D. R., & Hallet, B. (2003). Orographic precipitation and
911 the relief of mountain ranges. *Journal of Geophysical Research: Solid Earth*,
912 *108*(B6), 2315. doi: 10.1029/2001JB001521
- 913 Rossi, M. W., Whipple, K. X., & Vivoni, E. R. (2016). Precipitation and evapotran-
914 spiration controls on daily runoff variability in the contiguous United States
915 and Puerto Rico. *Journal of Geophysical Research: Earth Surface*, *121*(1). doi:
916 10.1002/2015JF003446
- 917 Royden, L., & Perron, J. T. (2013). Solutions of the stream power equation and ap-
918 plication to the evolution of river longitudinal profiles. *Journal of Geophysical*
919 *Research: Earth Surface*, *118*(2), 497–518. doi: 10.1002/jgrf.20031
- 920 Royden, L. H., Clark, M. K., & Whipple, K. X. (2000). Evolution of river elevation
921 profiles by bedrock incision: Analytical solutions for transient river profiles
922 related to changing uplift and precipitation rates. *Eos Trans. AGU*, *81*(48),
923 *Fall Meet. Suppl., Abstract T62F-09*. doi: 10.1002/eost.v81.16
- 924 Silverman, B. W. (1998). *Density estimation for statistics and data analysis*. Rout-
925 ledge. doi: 10.1201/9781315140919
- 926 Skofronick-Jackson, G., Petersen, W. A., Berg, W., Kidd, C., Stocker, E. F.,
927 Kirschbaum, D. B., ... Wilheit, T. (2017). The global precipitation mea-
928 surement (GPM) mission for science and Society. *Bulletin of the American*
929 *Meteorological Society*, *98*(8), 1679–1695. doi: 10.1175/BAMS-D-15-00306.1
- 930 Smith, R. B., & Barstad, I. (2004). A linear theory of orographic precipi-
931 tation. *Journal of the Atmospheric Sciences*, *61*(12), 1377–1391. doi:
932 10.1175/1520-0469(2004)061<1377:ALTOOP>2.0.CO;2
- 933 Sorensen, C. S., & Yanites, B. J. (2019). Latitudinal trends in modern fluvial ero-
934 sional efficiency along the Andes. *Geomorphology*, *329*, 170–183. doi: 10.1016/
935 j.geomorph.2018.12.030
- 936 Tucker, G. E., & Whipple, K. X. (2002). Topographic outcomes predicted by stream
937 erosion models: Sensitivity analysis and intermodel comparison. *Journal of*
938 *Geophysical Research: Solid Earth*, *107*(B9), 1–1. doi: 10.1029/2001JB000162
- 939 Ward, D. J., & Galewsky, J. (2014). Exploring landscape sensitivity to the Pacific
940 Trade Wind Inversion on the subsiding island of Hawaii. *Journal of Geophysi-
941 cal Research: Earth Surface*, *119*(9), 2048–2069. doi: 10.1002/2014JF003155
- 942 Whipple, K. X., & Tucker, G. E. (1999). Dynamics of the stream-power river in-
943 cision model: Implications for height limits of mountain ranges, landscape
944 response timescales, and research needs. *Journal of Geophysical Research:*
945 *Solid Earth*, *104*(B8), 17661–17674. doi: 10.1029/1999JB900120
- 946 Whipple, K. X., & Tucker, G. E. (2002). Implications of sediment-flux-dependent
947 river incision models for landscape evolution. *Journal of Geophysical Research:*
948 *Solid Earth*, *107*(B2), 3–1. doi: 10.1029/2000JB000044
- 949 Wickert, A. D., & Schildgen, T. F. (2019). Long-profile evolution of transport-

- 950 limited gravel-bed rivers. *Earth Surface Dynamics*, 7(1), 17–43. doi: 10.5194/
951 ESURF-7-17-2019
- 952 Wobus, C. W., Tucker, G. E., & Anderson, R. S. (2006). Self-formed bedrock
953 channels. *Geophysical Research Letters*, 33(18), 18408. doi: 10.1029/
954 2006GL027182
- 955 Wobus, C. W., Tucker, G. E., & Anderson, R. S. (2010). Does climate change create
956 distinctive patterns of landscape incision? *Journal of Geophysical Research:*
957 *Earth Surface*, 115(4). doi: 10.1029/2009JF001562
- 958 Zaprowski, B. J., Pazzaglia, F. J., & Evenson, E. B. (2005). Climatic influences
959 on profile concavity and river incision. *Journal of Geophysical Research: Earth*
960 *Surface*, 110(F3), 3004. doi: 10.1029/2004JF000138

Supporting Information for “Quantifying channel steepness distortion resulting from rainfall gradients and concavity changes”

Marina Ruiz Sánchez-Oro¹, Simon M. Mudd¹, and Boris Gailleton²

¹School of GeoSciences, University of Edinburgh, Edinburgh, UK

²CNRS, Rennes, France

Contents of this file

1. Text S1 to S6
2. Figures S1 to S19
3. Tables S1 to S9

Introduction This supporting information document contains the derivation of the distortion metrics used in the main text. In addition we present the model parameters and lithologic scenarios. We also provide additional figures for distortion as a function of the change in rainfall as well as for different scenarios of the concavity index.

Text S1. Calculation of k_{sn} distortion

Distortions in the local values of k_{sn} can affect the interpretation of the tectonic and erosional history of a landscape (e.g. Kirby & Whipple, 2012). In order to measure the extent of the k_{sn} distortion caused by different θ values, or alternatively application of

either discharge or area driven calculation of the χ metric, we follow a method similar to that described by (Gailleton et al., 2021).

For the equations below, we compare values in two areas within the same catchment and take the median value of all the $k_s n$ values within that area. The equations below are then quoted in terms of medians instead of absolute values, as was originally devised by (Gailleton et al., 2021).

We start by defining $k_s n$ at two points in the catchment, defined by their median slope and drainage area. We label these points M and N , and use subscripts to denote which point is being analysed:

$$k_M = S_M A_M^\theta \quad (\text{S1})$$

and

$$k_N = S_N A_N^\theta \quad (2)$$

We then take the ratio between the two values of $k_s n$, this we call $r_{k,\theta}$.

$$r_{k,\theta} = \frac{S_M A_M^\theta}{S_N A_N^\theta} \quad (3)$$

To simplify the equation, we can express the drainage area and the slope ratios as r_S and r_A^θ :

$$r_{k,\theta} = r_S r_A^\theta \quad (4)$$

Since we are investigating the effect of varying the concavity between two θ values, we can define:

$$\Delta\theta = \theta_2 - \theta_1 \quad (5)$$

Transforming this into natural log space, we can then see the linear relations between the terms. Note that only the drainage area ratios depend on the concavity θ , which allows us to remove the dependence on the slope ratios, r_S .

$$\ln[r_{k,\theta_2}] - \ln[r_{k,\theta_1}] = \ln[r_S] + \theta_2 \ln[r_A] - \ln[r_S] - \theta_1 \ln[r_A] \quad (6)$$

$$\ln[r_{k,\theta_2}] - \ln[r_{k,\theta_1}] = \Delta\theta \ln[r_A] \quad (7)$$

Finally, we can rewrite this ratio of ratios as a distortion originated from the variation in θ values.

$$\beta(\Delta\theta) = \frac{r_{k,\theta_2}}{r_{k,\theta_1}} = r_A^{\Delta\theta} \quad (8)$$

We then use these equations with the following series of steps in order calculate the degree of distortion in k_{sn} values that may be introduced by selection of the wrong method of calculating χ (for example, using A to calculate χ_A when incision depends on Q).

1. We select tributaries based on the drainage area: normalise the drainage area (DA^*) to be able to establish a common threshold for all the basins.
2. We remove the pixels that have a $DA^* < 0.1$.
3. We choose the pixels corresponding to larger rivers ($DA^* > 0.8$) and those belonging to side tributaries ($DA^* < 0.3$).

4. We normalise the k_{sn} values by the largest value in each basin.
5. We take the median value of the k_{sn}^* values for the smaller and the larger tributaries.
6. We calculate the ratio between the two medians (large DA/small DA).

These calculations are aimed at quantifying the distortion in k_{sn} related to a change in concavity index, θ . To study the distortion incurred by a change in incision rule (i.e. using discharge instead of drainage area) we need to introduce a further variable. We express discharge as $Q = RA$, where R is the rainfall rate (m/yr). The framework is the same, but we define the discharge k_{sn} ratio as:

$$r_{k,\theta,Q} = \frac{S_M(R_M A_M)^\theta}{S_N(R_N A_N)^\theta} \quad (9)$$

which we express as

$$r_{k,\theta,Q} = r_S (r_R r_A)^\theta \quad (10)$$

To see the distortion caused by the inclusion of rainfall in the calculations we take the ratio between r_k and $r_{k,Q}$:

$$r_{k,\theta,Q} = \frac{r_S (r_R r_A)^\theta}{r_S r_A^\theta} \quad (11)$$

If we assume a constant value for θ , the equation becomes:

$$\frac{r_{k,\theta,Q}}{r_{k,\theta}} = r_R^\theta \quad (12)$$

If we then combine both k_{sn} distortion cases (i.e. change in θ and change in incision rule) together we get the following expressions:

$$\frac{r_{k,Q,\theta_1}}{r_{k,\theta_2}} = \frac{r_S r_R^{\theta_1} r_A^{\theta_1}}{r_S r_A^{\theta_2}} \quad (13)$$

doing the natural log transformation of equation 13 leads to the ratio:

$$\frac{r_{k,Q,\theta_1}}{r_{k,\theta_2}} = r_R^{\theta_1} + r_A^{\Delta\theta} \quad (14)$$

Equations 8, 12, and 14 allow us to quantify three varieties of distortion: those caused by changes in θ , those caused by changes in the incision rule, and a combination of both. To capture the variety of distortion we calculate four distortion ratios:

- $\frac{k_{sn}(\theta=\theta_{best})}{k_{sn}(\theta=0.45)}$ (Distortion case i_A)
- $\frac{k_{sn-q}(\theta=\theta_{best})}{k_{sn-q}(\theta=0.45)}$ (Distortion case i_Q)
- $\frac{k_{sn}(\theta=\theta_{best})}{k_{sn-q}(\theta=\theta_{best})}$ (Distortion case ii)
- $\frac{k_{sn}(\theta=0.45)}{k_{sn-q}(\theta=0.45)}$ (Distortion case iii)

A ratio value of 1 means that there is no change in the k_{sn} values being compared, whereas values above or below 1 show a trend in either of the directions.

We always take basin M to be the larger basin. That is, This means that the ratio $A_M/A_N > 1$ in all our calculations. To understand what this means physically, we consider the following scenarios:

- Case a): k_{sn} distortion > 1
- Case b): k_{sn} distortion < 1

In this case, the area M has a larger drainage area than the area N in the calculations. Given this, for Case a), this implies that $\theta_2 > \theta_1$. In Case b), the opposite is true, $\theta_1 > \theta_2$.

When we have only a difference in the incision case, the distortion signal is dominated by the strength of the rainfall gradient. In our set up, the rainfall increases toward the east of the simulation. We will refer to the western-facing basins “dry” and the eastern-facing basins as “wet”. In this case, a change of sign in the k_{sn} distortion arises from $R_M/R_N < 1$ on the dry basins and $R_M/R_N > 1$ on the wet basins.

Case *i*: Distortion from changes in θ

Distortion:

$$r_A^{\Delta\theta} = \left(\frac{A_M}{A_N}\right)^{\theta_2 - \theta_1} \quad (15)$$

$$\theta_2 > \theta_1 \Rightarrow \left(\frac{A_M}{A_N}\right)^+ \Rightarrow r_A^{\Delta\theta} > 1 \quad (16)$$

$$\theta_2 < \theta_1 \Rightarrow \left(\frac{A_M}{A_N}\right)^- \Rightarrow r_A^{\Delta\theta} < 1 \quad (17)$$

$$(18)$$

Based on the distortion value we can find out what the relationship between the different θ is and vice versa. In our case θ_1 is the numerator and θ_2 the denominator in the 4 distortion ratios above. Larger θ values mean faster change of gradient downstream.

Case *ii*: Distortion from changes in incision rule (rainfall)

In this case, we are not comparing the effect of different θ so we only focus on the rainfall impact. We assume that θ is fixed to some reference value, in this case $\theta = 0.45$.

Distortion:

$$r_R^\theta = \left(\frac{R_M}{R_N}\right)^\theta \quad (19)$$

As explained above, we reason through this step in terms of dry and wet basins:

$$\text{Dry side : } R_M < R_N \Rightarrow \left(\frac{R_M}{R_N}\right)^{0.45} < 1 \Rightarrow r_R^\theta < 1 \quad (20)$$

$$\text{Wet side : } R_M > R_N \Rightarrow \left(\frac{R_M}{R_N}\right)^{0.45} > 1 \Rightarrow r_R^\theta > 1 \quad (21)$$

$$(22)$$

In this case, given the rainfall constraints that we have in the simulations, the maximum value for r_R is 10 (as this is the largest gradient case).

Case *iii*: Distortion from changes in θ and incision rule (due to rainfall)

Distortion:

$$r_R^\theta + r_A^{\Delta\theta} = \left(\frac{R_M}{R_N}\right)^{\theta_1} + \left(\frac{A_M}{A_N}\right)^{\Delta\theta} \quad (23)$$

Always: $A_M > A_N$

Dry: $R_M < R_N$

Wet: $R_M > R_N$

$\theta_1 \gg \Delta\theta$

We study the two terms in the distortion equation.

Distortion < 1 :

Dry side:

$$\left(\frac{R_M}{R_N}\right)^{0.45} < 1 \quad (24)$$

$$\left(\frac{A_M}{A_N}\right)^{0.45} > 1 \quad (25)$$

$$(26)$$

For the overall distortion to be negative, $\Delta\theta < 0$. So that $\theta_1 > \theta_2$.

Wet side:

$$\left(\frac{R_M}{R_N}\right)^{0.45} > 1 \quad (27)$$

$$\left(\frac{A_M}{A_N}\right)^{0.45} > 1 \quad (28)$$

$$(29)$$

From these parameters, the distortion will never be below 1 in this case for the wet area.

Distortion > 1 :

Dry side:

$$\left(\frac{R_M}{R_N}\right)^{0.45} < 1 \quad (30)$$

$$\left(\frac{A_M}{A_N}\right)^{0.45} > 1 \quad (31)$$

$$(32)$$

For the overall distortion to be above 1 for the dry side, $\theta_2 > \theta_1$.

Wet side:

$$\left(\frac{R_M}{R_N}\right)^{0.45} > 1 \quad (33)$$

$$\left(\frac{A_M}{A_N}\right)^{0.45} > 1 \quad (34)$$

$$(35)$$

From these parameters, the distortion in the wet side will always be above 1 in this case for the wet area regardless of θ .

Text S2. Model parameters

For our numerical simulations, we run models using the parameters described in Table S1.

Text S3. Lithologic scenarios

We run simulations with a number of different lithologic scenarios, examples of which are shown in Figure S1.

Dense blob lithology

The drainage area-driven incision is represented in Figure S2A. Compared to Figure S11A, we notice that the distinctions between calculating disorder with and without rainfall are largely masked by the presence of a heterogeneous lithology. In this drainage area-driven case, we would expect that calculating χ_A would lead to higher disorder values than using χ_Q . However, this is not clearly seen, with the results yielding the lowest disorder being mixed.

Even though from the overall behavior it is difficult to pick out the scenario with the least disorder. Looking at individual pairs of basins, we can see a signal. Note that in this case, the basins are identical regardless of the rainfall gradient, as there is only one model evolution. We can see that for each of the basins, the value for the case χ_Q presents higher disorder values than χ_A . In this case, the behaviour of the basins becomes case specific. In S11, A, all basins showed a base disorder close to 0 as there were no forcings present and therefore and consequent disorder calculations with χ_Q shows always higher disorder value regardless of the basin or the rainfall gradient. In this case, however, we

see that the baseline disorder for χ_A has increased from 0 by up to 14% in some basins. We still see, however, that the basins record a lower disorder when χ_A is calculated, as we expect from a drainage area-driven scenario.

In Figure S2B, we can see the effects of adding rainfall. Similarly to Figure S2A, it is very difficult to distinguish the signal from each of the χ cases in terms of the overall behaviour of all the basins in the same simulation run (for each rainfall gradient). If we look at individual basins, however, we see that the disorder is smaller when we use χ_Q for some of the basins.

Blob lithology

We present results from the blob lithology simulations in Figures S5, S6, and S7. The distortions associated with this scenario are shown in Table S7.

Striped Lithology

We present results from the striped lithology simulations in Figures S8, S9, and S10. The distortions associated with this scenario are shown in Table S10.

Text S4. Incision: Drainage Area vs Incision: Discharge

Figure S11 shows how D^* responds to changes in both rainfall gradients and incision rule (one basin is represented by one plot point). In the A -driven incision experiment (top plot), we expect the $\chi_A - z$ profiles to be linear and the associated $\theta_{best,A}$ to be 0.45. The disorder in this case is close to 0 for all the basins in all rainfall instances. In contrast, calculation using χ_Q results in more disorder and values of $\theta_{best,Q}$ that diverge from 0.45, with the differences increasing as the rainfall gradient increases.

Figure S11B portrays the effect of including rainfall in the χ_A calculations, given a Q -driven incision model. In this case, there are as many models as there are rainfall

scenarios, with the first one corresponding to the A -driven incision model with a base rainfall of 1 m/yr and no gradient. Calculating χ_Q with matching incision rule rainfall gradient yields D^* values of 0 compared to calculating χ_A . For instance, in the model run with a rainfall gradient of 5 m/yr, the χ_Q calculations with 5 m/yr will yield a lower disorder than calculating χ_A (without rainfall). This also means that the value for $\theta_{best,Q}$ will be 0.45 in that case. We see that as the rainfall gradient increases the differences between the minimum disorder values increases, and the model behaviour diverges from the A -driven incision case.

Note that in the discharge-driven incision case, the simulated basins vary under each of the rainfall scenarios, showing the differences that different rainfall gradients make in the evolution of basins. In the drainage area incision case we only have one set of simulated basins as the modelling conditions are the same and it is only in the χ calculations that we incorporate a dependence on rainfall.

In the drainage area scenario, the variations in χ_Q and $\theta_{best,Q}$ arise from including a rainfall gradient in the calculations, they are purely a mathematical bias. In the discharge scenarios, changes in χ_Q are captured from changes in the topography of the simulated basins due to the imposed rainfall gradients.

The scale of the change in disorder varies between the two incision scenarios. In the A -driven case (plot A), disorder ranges between less than 0.01 (when calculating χ_A with the 1 m/yr rainfall gradient) and over 0.04 (with a 10 m/yr χ_A calculation). On the other hand, the Q -driven scenario leads to larger disorder changes of one order of magnitude, ranging from 0.01 to 0.14. Thus, when applying disorder minimisation, choosing the

incorrect incision rule leads to stronger variations in optimal θ_{best} when discharge is the main incision mechanism.

Text S5. Disorder in natural landscapes

Figure S14 shows the values of the minimum D^* points for χ_A and χ_Q for all the selected mountain ranges. We see a resemblance with the model results with heterogeneous lithology, where it is difficult to distinguish whether there is an overall trend suggesting the preference of one incision mechanism over another at a large scale.

The disorder value ranges are considerably larger than those for the model runs. In natural landscapes, the minimum D^* values range between 0.1 and 0.75. We compare this to the minimum D^* from the simulations, where the maximum disorder was 0.4 for the discharge-driven heterogeneous lithology case and 0.14 for the discharge-driven homogeneous lithology case.

We note that basins within the same geographical area have ΔD^* of up to 0.4. The differences when calculating D^* with or without rainfall are one order of magnitude smaller, which makes it challenging to compare the influence of disorder across multiple mountain range of different scales.

Text S6. Effect of varying the concavity index, θ : 0.35 and 0.55

In the following section we explore how choosing $\theta = 0.45$ in a landscape carved by a different m/n ratio affects the k_{sn} distortion. We highlight this case because of the large body of literature that assumes $\theta = 0.45$ when deriving erosion rates and determining the tectonic history of a basin. Figure S16 reflects data run from models with $m/n = 0.35$, where the resulting landscapes show higher relief and straighter rivers than those for $m/n = 0.45$.

The plots from a discharge driven model (Figure S16) suggests that regardless of the incision case chosen, the wrong concavity ($\theta = 0.45$ in this case) will lead to k_{sn} distortions reaching 30% (plots A and B). The ratios are all > 1 , which is in line with the mathematical formulation of distortion, given $\theta_1 = 0.35$ and $\theta_2 = 0.45$. Opting for the incorrect incision scenario (Figure S16C) under $\theta = 0.35$ leads to a smaller distortions of up to 13% for the largest rainfall gradient scenario.

This implies that analysing the incision pattern for a landscape where the concavity rule is not constrained, a mistaken choice of $\theta = 0.45$ causes larger distortion than assuming the incorrect incision scenario.

Next we choose $m/n = 0.55$ (Figure S18), which forms a landscape with lower relief and more sinuous rivers than $m/n = 0.45$. The behaviour is similar to that of the $m/n = 0.35$ scenario, but in this case the distortion is < 1 when we compare the effects of choosing 0.45 or 0.55 for θ (Figures S18A and B). There is no change in the distortion values based on the rainfall in Figure S18A and B. The highest distortion occurs when using optimising θ under the incorrect incision scenario (Figure S18D). The maximum distortion originated

from varying the incision rule is lower compared to the other scenarios (Figure S18E, 13% compared to 20-26% in Figures S18A, B, D).

Aside from the distortions in k_{sn} and k_{sn-q} , we also include the distributions of steepness indices under different rainfall, concavity and incision scenarios. In Figure S13, we show the distributions for the cases when the initial $m/n = 0.45$. The absolute channel steepness index values show a bimodal distribution when we use the optimal concavity, but a smoother and narrower monomodal shape when using 0.45. We see that for the A -driven incision, under $\theta = 0.45$, including rainfall gradients in the calculations increases the channel steepness values. When we have the Q -driven incision case, we obtain lower channel steepness values when we do not include rainfall in the calculations. Between the two incision cases, channel steepness is reduced with increased precipitation rates, with variability depending on the values of the concavity, as quantified by (D'Arcy & Whittaker, 2014).

References

- D'Arcy, M., & Whittaker, A. C. (2014). Geomorphic constraints on landscape sensitivity to climate in tectonically active areas. *Geomorphology*, *204*, 366–381. doi: 10.1016/j.geomorph.2013.08.019
- Gailleton, B., Mudd, S. M., Clubb, F. J., Grieve, S. W., & Hurst, M. D. (2021). Impact of Changing Concavity Indices on Channel Steepness and Divide Migration Metrics. *Journal of Geophysical Research: Earth Surface*, *126*(10). doi: 10.1029/2020JF006060
- Kirby, E., & Whipple, K. X. (2012). Expression of active tectonics in erosional landscapes. *Journal of Structural Geology*, *44*, 54–75. doi: 10.1016/J.JSG.2012.07.009

Table S1. Summary of the conditions upon which the distortion in k_{sn} values are above or below 1 for distortion calculated with changes in incision rate and θ .

	DRY	WET
Dist. < 1 $\theta_1 > \theta_2$ AND ratio dependence		ALWAYS
Dist. > 1 ALL θ , ratio dependence		NEVER

Table S2. Model parameters values for the initial conditions of the discharge simulation.

Parameter	Value
<i>Pixel resolution (m)</i>	30
<i>Lx (m)</i>	1.5e4
<i>Ly (m)</i>	3e4
<i>Diamond min height (m)</i>	0
<i>Diamond max height (m)</i>	1
<i>Roughness</i>	0.75
<i>Random seed</i>	420
<i>K (m⁻¹yr⁻¹)</i>	3e-8
<i>EU (m⁻¹)</i>	1e-5
<i>snastm</i>	0.45
<i>n</i>	1

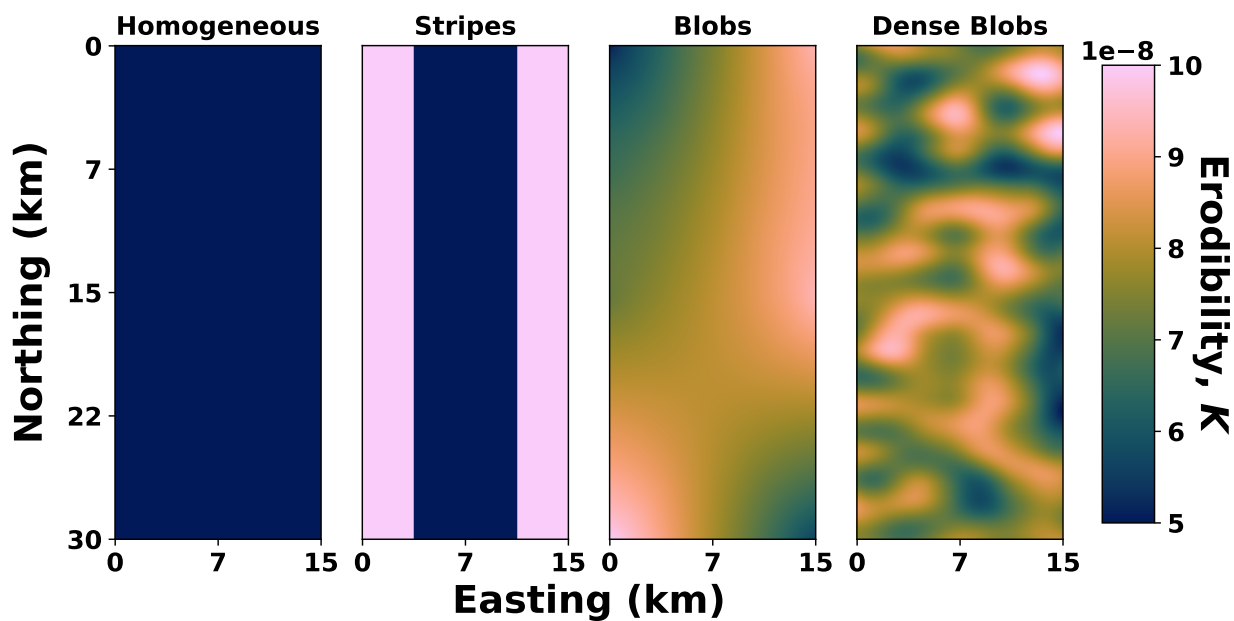


Figure S1. The four types of lithologies modelled: (a) Homogeneous lithology, (b) Striped lithology, (c) blob lithology and (d) dense blob lithology.

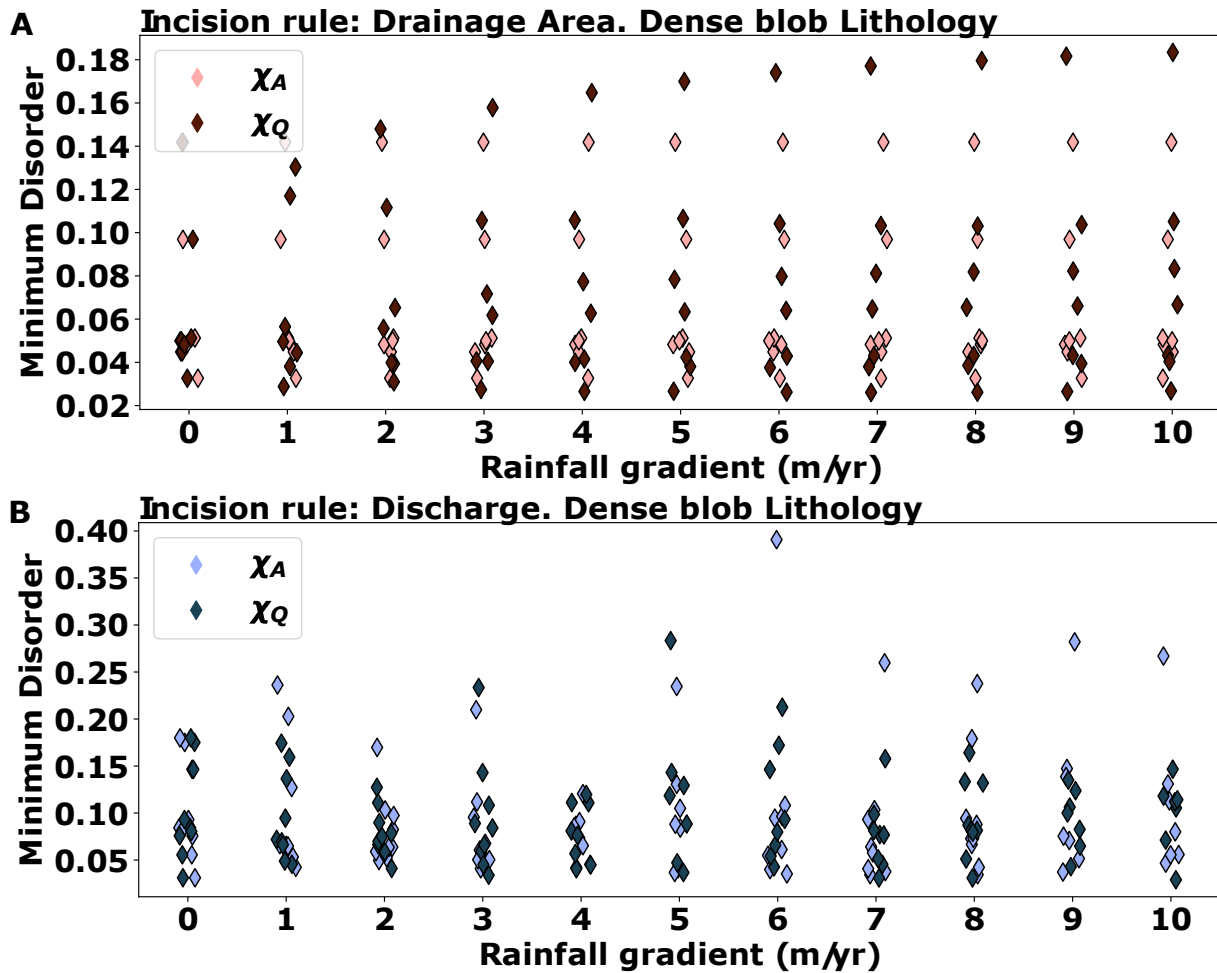


Figure S2. Evolution of the minimum disorder for model runs with drainage area (A) and discharge-driven (B) incision rule for a range of rainfall gradients (0-10m/yr) under dense blob lithology. We show the minimum disorder values when calculating χ_A and χ_Q , for rainfall values increasing from 0 m/yr to 10 m/yr. Under a dense blob lithology it is not possible to establish a pattern in disorder values when using χ_A as opposed to χ_Q , regardless of the incision scenario.

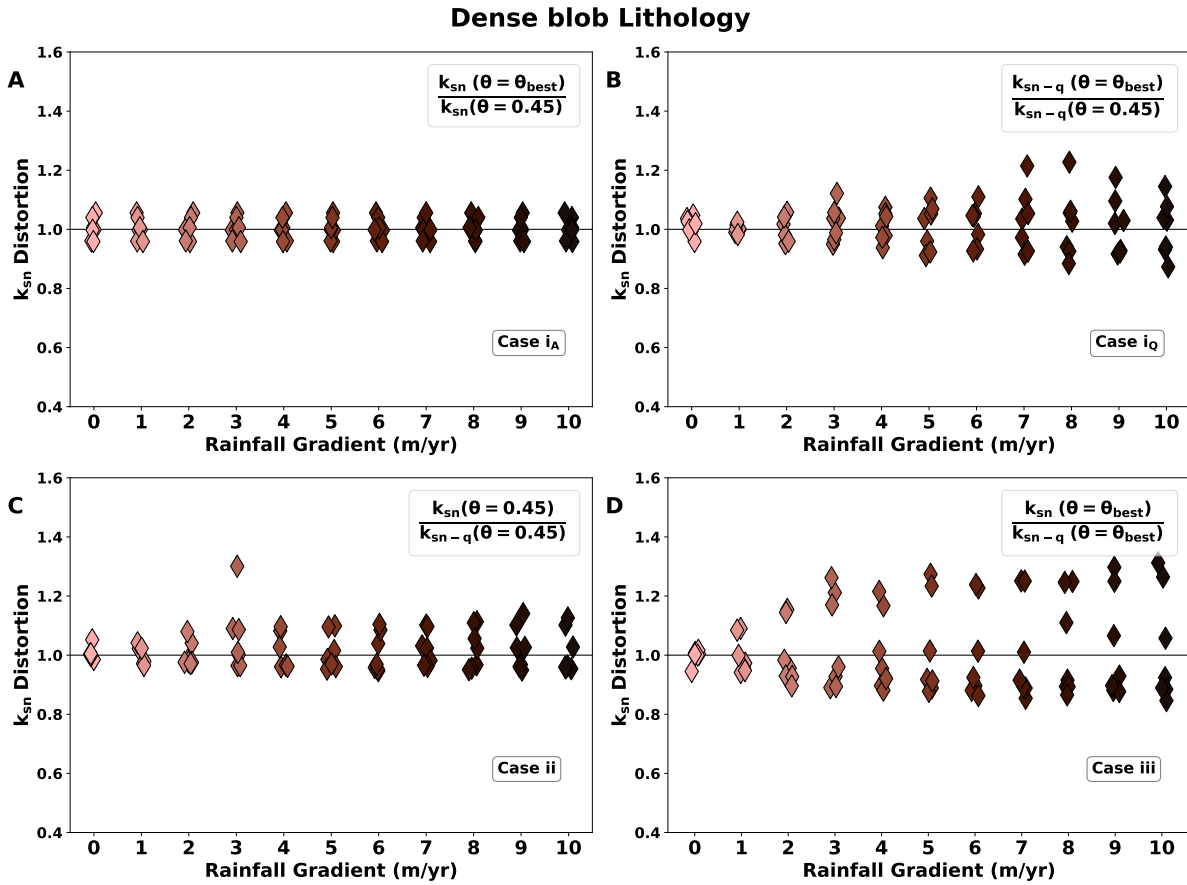


Figure S3. Distortion in k_{sn} for the A -driven incision case under dense blob lithology and initial $m/n=0.45$. A distortion of 1 (solid black line) keeps the value of k_{sn} unchanged. We show the possible distortion scenarios that one might encounter under different assumptions of concavity index and incision. (A) shows the distortion incurred by not optimising θ under A -driven incision, whereas (B) highlights the effects of optimising concavity under the incorrect incision scenario (discharge), where we see the largest k_{sn} distortions of up to 34%. (C) keeps concavity index at 0.45 but compares incision scenario and (D) comprises the effects of θ optimisation under different assumptions of incision scenarios.

Dense blob lithology

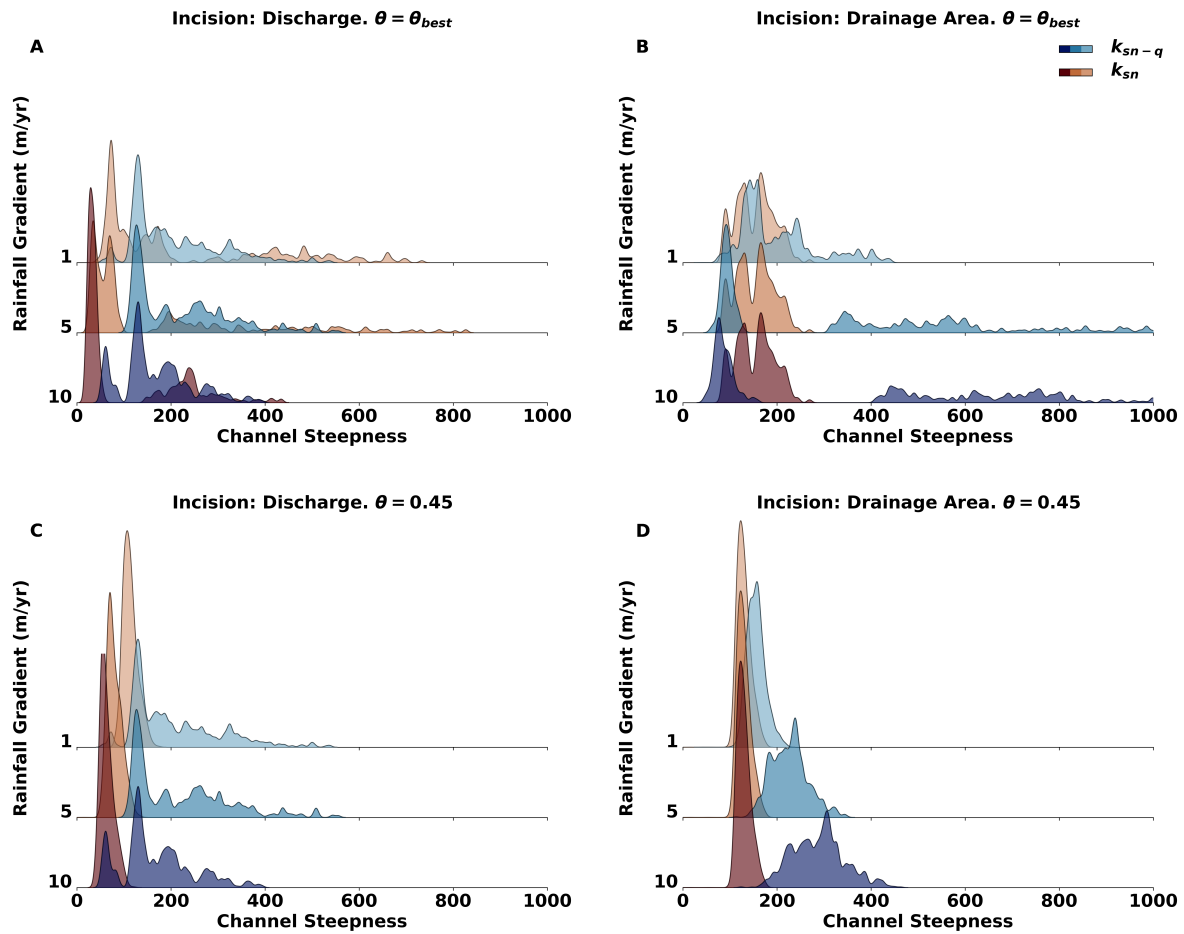


Figure S4. Distribution of k_{sn} and k_{sn-q} values for the basins in the dense blob lithology simulation. (A) and (C) show how the channel steepness distribution remains largely unchanged when using k_{sn-q} but it shifts towards smaller channel when using k_{sn} . (B) and (D) shows a similar trend, but in this case the k_{sn} distributions remain unchanged while the k_{sn-q} as the rainfall is increased.

Table S3. Maximum values of k_{sn} distortion for the dense blob lithology case with $m/n = 0.45$. Bold values indicate the highest distortion for each incision scenario.

Dense Blob Litho.	Case i_A	Case i_Q	Case ii	Case iii
Drainage Area (A)	23%	6%	30%	31%
Discharge (Q)	19%	35%	44%	54%

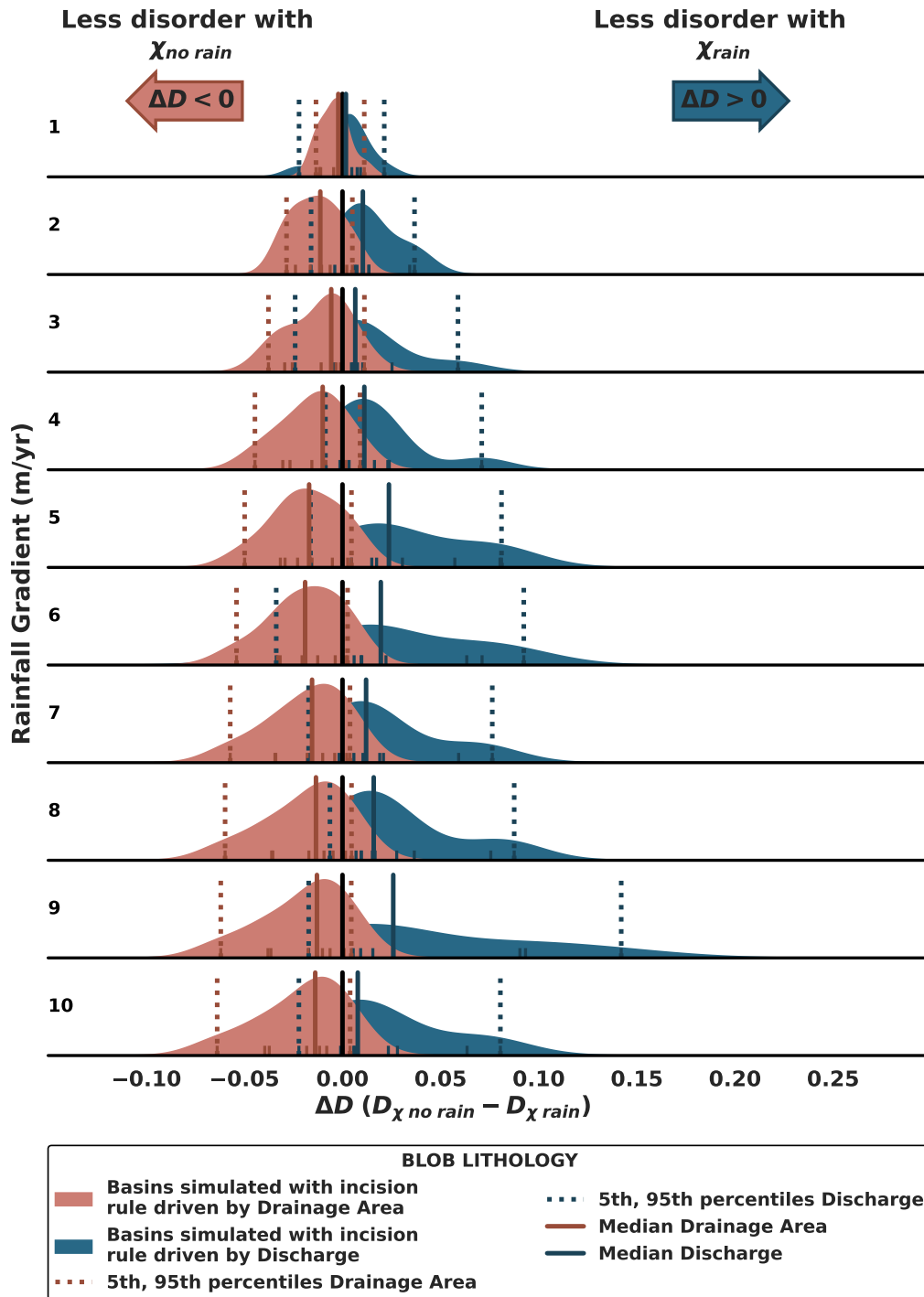


Figure S5. Comparison of the median values for ΔD^* for each of the rainfall ranges for A and Q -driven incision under blob lithology for an initial $m/n=0.45$. Even though the medians lie at either side of the 0 indicator regardless of the rainfall gradient, it is not possible to establish with 95% that the distributions are distinguishable because the percentiles overlap.

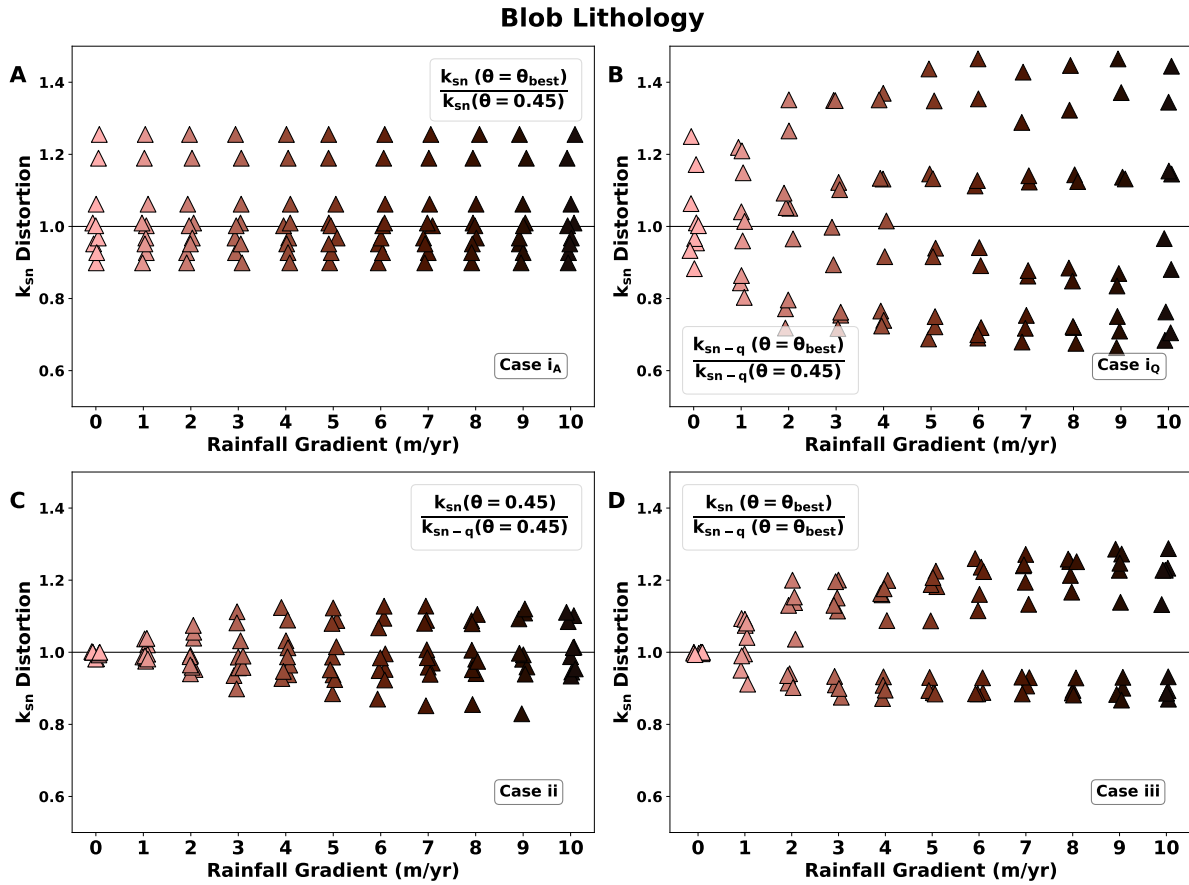


Figure S6. Distortion in k_{sn} for the A -driven incision case under blob lithology and initial $m/n=0.45$. A distortion of 1 (solid black line) keeps the value of k_{sn} unchanged. We show the possible distortion scenarios that one might encounter under different assumptions of concavity index and incision. (A) shows the distortion incurred by not optimising θ under A -driven incision, where we see the largest k_{sn} distortions of up to 46%. (B) highlights the effects of optimising concavity under the incorrect incision scenario (discharge). (C) keeps concavity index at 0.45 but compares incision scenario and (D) comprises the effects of θ optimisation under different assumptions of incision scenarios.

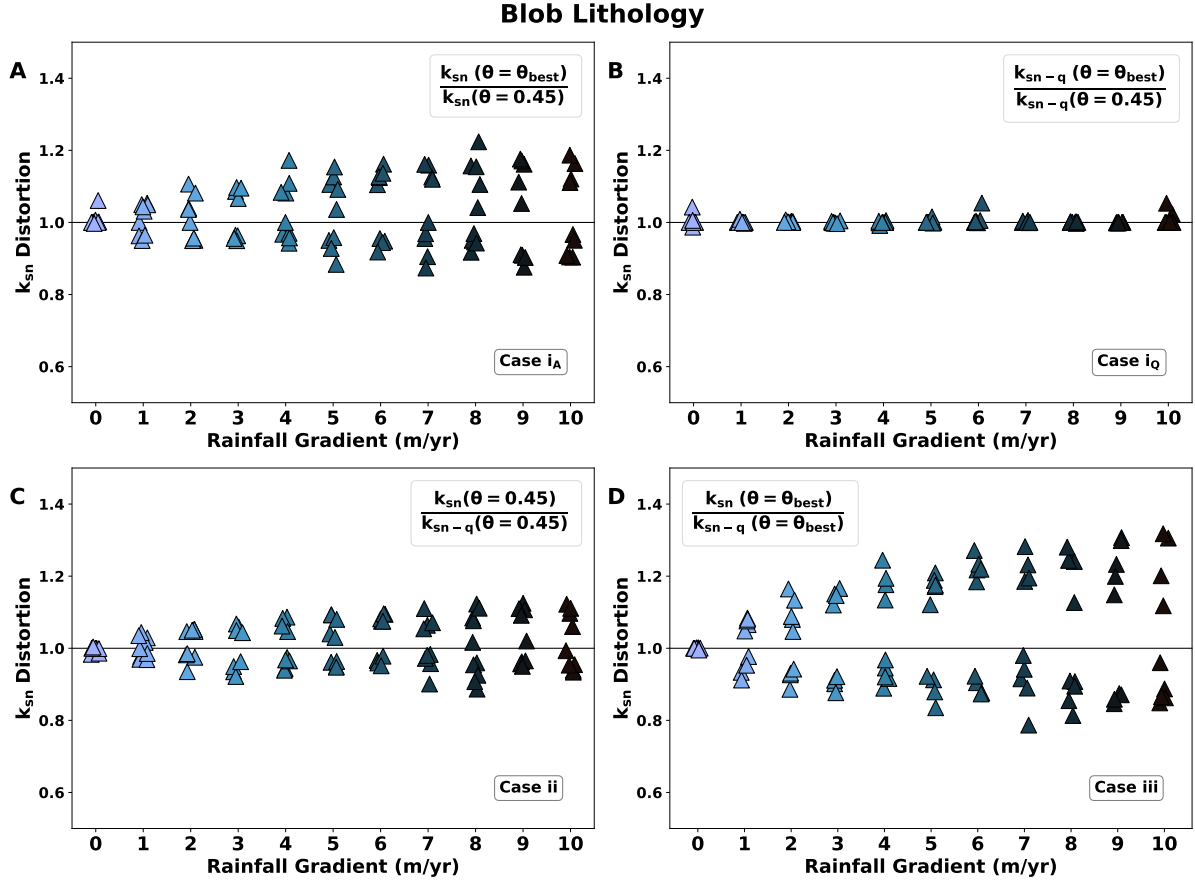


Figure S7. Distortion in k_{sn} for the Q -driven incision case under blob lithology and initial $m/n=0.45$. A distortion of 1 (solid black line) keeps the value of k_{sn} unchanged. We show the possible distortion scenarios that one might encounter under different assumptions of concavity index and incision. (A) highlights the effects of optimising concavity under the incorrect incision scenario (drainage area), whereas (B) shows the distortion incurred by not optimising θ under Q -driven incision. (C) keeps concavity index at 0.45 but compares incision scenario and (D) comprises the effects of θ optimisation under different assumptions of incision scenarios, where we see the largest k_{sn} distortions of up to 32%.

Table S4. Maximum values of k_{sn} distortion for the blob lithology case with $m/n = 0.45$. Bold values indicate the highest distortion for each incision scenario.

Blob Litho.	Case i_Q	Case i_A	Case ii	Case iii
Drainage Area (A)	46%	26%	17%	29%
Discharge (Q)	5%	22%	12%	32%

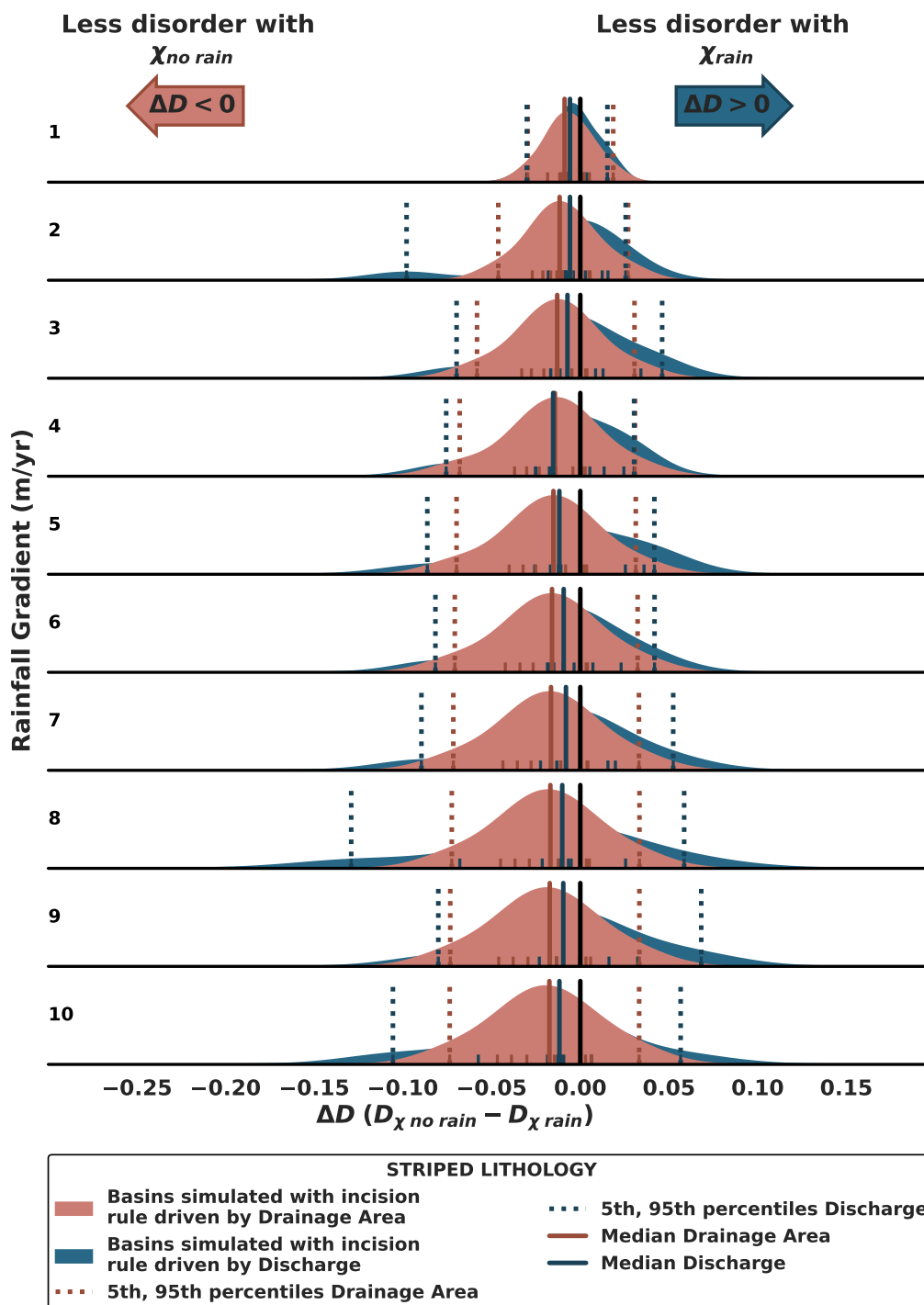


Figure S8. Comparison of the median values for ΔD^* for each of the rainfall ranges for A and Q -driven incision under striped lithology for an initial $m/n=0.45$. In this case, all medians lie on the negative side of the x-axis, with the percentiles fully overlapping, making the distributions non-distinguishable.

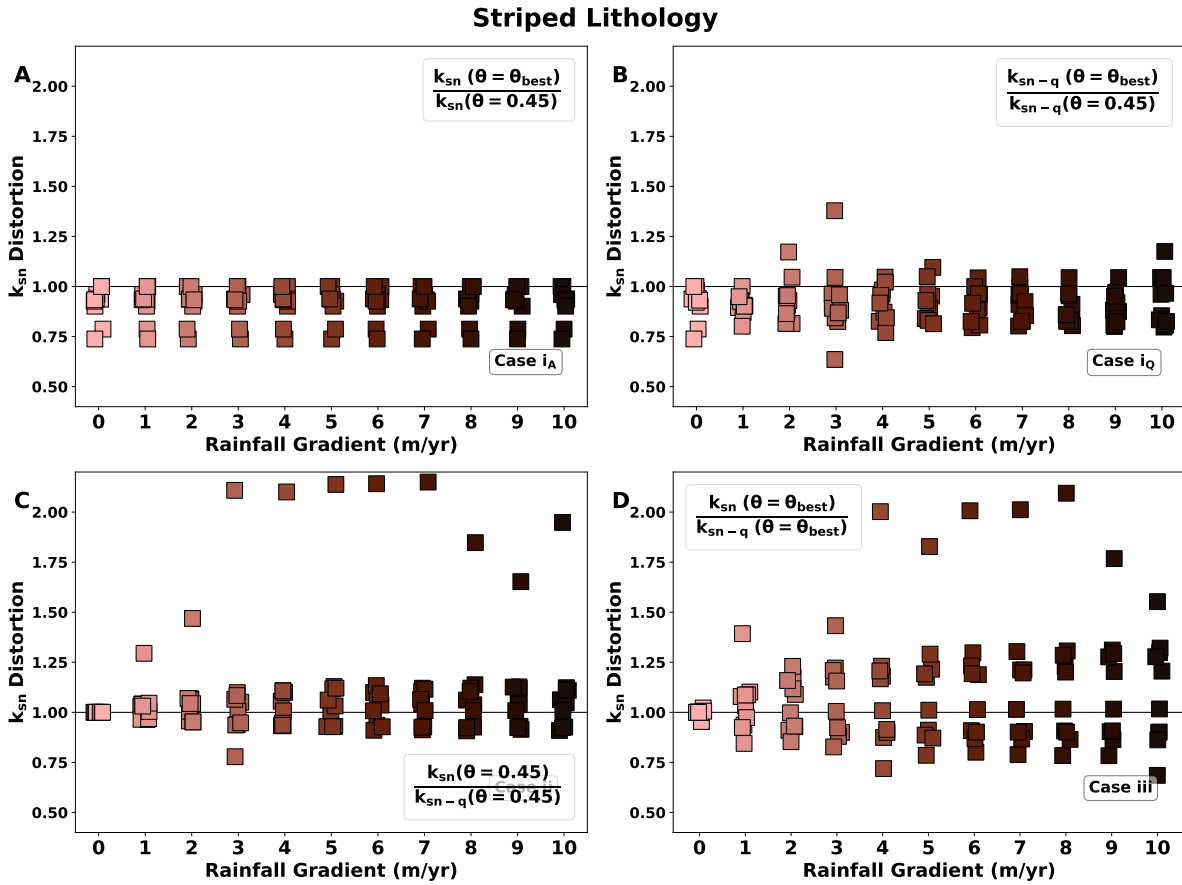


Figure S9. Distortion in k_{sn} for the A -driven incision case under striped lithology and initial $m/n=0.45$. A distortion of 1 (solid black line) keeps the value of k_{sn} unchanged. We show the possible distortion scenarios that one might encounter under different assumptions of concavity index and incision. (A) shows the distortion incurred by not optimising θ under A -driven incision, whereas (B) highlights the effects of optimising concavity under the incorrect incision scenario (discharge), where we see the largest k_{sn} distortions of up to 115%. (C) keeps concavity index at 0.45 but compares incision scenario and (D) comprises the effects of θ optimisation under different assumptions of incision scenarios.

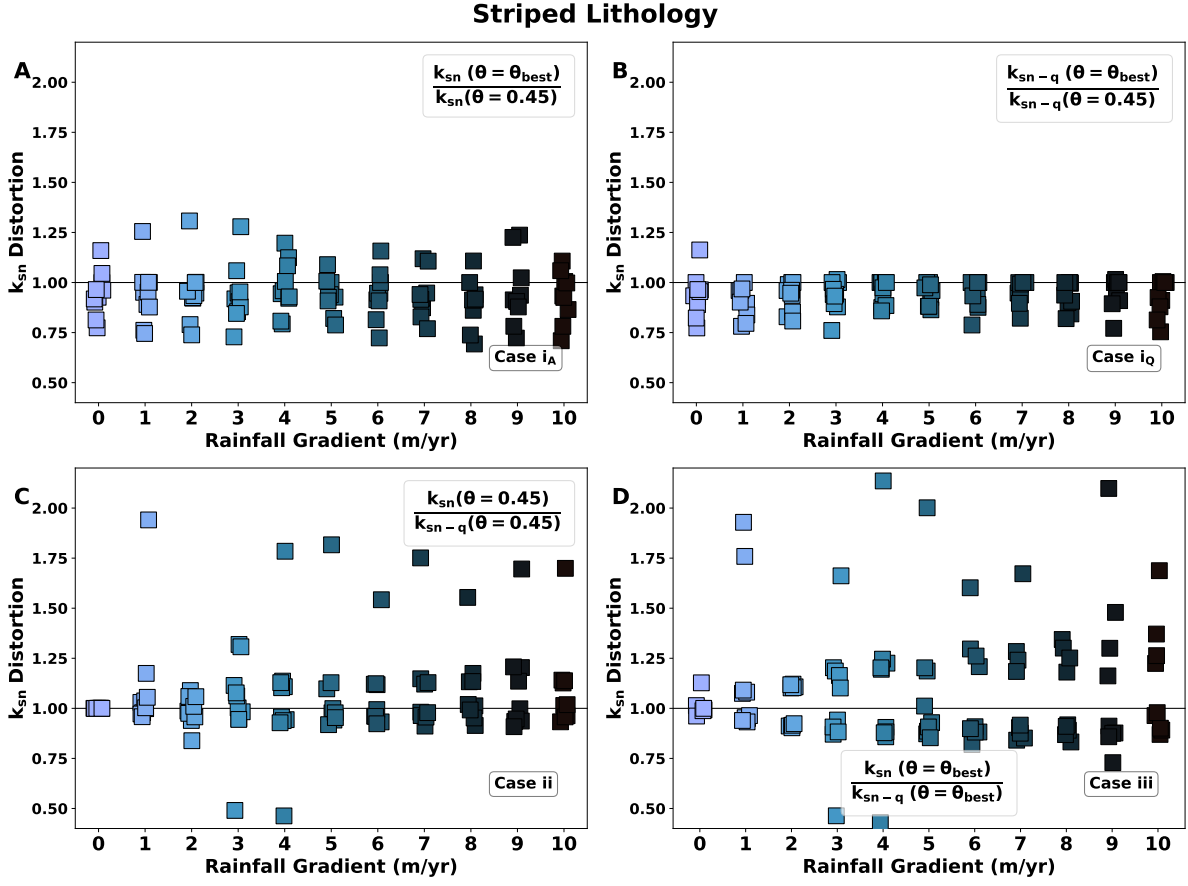


Figure S10. Distortion in k_{sn} for the Q -driven incision case under striped lithology and initial $m/n=0.45$. A distortion of 1 (solid black line) keeps the value of k_{sn} unchanged. We show the possible distortion scenarios that one might encounter under different assumptions of concavity index and incision. (A) highlights the effects of optimising concavity under the incorrect incision scenario (drainage area), whereas (B) shows the distortion incurred by not optimising θ under Q -driven incision. (C) keeps concavity index at 0.45 but compares incision scenario and (D) comprises the effects of θ optimisation under different assumptions of incision scenarios, where we see the largest k_{sn} distortions of up to 114%.

Table S5. Maximum values of k_{sn} distortion for the striped lithology case with $m/n = 0.45$. Bold values indicate the highest distortion for each incision scenario.

Striped Litho.	Case i_Q	Case i_A	Case ii	Case iii
Drainage Area (A)	38%	26%	115%	109%
Discharge (Q)	25%	31%	94%	114%

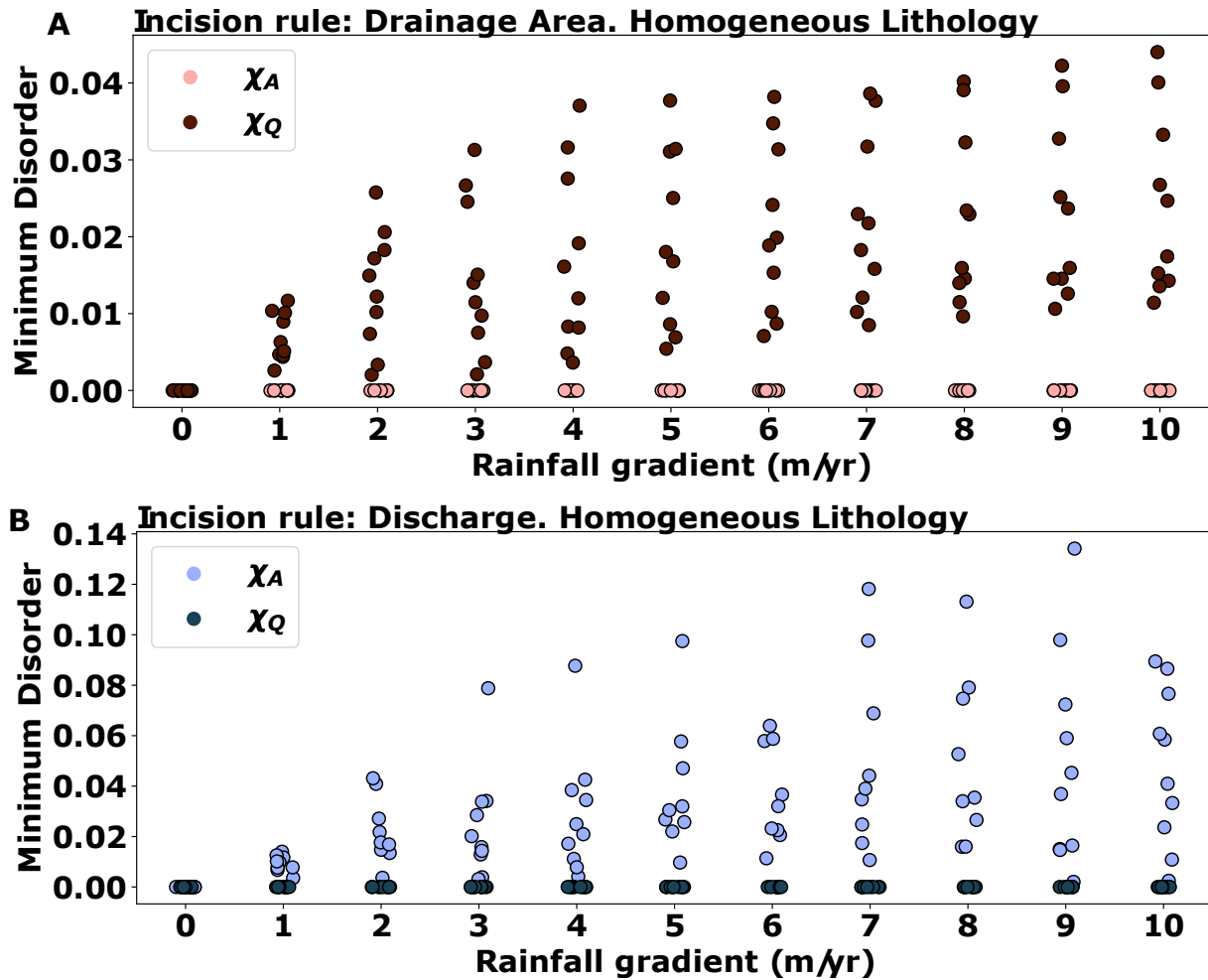


Figure S11. Evolution of the minimum disorder for model runs with a drainage area (A) and a discharge-driven (B) incision rule for a range of rainfall gradients (0-10m/yr) under homogeneous lithology. We show the minimum disorder values when calculating χ_A and χ_Q , for rainfall gradients increases from 0 m/yr to 10 m/yr. The disorder calculated with χ_Q is lower than that calculated with χ_A . The differences become progressively larger as the rainfall gradients increase.

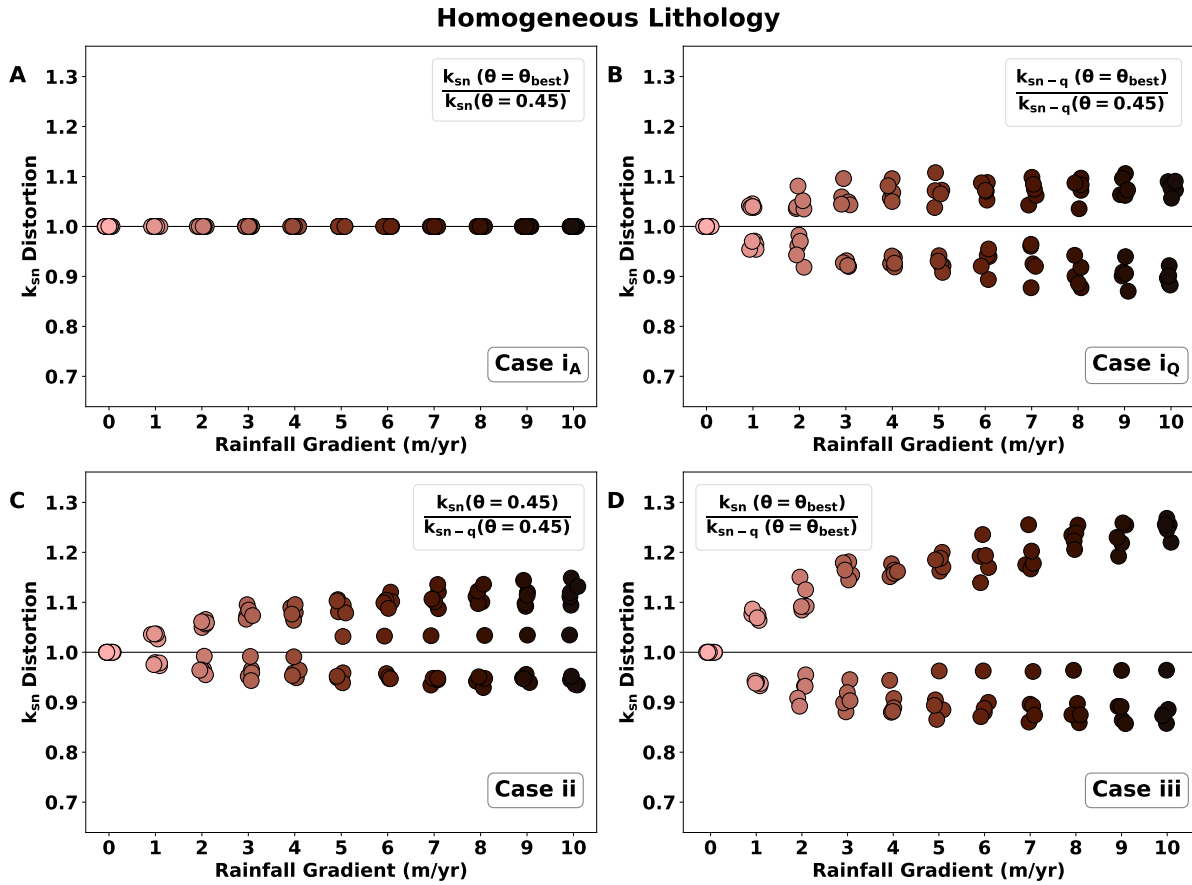


Figure S12. Distortion in k_{sn} for the A-driven incision case under homogeneous lithology and initial $m/n=0.45$. A distortion of 1 (solid black line) keeps the value of k_{sn} unchanged. (A, Case i_A) indicates that no k_{sn} distortion occurs when the concavity index and the incision case match the model scenario. (B), (C) and (D) show the possible distortion scenarios that one might encounter under different assumptions. (B) highlights the effects of optimising concavity index under an incorrect incision scenario, (C) assumes concavity index is kept at 0.45 but the incision scenario changes and (D) comprises the effects of θ optimisation under different assumptions of incision scenarios, where we see the largest k_{sn} distortions of up to 27%.

Homogeneous Lithology

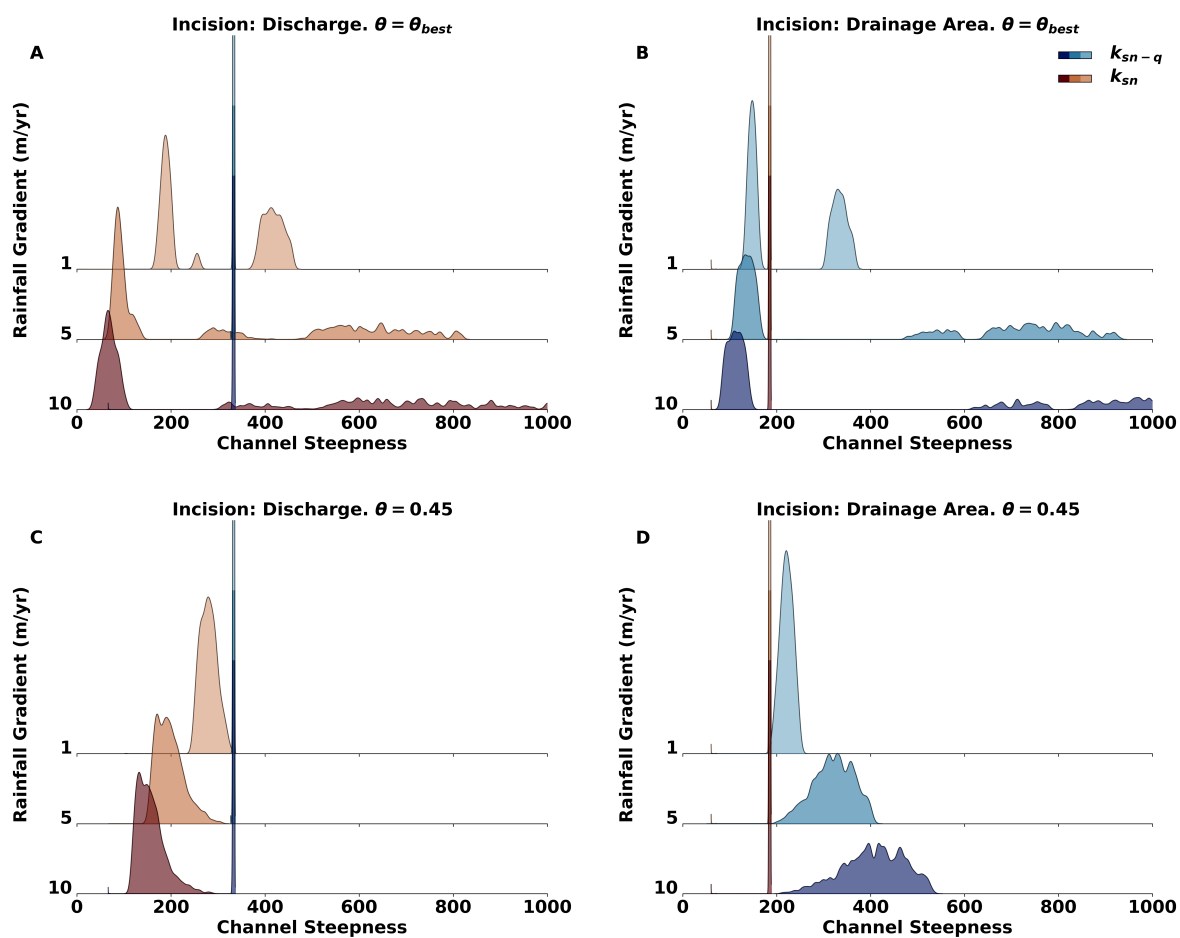


Figure S13. Distribution of k_{sn} and k_{sn-q} values for the basins in the homogeneous lithology simulation. Channel steepness is well constrained when the incision case matches the channel steepness case. The higher the rainfall rate, the larger the distortion in the channel steepness index distributions.

Table S6. Maximum values of k_{sn} distortion for the homogeneous lithology case with $m/n = 0.45$. Bold values indicate the highest distortion for each incision scenario.

Homogeneous Litho.	Case i_Q	Case i_A	Case ii	Case iii
Drainage Area (A)	13%	0%	15%	27%
Discharge (Q)	0%	23%	11%	34%

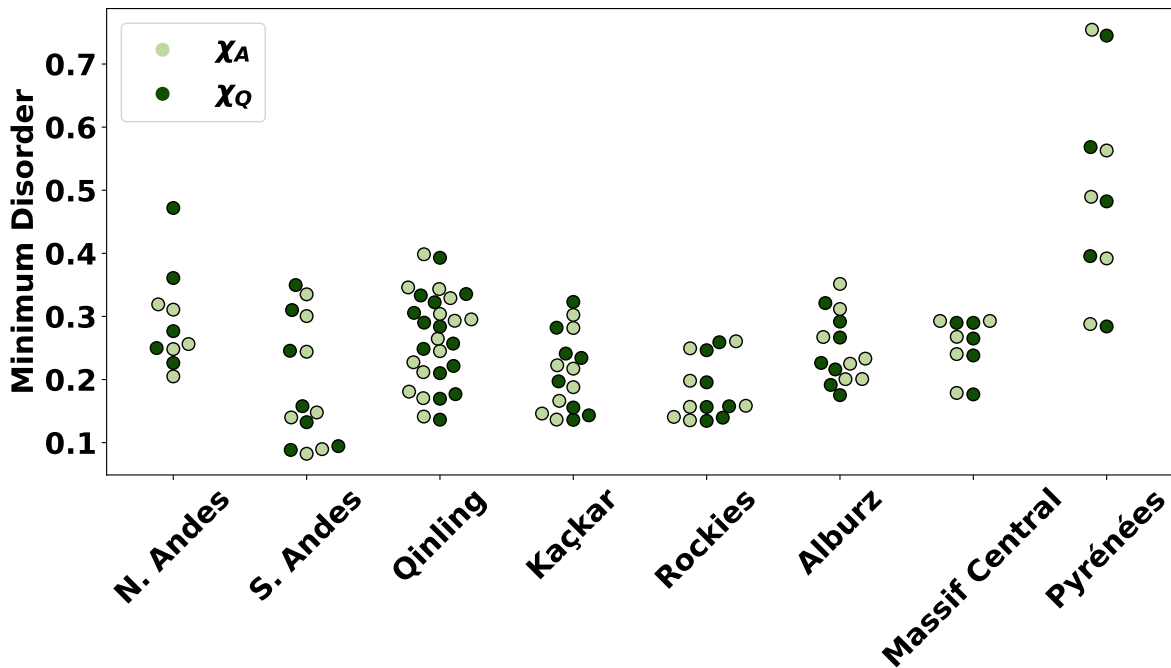


Figure S14. Evolution of the minimum disorder basins in natural landscapes. We show that the minimum D^* values with χ_A and χ_Q have very similar values, making it a challenge to identify the preferential incision route.

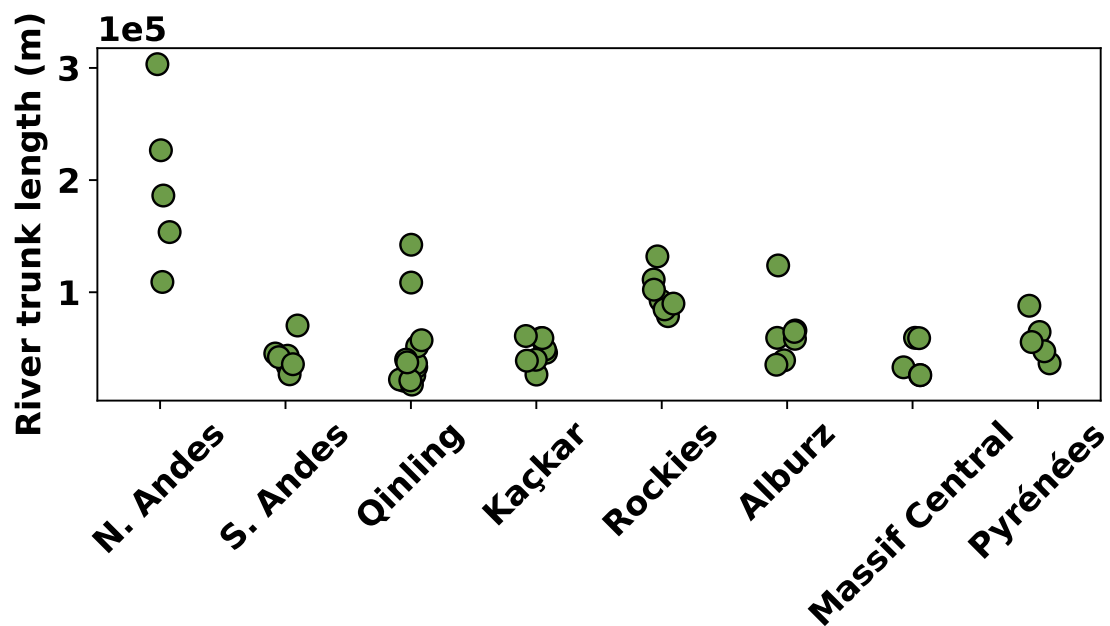


Figure S15. Distribution of the length of the main trunk for the chosen basins in each of the study areas. Areas such as the Northern Andes show a wider range of trunk sizes, from $\sim 100km$ to $> 300km$. Regions such as the Southern Andes or the Kaçkar Mountains all show trunk sizes $< 100km$.

Table S7. Values for the k_{sn} of the basins with maximum distortion in each mountain range under each of the distortion scenarios. Bold values correspond to the case with the highest distortion for each mountain range.

Mountain Range	Case i_A	Case i_Q	Case ii	Case iii
N. Andes	20%	23%	26%	32%
S. Andes	56%	26%	79%	26%
Qinling	81%	50%	28%	33%
Kaçkar	40%	38%	15%	14%
Rockies	47%	44%	6%	5%
Alburz	48%	45%	18%	26%
Massif Central	48%	25%	25%	36%
Pyénées	67%	49%	34%	17%

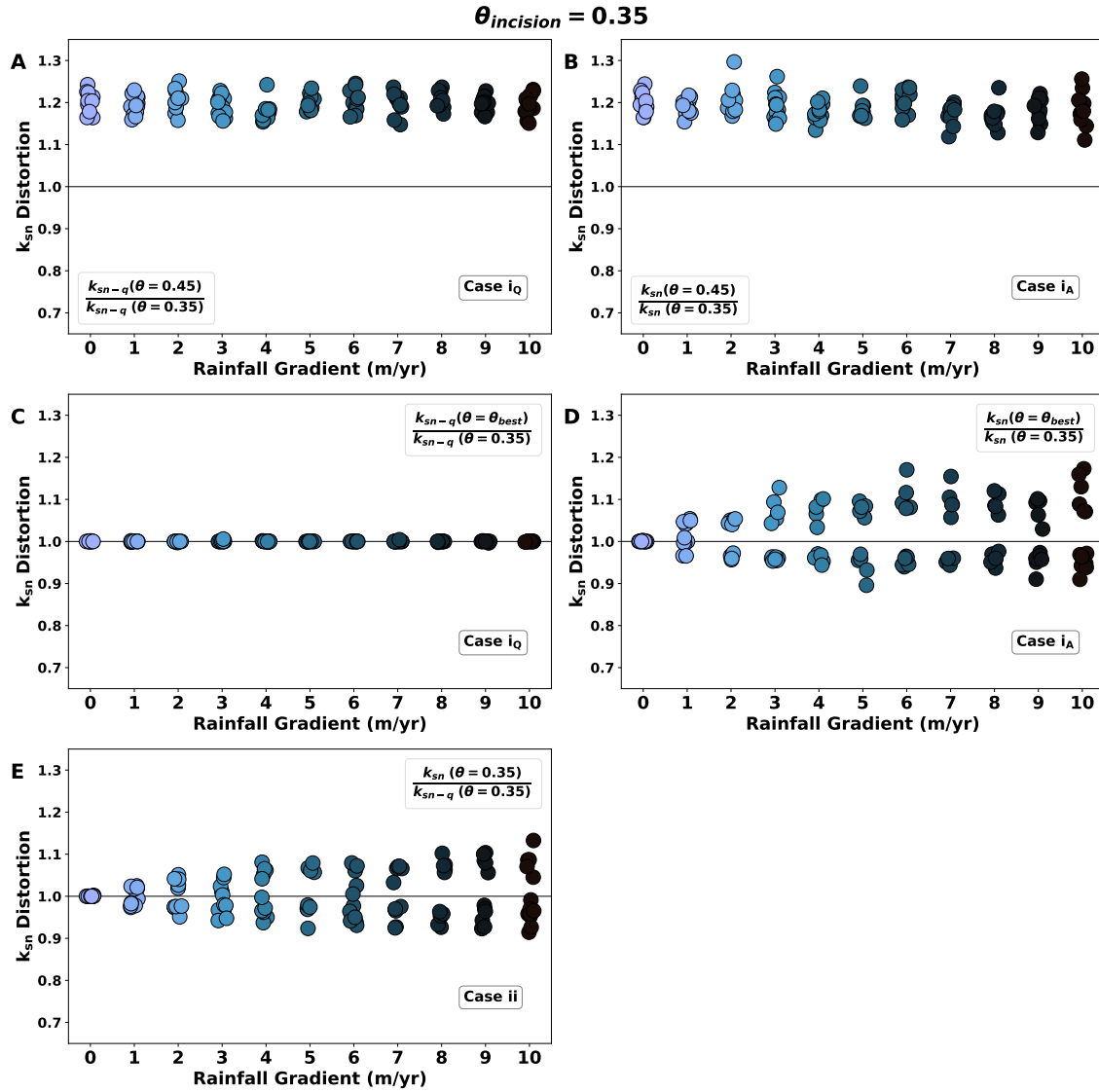


Figure S16. Distortion in k_{sn} for the A-driven incision case under homogeneous lithology and initial $m/n=0.35$. A distortion of 1 (solid black line) keeps the value of k_{sn} unchanged. (C, Case i_Q) indicates that no k_{sn} distortion occurs when the concavity index and the incision case match the model scenario. (D) highlights the effects of optimising concavity index under an incorrect incision scenario, (A) and (B) assumes that concavity index has been chosen as 0.45 for discharge and drainage area-driven scenarios respectively. (E) assesses the distortion caused by different incision assumptions under the correct concavity index (0.35). We see the largest k_{sn} distortions (up to 30%) in (B).

$\theta = 0.35$

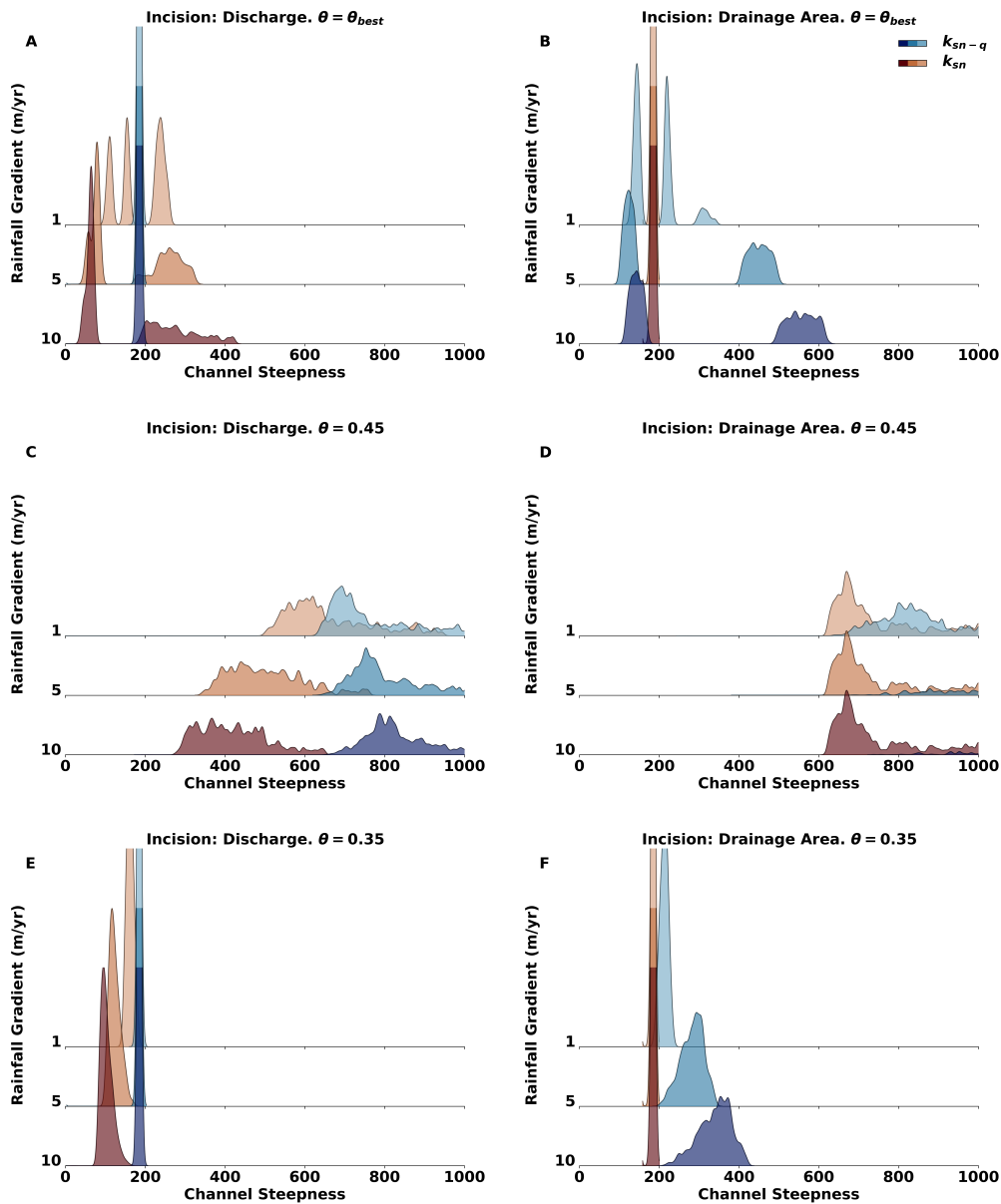


Figure S17. Distribution of k_{sn} and k_{sn-q} values for the basins in the homogeneous lithology simulation with initial concavity of $\theta=0.35$. Channel steepness is well constrained when the incision case matches the channel steepness case. (C) and (D) show the largest deviations from the expected channel steepness distributions. This shows that an incorrect choice of concavity can distort the k_{sn} distributions to a larger extent than rainfall.

Table S8. Maximum values of k_{sn} distortion for the homogeneous lithology case with $m/n = 0.35$. Bold values indicate the highest distortion for each incision scenario.

$m/n = 0.35$	Case $i_{Q,\theta=0.45}$	Case $i_{A,\theta=0.45}$	Case $i_{Q,\theta=\theta_{best}}$	Case $i_{A,\theta=\theta_{best}}$	Case ii
Drainage Area (A)	26%	22%	10%	0%	10%
Discharge (Q)	25%	30%	1%	17%	13%

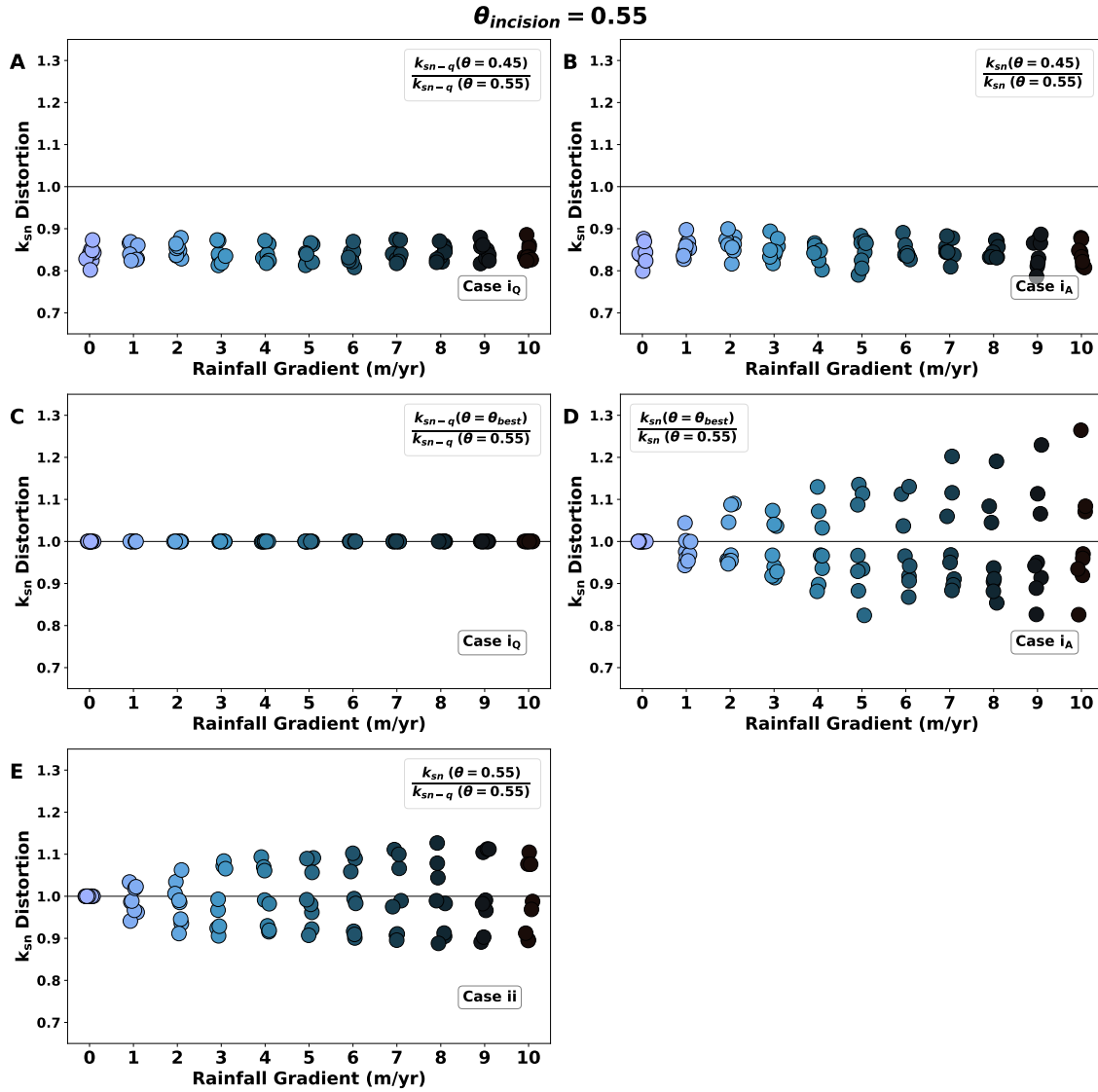


Figure S18. Distortion in k_{sn} for the A-driven incision case under homogeneous lithology and initial $m/n=0.55$. A distortion of 1 (solid black line) keeps the value of k_{sn} unchanged. (C, Case i_Q) indicates that no k_{sn} distortion occurs when the concavity index and the incision case match the model scenario. (D) highlights the effects of optimising concavity index under an incorrect incision scenario, (A) and (B) assumes that concavity index has been chosen as 0.45 for discharge and drainage area-driven scenarios respectively. (E) assesses the distortion caused by different incision assumptions under the correct concavity index (0.55). We see the largest k_{sn} distortions (up to 26%) in (D).

$\theta = 0.55$

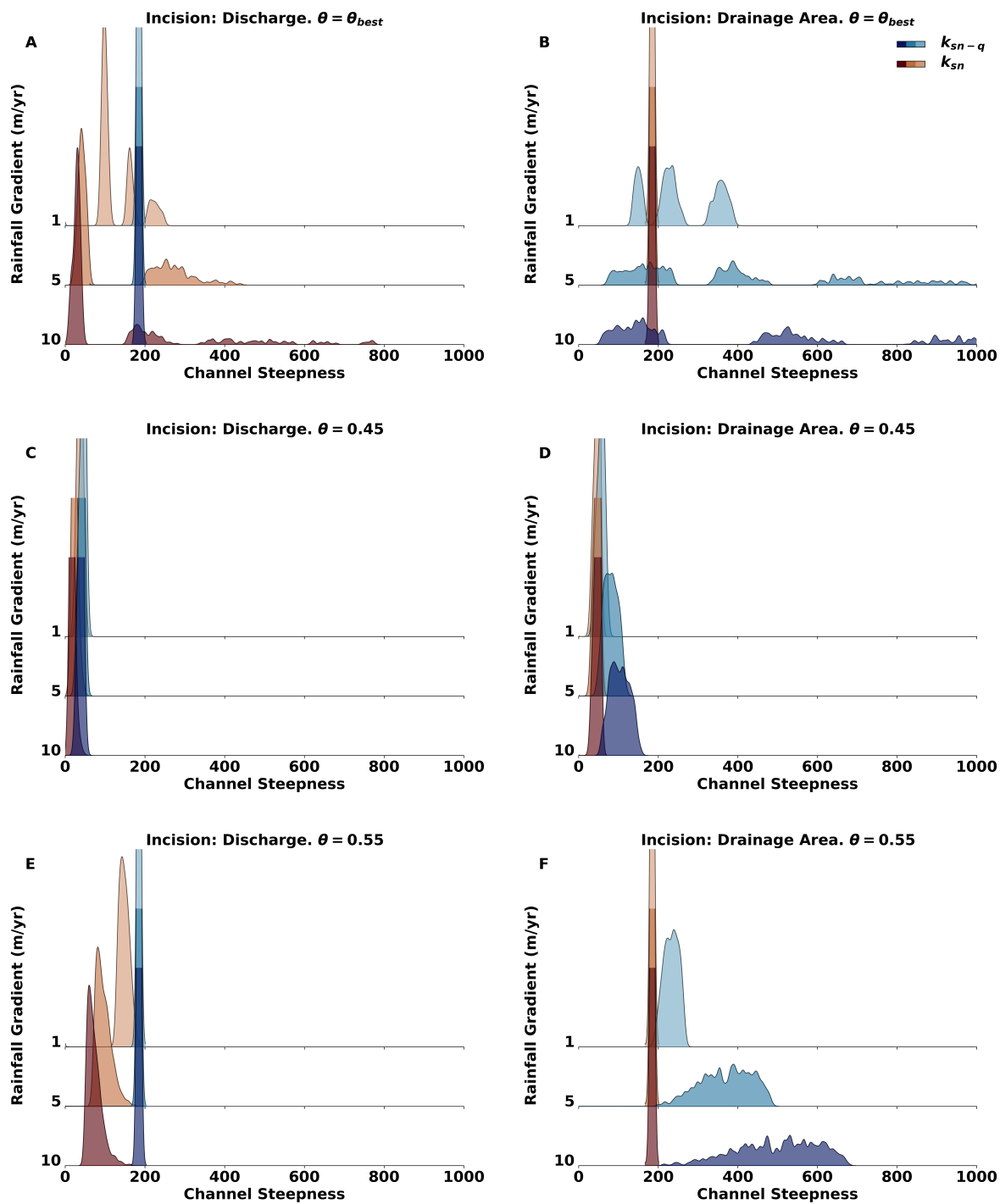


Figure S19. Distribution of k_{sn} and k_{sn-q} values for the basins in the homogeneous lithology simulation with initial concavity of $\theta=0.55$. Channel steepness is well constrained when the incision case matches the channel steepness case.

Table S9. Maximum values of k_{sn} distortion for the homogeneous lithology case with $m/n = 0.55$. Bold values indicate the highest distortion for each incision scenario.

$m/n = 0.55$	Case $i_{Q,\theta=0.45}$	Case $i_{A,\theta=0.45}$	Case $i_{Q,\theta=\theta_{best}}$	Case $i_{A,\theta=\theta_{best}}$	Case ii
Drainage Area (A)	21%	17%	18%	0%	10%
Discharge (Q)	20%	21%	0%	26%	13%